Remote Access Computed Tomography Colonography

AUTHORED BY QIUSHA MIN, B.SC.

SUPERVISED BY DR ROBERT SADLEIR

SCHOOL OF ELECTRONIC ENGINEERING

DUBLIN CITY UNIVERSITY

THESIS SUBMITTED FOR THE DEGREE OF DOCTOR OF PHILOSOPHY

August 2013

Declaration

I hereby certify that this material, which I now submit for assessment on the programme of study leading to the award of Doctor of Philosophy is entirely my own work, that I have exercised reasonable care to ensure that the work is original, and does not to the best of my knowledge breach any law of copyright, and has not been taken from the work of others save and to the extent that such work has been cited and acknowledged within the text of my work.

Signed : _____________ **ID NO. :** _____________

Date : _____________

Acknowledgements

I would like to take this opportunity to offer my sincere thanks to Dr Robert Sadleir for his patient supervision and valuable help during the course of my PhD research. In addition, I would like to express my sincere gratitude to all the members of the Vision System Group, for their encouragement, help and friendship during the time I spent in DCU. Special thanks go to Dr Tarik Chowdhury, Patricia Moore, Jiao Tian, Sha Yu, Dr Ayodeji Adesina and Michele Peporte. I am also most grateful to my parents for their constant encouragement and tremendous support.

Finally, I would like to thank the Chinese Scholarship Council, Dublin City University and the Irish Universities Association, for generously funding my PhD research.

Contents

List of Figures **xiii**

List of Tables **xv**

Abstract **xv**

Publications Arising from this Research **xvii**

Glossary of Acronyms **xviii**

1 Introduction **1**
- 1.1 Motivation 4
- 1.2 Technical Challenges 10
- 1.3 Contributions 15
- 1.4 Thesis Organisation 16

2 Literature Review **18**
- 2.1 Volume Rendering 18
  - 2.1.1 Basic Algorithms 20
    - 2.1.1.1 Ray Casting 20

2.1.1.2 Splatting 21
2.1.1.3 Shear-warp 22
2.1.1.4 3D Texture-mapping 23
2.1.2 Acceleration Techniques 24
2.1.3 Methods Designed for CTC 30
2.1.4 Discussion 33
2.2 Medical Data Compression 33
2.2.1 Predictive Coding 35
2.2.2 Transform Coding 43
2.2.3 Pyramid Coding 47
2.2.4 Multiplicative Autoregressive Models 49
2.2.5 Hybrid Techniques 49
2.2.6 Anatomy-based Compression 53
2.2.7 Discussion 53
2.3 Conclusion 57

3 Software-based Real-time Volume Rendering 59
3.1 Overview of the Proposed Volume Rendering Technique 60
3.2 Acceleration Methods 62
3.2.1 Rendering with Subvolume 62
3.2.2 Constant Ray Step 63
3.2.3 Optimised Trilinear Interpolation 64
3.3 Experiments and Results 68
3.3.1 Rendering Time 69
3.3.2 Rendering Quality 71
3.3.3 Diagnostic Capability 73
3.4 Conclusion 76

4 An Anatomy-based Segmentation Method for Image Compression 78
4.1 Overview of the Proposed Compression Scheme 79
4.2 Anatomical Terms 84
  4.2.1 Anatomical Terms for Tissues 84
  4.2.2 Anatomical Terms for Describing Positions 84
4.3 Categorisation of Different Anatomical Regions 85
4.4 Analysis of the Features for Each Category 87
  4.4.1 Density Features 87
  4.4.2 Anatomical Features 89
4.5 Automatic Segmentation in the Context of Compression 98
  4.5.1 The Proposed Segmentation Method 98
  4.5.2 Experiments and Results 102
  4.5.3 Discussion 104
4.6 Conclusion 106

5 Adaptive Prediction Model 108
5.1 Interior-based Prediction Model 109
  5.1.1 Template Identification 109
  5.1.2 Model Determination 117
5.2 Edge-based Prediction Model 118
  5.2.1 Estimation of the Normal Direction 120
  5.2.2 Quantisation of the Angle 122
  5.2.3 Model Determination 123
5.3 Experiments and results 126
  5.3.1 Qualitative Evaluation 126
  5.3.2 Quantitative Evaluation 127
5.4 Conclusion 129

6 Delivery Scheme Implementation and Evaluation 131
6.1 Lossless Compression Performance 132
  6.1.1 Data Description 133
  6.1.2 Lossless Entropy Coding 133
  6.1.3 Complete Lossless Performance 135
6.2 Delivery Scheme 137
  6.2.1 Experimental Environment 138
  6.2.2 Description of the Experiment 139
  6.2.3 Experiments and Results 139
6.3 Discussion 141
  6.3.1 Template Optimisation 141
  6.3.2 Scalable Compression 143
  6.3.3 Transmission Optimisation 147
6.4 Conclusion 147

7 System integration 149
7.1 The Proposed Framework for Remote Access CTC Training . . . 149
  7.1.1 Data Connection 150
  7.1.2 Functionality Provided by the Framework 150
  7.1.3 Feedback 153
7.2 Implementation 153
7.3 Conclusion 154

8 Conclusions and Future Work 156
8.1 Research Contributions 157
  8.1.1 Major Contributions 158
  8.1.2 Minor Contributions 160
8.2 Future Work 161

Appendix A: Description of the Data Used for Development and Testing 164

Appendix B: Overview of the Implemented System 166

References 189

List of Figures

1.1 Examples of CTC images. (a) A 2D slice from a CTC data set. (b) A 3D rendering of a CTC data set. 3
1.2 Outline of the main steps for remote access CTC training. 12
1.3 An overview of a comprehensive graphical user interface for a remote access CTC training system. 13

2.1 An illustration of ray casting. A ray starting from a viewpoint is cast through the volume. 20
2.2 The ray compositing process in volume rendering. 21
2.3 An illustration of splatting. Each voxel is projected onto the image plane using a footprint. 22
2.4 A demonstration of the three stages of the shear-warp method. . . 23
2.5 A sample CT image and its histogram. 26
2.6 An illustration of skipping empty areas within the colon. 27
2.7 A ray traversing a slice from a volumetric data set based on the proximity clouds technique. 28
2.8 Examples of parallel (left) and perspective (right) projections. . . 31
2.9 A development timeline of medical image compression techniques. 36

2.10 A block representation of a general predictive coding method. . . 36
2.11 The pixel neighbourhood used to predict the value of X in JPEG compression. 38
2.12 A block representation of a general transform coding method. . . 43
2.13 An illustration of the set definition in SPIHT. 46
2.14 A four-level pyramid decomposition. 48
2.15 The wavelet transform representation of an image. 52

3.1 A flowchart of the proposed volume rendering technique. 61
3.2 Navigation within the colon using the subvolume technique. . . . 63
3.3 Determining ray step length in the x direction. 64
3.4 The trilinear interpolation process. The red dots show the known voxels and the green dot is the point to be interpolated. 66
3.5 Volume rendering performance provided by different techniques in conjunction with a range of different subvolume sizes. 70
3.6 Volume rendering using the proposed method and the VTK to display a polyp. 71
3.7 Volume rendering using the proposed method and the VTK to display folds in the colon. 72
3.8 Volume rendering using the proposed method and the VTK to display colonic wall. 72
3.9 Volume rendering using the proposed method and the VTK to display the inflation tube that is used in a CTC examination. . . 72
3.10 Visualisations of polyps with size $\geq 5mm$ using the proposed volume rendering technique. 74
3.11 Visualisations of small polyps ($< 5mm$) using the proposed volume rendering technique. 75

4.1 Influence of image sampling on the PVE. The actual object is displayed in the left image and the right image is processed by sampling. In the right image, pixels on the edges of the object are associated with both the object and the surrounding tissues. The densities of these pixels are the mean of the underlying regions. . 80

4.2 A block diagram of the proposed compression scheme (ALMIC). . 82

4.3 An illustration of the main regions typically found in a CT data set. 83

4.4 A global histogram of a sample CTC data set. 88

4.5 A model of the anatomical structure in an abdominal CT data set. 90

4.6 An illustration of the identification process for the subcutaneous tissue region. The candidate subcutaneous tissue region is indicated by grey colour. 91

4.7 The top slices of six abdominal CT data sets. 93

4.8 An illustration of the liver region identification process. The candidate liver region (R_l) is indicated within the red dashed semi-ellipse. 94

4.9 An illustration of the kidney region identification process. The candidate kidney regions (R_k) are indicated within the red dashed ellipse. 97

4.10 An illustration of the spleen region identification process. The candidate spleen region (R_s) is indicated within the red dashed box. 98

4.11 Flowchart of the segmentation process using the proposed technique. 100

4.12 The template used for region identification. 101

4.13 The segmentation results using the proposed technique. (a, c) original images. (b, d) segmented images. 102

5.1 The diamond template used for prediction. The size of this template is 9 pixels. 110

5.2 The sphere template used for prediction. The radius of this template is 3 pixels. 110

5.3 The cube template used for prediction. The size of this template is 5 pixels. 111

5.4 The average residual entropies of the bone region tested on 20 CTC data sets. 113

5.5 The average residual entropies of the soft tissue region tested on 20 CTC data sets. 113

5.6 The average residual entropies of the air region tested on 20 CTC data sets. 114

5.7 The average residual entropies of the adipose tissue region tested on 20 CTC data sets. 114

5.8 Edge transitions in an example CT image and a natural image. The upper left image is a 16-bit CT image and the upper right image is the profile plot corresponding to the lines in the CT image. The lower left image is a 16-bit grey-scale Lena image and the lower right image is the profile plot corresponding to the lines in the Lena image. 119

5.9 An unoptimised approach for organising the input variables used by a PVE prediction scheme. The order of input variables is indicated by the numbers in the templates. 121

5.10 An optimised approach for organising the input variables used by a PVE prediction scheme where the template has been rotated according to the edge normal. 121

5.11 The new 3D normal calculator for use in the context of compression where $p_a = 1$, $p_b = 0$ and $p_c = \frac{1}{2}$. (the centre point (in red) is the current pixel) 123

5.12 A 3D representation of the full set of prediction templates used by the proposed edge-based prediction method. The initial templates of T1, T2, T3 and T4 are at locations A, B, C and D respectively. The other templates are generated from these initial templates using rotation and translation. 124
5.13 Residue images of a CT image after different prediction methods. a) original image, b) MED, c) 2D GAP, d) 3D GAP, e) 3D JPEG-4, and f) the proposed prediction method (AAP). 128

6.1 The encoding and decoding processes of the ALMIC technique. . . 132
6.2 Overview of the experimental testbed for modelling the network environment. 138
6.3 Performance of the delivery time for data set 1 over a range of different connection speeds. 140
6.4 The image compression ratio before and after removing the area outside the body. 145

7.1 An outline of the proposed online framework for CTC training. . . 151

1 The four methods provided for navigating through the slices in a data set: slider-based navigation, previous and next buttons, arrow keys and scroll wheel. 166
2 Control over the magnification of a slice using the zoom in, zoom out and reset buttons. 167
3 The three types of images provided by the system: axial, sagittal and coronal images. In this figure, an axial image is displayed on the left and a sagittal image is displayed on the right side. 167
4 A windowed image where the following settings have been used: window centre, 300 HU; window width, 200 HU. 168

5 Perspective volume rendering of a region of interest. This 3D model can be rotated as follows: the plus key moves the viewpoint forward, the minus key moves the viewpoint backward and the arrow keys rotate the 3D model. 168

6 A surface rendering of the entire colon which can be controlled by the user via the mouse. 169

7 A single frame of fly-through within the surface rendered model of the colon. 169

8 The tool for flagging a potential polyp. This tool allows a polyp size, a polyp type and a confidence value to be specified. 170

9 Automatic evaluation of the submitted findings based on the gold standard and presentation of the correct diagnosis. 170

List of Tables

1.1 The specific number of CTC training cases recommended by various international radiologist organisations. 5
1.2 Selected expert suggestions for CTC training 7

2.1 An overview of previously published volume rendering techniques 34
2.2 The seven JPEG predictors used to estimate the value of the current pixel based on its neighbours P_W, P_N and P_{NW}. 38
2.3 Previous compression results tested on 8-bit medical images. . . . 54
2.4 Previous compression results tested on 12-bit medical images. . . 55

3.1 Volume rendering performance using different subvolume sizes. . . 69

4.1 The properties of the main regions typically found in a CTC data set. 86
4.2 Statistical evaluation of colon and kidney segmentation quality. . 104
4.3 Common sources of abnormalities within the abdomen. 106

5.1 The number of causal pixels associated with different sizes of diamond-based, sphere-based and cube-based templates. 112

5.2 The results of the cross-validation study comparing the performance of the different templates. D represents diamond, S represents sphere and C represents cube. The sizes of diamond, sphere and cube are 9, 3 and 5 pixels respectively. 115
5.3 The specifications for the four template categories 125
5.4 Entropies of prediction residuals for MED, GAP, 3D JPEG-4 and AAP models. 129

6.1 Compression ratio for each lossless compression method. 134
6.2 Lossless compression results using various compression methods. . 136
6.3 The details of equipment used in the experiments. 138
6.4 The delivery performance achieved using different template sizes. . 144

1 An explanation of the abbreviations used in Table 2. 164
2 Details of the CTC data sets used in this thesis. 165

Title: Remote Access Computed Tomography Colonography

Author: Qiusha Min

Abstract

This thesis presents a novel framework for remote access Computed Tomography Colonography (CTC). The proposed framework consists of several integrated components: medical image data delivery, 2D image processing, 3D visualisation, and feedback provision. Medical image data sets are notoriously large and preserving the integrity of the patient data is essential. This makes real-time delivery and visualisation a key challenge. The main contribution of this work is the development of an efficient, lossless compression scheme to minimise the size of the data to be transmitted, thereby alleviating transmission time delays. The scheme utilises prior knowledge of anatomical information to divide the data into specific regions. An optimised compression method for each anatomical region is then applied. An evaluation of this compression technique shows that the proposed 'divide and conquer' approach significantly improves upon the level of compression achieved using more traditional global compression schemes.

Another contribution of this work resides in the development of an improved volume rendering technique that provides real-time 3D visualisations of regions within CTC data sets. Unlike previous hardware acceleration methods which rely on dedicated devices, this approach employs a series of software acceleration techniques based on the characteristic properties of CTC data. A quantitative and qualitative evaluation indicates that the proposed method achieves real-time performance on a low-cost PC platform without sacrificing any image quality.

Fast data delivery and real-time volume rendering represent the key features that are required for remote access CTC. These features are ultimately combined with other relevant CTC functionality to create a comprehensive, high-performance CTC framework, which makes remote access CTC feasible, even in the case of standard Web clients with low-speed data connections.

Publications Arising from this Research

- Qiusha Min & Robert J.T. Sadleir, A Hybrid Lossless Compression Scheme for Efficient Delivery of Medical Image Data over the Internet, 2010 Second International Conference on Computer Modeling and Simulation, Vol.1, pp.319-323, 2010.

- Qiusha Min & Robert J.T. Sadleir, A Real-time Software-based Volume Rendering Technique for Virtual Endoscopy, China-Ireland International Conference on Information and Communications Technologies, 2010.

- Qiusha Min & Robert J.T. Sadleir, A Segmentation Based Lossless Compression Scheme for Volumetric Medical Image Data, 2011 Irish Machine Vision and Image Processing Conference, pp.101-102, 2011.

- Qiusha Min & Robert J.T. Sadleir, Medical Image Compression Using Region-based Prediction, 2012 IEEE-EMBS Conference on Biomedical Engineering (IECBES 2012), 2012.

- Qiusha Min & Robert J.T. Sadleir, An Edge-based Prediction Approach for Medical Image Compression, 2012 IEEE-EMBS Conference on Biomedical Engineering (IECBES 2012), 2012.

Glossary of Acronyms

Acronyms		**Explanation**
2D	—	Two-Dimensions
3D	—	Three-Dimensions
CT	—	Computed Tomography
CTC	—	CT Colonography
CRC	—	Colorectal Cancer
HU	—	Hounsfield Unit
MR	—	Magnetic Resonance
PET	—	Positron Emission Tomography
PVE	—	Partial Volume Effect
GPU	—	Graphics Processing Unit
JPEG	—	Joint Photographic Experts Group
LS	—	Least Square

MMSE — Minimum Mean Square Error

GAP — Gradient Adjusted Prediction

GED — Gradient Edge Detection

MED — Median Edge Detection

EDP — Edge-Directed Prediction

AAP — Anatomy-based Adaptive Prediction

ALMIC — Anatomy-based Lossless Medical Image Compression

Mbps — Megabits per second

Chapter 1

Introduction

Cancer is a major cause of death worldwide and the number of cases is increasing at a significant rate. According to a report from the World Health Organisation (WHO, 2003), by 2020, the worldwide incidence of cancer could climb by 50% to 15 million. As the fourth most common cause of cancer death, colorectal cancer (CRC) was responsible for approximately 608,000 deaths worldwide in 2008 (WHO, 2012). Furthermore, CRC is the second most common type of cancer and the second leading cause of cancer deaths in developed countries (Martinez, 2005).

CRC screening is regarded as an efficient approach in the diagnosis of CRC at an early stage, which can significantly reduce the risk of death. However, it should be noted that colonoscopy, which is the main conventional colorectal cancer screening technique, is an extremely uncomfortable and highly invasive procedure. The colonoscopy examination involves inserting an instrument known as an endoscopic probe into the colon through the rectum. The physician examines the inner surface of the colon with the use of a camera attached to the tip of the probe. In some cases, sedation is required in this procedure; therefore, after the examination, the patient requires a significant amount of time to recover from the effects of sedation. The main drawback associated with the colonoscopy examination is that it may cause a number of possible complications, e.g. perforation, infection and haemorrhage. A previous study that explored the risks of perforation resulting from colonoscopy reported that 20 perforations occurred in 10,000 colonoscopy examinations and two patients died as a result of perforation (Anderson *et al.*, 2000). Consequently, the potential efficiency and practicality of colonoscopy are compromised by limitations related to the comfort and safety of the patient.

Computed Tomography Colonography (CTC) is an alternative to conventional colonoscopy for the diagnosis of CRC. It uses a CT scanner to create a virtual representation of the abdomen for a suitably prepared patient. The patient must undergo a bowel-cleansing regimen before scanning. This is similar to the preparation for a conventional colonoscopy examination. In addition, air or CO_2 is pumped into the patient's colon in order to inflate the colon for better viewing. Immediately after air insufflation, some patients temporarily feel slight abdominal cramping, but significant pain is infrequent. A CT scanner is then used to produce a series of cross-sectional images of the abdomen. This data is referred to as a CTC data set. A CTC study typically includes two data sets recorded in the supine and the prone positions. There are approximately 250 slices in a CTC data set and each slice contains 512 × 512 pixels. The density characteristics of the materials in CT images are represented using Hounsfield Units (HU). The HU scale is a linear scale that defines the density of water as 0 HU and the density of air as -1000 HU. The acquired CTC data set can be reconstructed in the form of 2D slices and these slices can subsequently be rendered using 3D techniques (see Figure 1.1). These images are ultimately interpreted by a skilled radiologist to evaluate the colon's inner surface.

The significant advantages of CTC can be summarised as follows: it is a min-

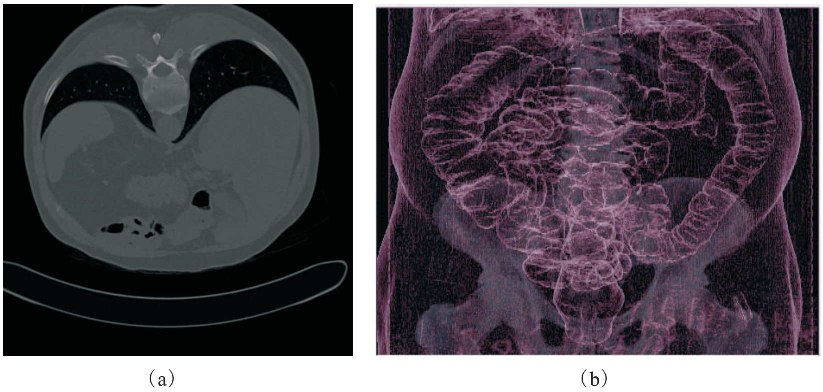
(a) (b)

Figure 1.1: Examples of CTC images. (a) A 2D slice from a CTC data set. (b) A 3D rendering of a CTC data set.

imally invasive examination, *inter alia*, no sedatives or analgesics are required, and it is less time-consuming than conventional colonoscopy. Thus, CTC can be considered more acceptable to patients. Svensson *et al.* (2002) surveyed patients who underwent both CTC and conventional colonoscopy to determine their preferences for both examinations. According to the results of this survey, 82% of patients who experienced both examinations preferred CTC and 57% regarded CTC as "not painful " compared with 26% for conventional colonoscopy.

In addition, a number of studies have been carried out in an attempt to estimate the sensitivity and accuracy of CTC, especially in comparison with conventional colonoscopy. The study by Fenlon *et al.* (1999) showed that CTC and conventional colonoscopy have a similar level of efficiency for polyps $\geqslant$ 6 mm in diameter. In general, polyps can be classified as small ($<$6 mm), medium (6 to 10 mm) or large ($>$10 mm) (Summers, 2010). Larger polyps have a greater likelihood of being or becoming cancer. Fenlon *et al.* (1999) indicated that CTC is sufficient for the detection of medium and large polyps. The same conclusion was drawn by Kim *et al.* (2007a), Arnesen *et al.* (2007) and Graser *et al.* (2009). Therefore, compared to colonoscopy examinations, CTC has nearly the same performance in terms of sensitivity and accuracy for the detection of high-risk polyps, while providing a lower risk and a higher level of patient acceptance.

1.1 Motivation

Although the concept of CTC was initially proposed in 1994 (Vining *et al.*, 1994), it is not yet in widespread clinical use. The reason for this is partly due to insufficient training resources and a shortage of radiologists specialised in CTC. CTC is an advanced examination technique that involves some prerequisites related to the analysis and interpretation of CT data. However, most current radiologists in practice may not be familiar with these specialised interpretation skills. Therefore, dedicated training for CTC is required and the importance of the training has been emphasised by several radiology organisations (see Table 1.1). It is clear from this table that most organisations recommend that 50 to 100 endoscopically confirmed cases should be practiced before clinical participation in CTC data interpretation. This intensive training is the prerequisite for a radiologist to acquire proficiency in CTC.

Table 1.1: The specific number of CTC training cases recommended by various international radiologist organisations.

Organisation	**Document**	**Release date**	**Recommended number of training cases**
The American Gastrointestinal Association (AGA)	Standards for gastroenterologists for performing and interpreting diagnostic computed tomographic colonography	2007	≥ 75
The American College of Radiology (ACR)	ACR colon cancer committee white paper: Status of CT colonography	2009	≥ 50
The International Collaboration for CT Colonography Standards	CT colonography standards	2010	≥ 50
Canadian Association of Radiologists (CAR)	CAR CT colonography Standards	2010	≥ 50

Continued on next page

Table 1.1 – continued from previous page

Organisation	**Document**	**Release date**	**Recommended training cases**
The British National Health Service	Guidelines for the Use of Imaging in the NHS Bowel Cancer Screening Programme	2010	≥ 100
The Faculty of Radiologists in Ireland	Guidelines for Use of CT Colonography (CTC) as part of the National Colorectal Screening Programme in Ireland	2012	≥ 50

In order to teach CTC skills in an efficient and effective way, some experts have provided a number of suggestions. These suggestions are presented in Table 1.2.

Table 1.2: Selected expert suggestions for CTC training

Author	Study	Suggestion
Ericsson (2004)	Deliberate Practice and the Acquisition and Maintenance of Expert Performance in Medicine and Related Domains	Feedback based on performance is very important in the training programme and can motivate the participant to improve performance
Soto *et al.* (2005)	Reader training in CT colonography: How much is enough?	An intensive hands-on course conducted at reading workstations under the supervision of experienced radiologists
Slater *et al.* (2006)	Reader error during CT colonography: causes and implications for training	Emphasis on lesion detection could improve CT colonography performance
Taylor (2007)	A review of research into the development of radiological expertise: implications for computer-based training	Present some examples in the initial training and then use a large number of cases for hands-on training and provide clear feedback

Continued on next page

Table 1.2 – continued from previous page

Author	Study	Suggestion
Dachman *et al.* (2008)	Formative evaluation of standardized training for CT colonograhic image interpretation by novice readers	Lectures and hands-on training with feedback
Dachman (2008)	Success in virtual colonography depends on right training	

It can be concluded from this table that most researchers agree that hands-on training and appropriate feedback are the two most important aspects in CTC training. Based on these suggestions, most current CTC training is structured as a full two-day course in a specific centre. The first day consists of introductory lectures on performing CTC, observation of an expert reader interpreting several cases and an introduction to commercially available reading software. During the first day, trainees gain some basic skills in CTC interpretation. On the following day, a large number of hands-on cases are interpreted by the trainees in a simulated clinical scenario. These are actual clinical cases and the interpretation tool is the same as that used in a clinical environment. After interpreting each case, the trainee is unblinded to the gold standard and has an opportunity to meet with an experienced radiologist to obtain explanations of false-negative or false-positive interpretations, as well as some teaching points associated with the case. Some universities and organisations, such as Boston University, the Society of Gastrointestinal Radiologists and the American College of Radiology have recently provided CTC training courses based on this model.

There are two main drawbacks associated with the approach to CTC training outlined above and these can be summarised as follows:

- This training is extremely costly in terms of time and financial expense, particularly in relation to travelling and accommodation. In order to reduce the cost of trainees' transportation, a local training centre could be established in the absence of a more viable alternative. However, this could be inefficient due to redundant resources across multiple training locations.
- After dedicating two days to training, some novices can become competent CTC readers, however, others may not reach this level (Dachman *et al.*, 2008). In addition, lack of follow-up training after the initial two-day courses means there is little or no ongoing support for the trainees. In both cases, trainees may need additional CTC training.

In considering solutions to the problems mentioned above, the development of a software system that provides remote access to CTC training material as well as automatically evaluating reading performance is a desirable approach. This is motivated by the fact that improvements and advances in Internet and computer technologies facilitate the provision of a straightforward and cost-effective training experience. The remote training approach can significantly reduce the difficulties associated with CTC accreditation and provide the trainee with an ongoing opportunity to maintain clinical expertise in CTC after undergoing their initial training.

Such a remote access system requires several key features in order to deliver a comprehensive CTC training experience. Firstly, the training should be provided in a clinical scenario to offer the trainee hands-on experience. In this case, the complete CTC data set should be available for the user. The reason for this is that when performing CTC examinations in practice, a radiologist has to read hundreds of CT slices from a volumetric data set, instead of relying on a few specific slices. In addition, both 2D and 3D interpretation tools should be provided in the training system. Pickhardt *et al.* (2007) demonstrated that in the case of CTC, reader performance could be improved in the aspects of sensitivity and interpretation time if 3D functions were available. Therefore, 3D visualisation plays an important role in facilitating an accurate interpretation of CTC images in a clinical environment and hence should be available in the training system. Furthermore, as suggested in Table 1.2, feedback is important in enhancing learning and performance during the training. This feature should be incorporated into the overall CTC training system. In addition, in order to maximise the potential user base, the system should be designed to be operated on a low-cost client machine with the following minimum requirements: a 2.8 GHz processor with 512 MB of RAM and a 1 GB hard disk. Utilisation of such a training strategy could provide an always-on and always-available teacher. However, this kind of CTC training is not currently available.

1.2 Technical Challenges

Dachman *et al.* (2008) described a standardised hands-on CTC training process as follows. A full CTC data set is provided to users and then they use 2D tools, such as windowing and zooming, as well as 3D visualisation functions to assist in the interpretation and analysis of the data set. Feedback about the training session is ultimately provided after the interpretation of a CTC data set has been completed. This feedback includes some explanations on false-negative or false-positive polyps and teaching points associated with the case. Provision of this information allows the user to learn from his/her mistakes and be aware of his/her progress during the training process. The only difference between remote access CTC training and local CTC training is the transmission of CTC data sets to the client. Slomka *et al.* (2000) demonstrated that transmission of the whole 3D medical data set to the user could dramatically reduce network traffic due to a reduction in client-server communications and hence provide a short response time for remote viewing and processing of the data set. According to their study, it is preferable to download the full data set to the client so as to offer a short response time for client operations. Integration of this strategy into the existing CTC training process creates a hybrid remote access training process which is illustrated in Figure 1.2. When launching the CTC training system, the first step is to download the relevant data set to the client. Once the download is complete, the remote access training session is implemented in the same way as the local training process.

Based on this training process, a remote access CTC training system comprises of server- and client-side components. The server-side component is responsible for retrieving the required study from a repository of studies and sending the associated data to the client. The client-side component is a comprehensive medical imaging application which sends the request for downloading the selected data set to the server, displays the downloaded images, provides a set of interpretation tools such as windowing and volume rendering, and ultimately allows the user to send their polyp selections back to the server for evaluation (see Figure 1.3).

In order to develop such a remote access training system, the first challenge that needs to be addressed is the transmission time required to send a large amount of data to the client. The increasing size of volumetric CTC data sets as well as practical limitations in transmission bandwidth make real-time delivery a key challenge. In general, CTC is performed with the patient in both the supine (facing up) and prone (facing down) positions. Both image data sets are

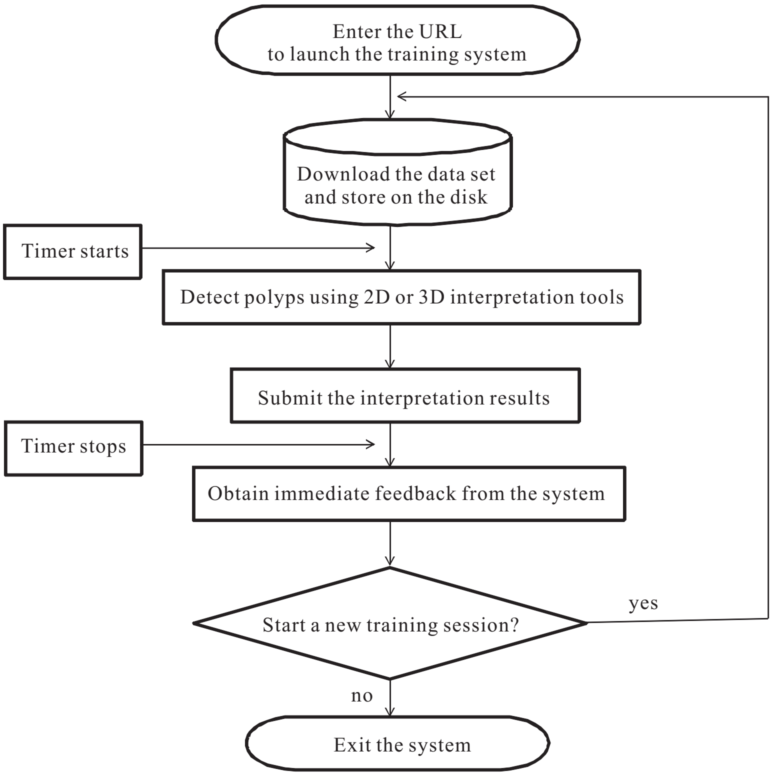

Figure 1.2: Outline of the main steps for remote access CTC training.

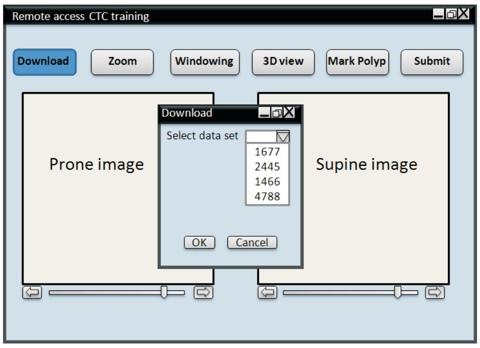

Select data set
1677
2445
1466
4788

a) selecting a case

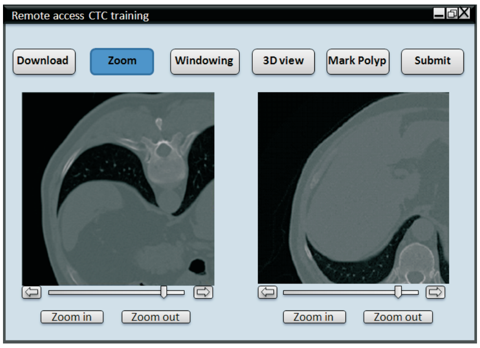

b) zooming in/out

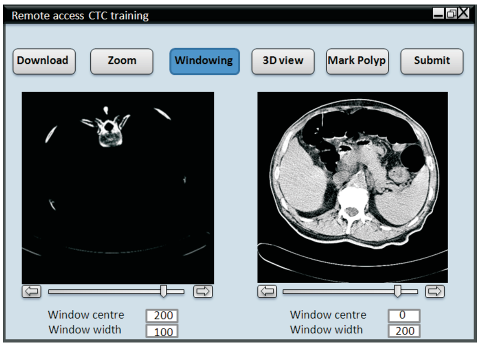

Window centre 200
Window width 100

Window centre 0
Window width 200

c) windowing

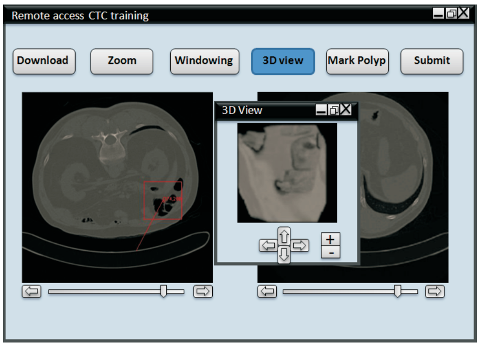

d) 3D visualisation

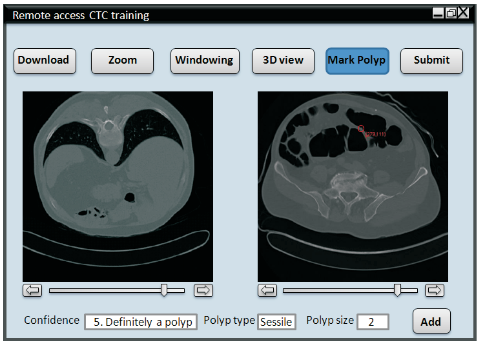

Confidence 5. Definitely a polyp Polyp type Sessile Polyp size 2

e) polyp marking

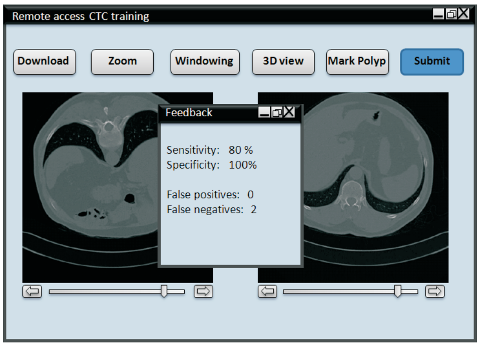

Sensitivity: 80 %
Specificity: 100%

False positives: 0
False negatives: 2

f) feedback provision

Figure 1.3: An overview of a comprehensive graphical user interface for a remote access CTC training system.

critical in order to provide comparable views to confirm pathology. Normally, a single CTC data set is between 150 and 200 Megabytes and hence the size of both prone and supine data sets is around 300 to 400 Megabytes. Based on the typical download speed, it takes a significant amount of time to complete data delivery for one patient. A long delay definitely discourages the use of remote access CTC systems. The instinctive solution to the long delay is to increase the network bandwidth or to compress the data set or to do both. However, narrow-band connections will probably not be completely eliminated in the near future. As a result, the only current viable solution is the development of an optimal compression technique to facilitate efficient transmission of CTC data sets.

Additionally, as previously described, 3D rendering is a necessary interpretation tool in a training system. This functionality should be provided for users. However, 3D rendering, especially in the case of volume rendering, is a computationally intensive process that is usually implemented on a dedicated workstation with hardware acceleration. There is a significant delay associated with the time required for volume rendering when it is implemented on a low-cost PC platform. A potential solution to this problem is to perform server-side volume rendering. The rendered image is then sent back to the client. However, this solution suffers from a heavy dependence on network performance and possible performance degradation when multiple clients access the server simultaneously. In order to overcome these shortcomings, it is preferable to implement client-side volume rendering so as to offer stable performance during the training process. Consequently, this gives rise to a further challenge related to remote access CTC, as it is difficult to achieve fast volume rendering on a standard PC platform.

Motivated by these challenges, the development of optimised solutions for data delivery and 3D visualisation represent the major topics that are addressed in this thesis.

1.3 Contributions

The central aim of the research outlined in this thesis is to develop a theoretical framework which can provide efficient CTC training in a remotely-accessible fashion. In order to deliver this training, the entire medical data set should be available for the user. As mentioned in Section 1.2, transmission of a CTC data set via the Internet is particularly time-consuming. In addition, the large size of medical data sets could result in 3D operations being extremely slow when implemented on a standard PC platform. Addressing all these challenges forms the set of major contributions that are presented in this thesis and these major contributions are summarised as follows:

- To develop a lossless medical image compression method that exploits the inherent characteristics of medical data sets to improve the level of compression that can be achieved. This method is subsequently integrated into a delivery scheme that allows transmission speed to be increased significantly without losing any information.
- To develop a real-time rendering technique capable of generating a high-quality volume rendering of a region of interest within a medical data set on a low-cost PC platform.

Additional contributions can be found in a novel edge-based prediction method and a new 3D normal operator for use in the domain of data compression. Furthermore, a new trilinear interpolation operator is developed in order to achieve fast volume rendering. A generic framework for remote access CTC is created incorporating of all these contributions and is shown to provide a high level of functionality, interactivity and usability.

1.4 Thesis Organisation

The remainder of this thesis is organised as follows:

Chapter 2 reviews the existing techniques in the field of volume rendering and medical image compression. The main conclusions resulting from this review are discussed.

Chapter 3 describes an improved volume rendering technique. In this chapter, each acceleration approach integrated into the developed technique is discussed in detail. The main novelty of the developed technique is utilisation of the characteristic properties of CTC data to enable a software-based acceleration approach. A quantitative and qualitative evaluation was conducted to assess the performance of the proposed method.

Chapter 4 presents a new segmentation technique which has the ability to identify specific anatomical regions in a CTC data set. This is achieved by utilising density and anatomical features. A tailored version of this segmentation technique is then developed for use in the preprocessing stage of the compression scheme. The performance of this version of the technique is ultimately evaluated by comparison with the manually labelled ground truth data for specific anatomical regions.

Chapter 5 presents a novel prediction model based on the developed segmentation technique. This model consists of a series of predictors optimised for each anatomical region. To generate these predictors, there are two different modelling approaches to deal with interior regions and edge regions, respectively. The first approach, designed for interior regions, is based on an optimised prediction template to create the predictor. The second approach for dealing with edges considers different contexts based on the edge direction, in order to generate an appropriate predictor for each context. The decorrelation performance of the proposed prediction model is benchmarked against several of the prediction methods that are currently available.

Chapter 6 evaluates the performance of the complete compression scheme, including both decorrelation and entropy coding stages. In this chapter, several entropy coding methods are evaluated in order to determine the most efficient technique. The complete compression scheme is generated by combining the most efficient entropy coding technique with the previous prediction model. An evaluation of the complete scheme is conducted on a large number of CTC data sets. The main focus of this chapter is placed on the development of an efficient delivery scheme for medical image data. An optimal delivery solution that integrates the developed compression method is ultimately presented. As the results show, the proposed delivery scheme can reduce the delivery time by nearly two thirds of original download time at the typical connection speed available in Ireland.

Chapter 7 presents the whole framework for remote access CTC training and highlights the optimised components resulting from this research. Initial implementation of the framework is also presented in this chapter which demonstrates the feasibility of the proposed framework for the provision of remote access CTC training.

Chapter 8 summarises this research, outlines the resulting contributions, and provides some further research directions related to the compression and volume rendering contributions.

Chapter 2

Literature Review

The aim of this chapter is to present the background of the research discussed in this thesis. The main techniques in the fields of volume rendering and image compression will be presented with specific focus on the medical imaging applications in these fields.

2.1 Volume Rendering

Volume rendering is an advanced technique for the visualisation of 3D data. It involves a number of technologies, i.e. image processing, computer vision and computer graphics, for displaying a 2D projection of a data set. Research on volume rendering began in the 1970s, at approximately the same time as the development of *Computed Tomography* (CT), *Magnetic Resonance Imaging* (MRI) and other medical imaging modalities.

Over the course of the past four decades, several volume rendering algorithms, such as ray casting and splatting, have been developed for the visualisation of volumetric medical data. These algorithms can be roughly classified as either direct or indirect volume rendering methods (Deserno, 2011) and can be summarised as follows:

- Direct volume rendering (simply called volume rendering) involves mapping each sample value to an opacity and a colour. The final image is an accumulation achieved by compositing these filtered samples. This procedure allows all the voxels in a data set to be visualised.
- Indirect volume rendering (also called surface rendering) is a process that extracts a polygonal representation of an object within a 3D data set and then generates a model based on the extracted surfaces. This type of algorithm only displays the outermost surface of a target object without dealing with the inner parts.

Based on the above descriptions, it is clear that indirect volume rendering is limited in that only a presegmented surface can be presented in the rendered image. The information beneath the surface cannot be visualised. On the other hand, direct volume rendering does not extract a surface from the data and instead incorporates all the data to generate the rendered image. Thus, direct volume rendering has the potential to visualise the complete data set. More importantly, this algorithm can map the original data to different colours and opacities. This feature enables interactive segmentation of the data and requires no preprocessing. The use of direct volume rendering techniques in the process of image interpretation can greatly help the radiologist to identify important diagnostic information. Therefore, this review focuses on state-of-the-art direct volume rendering techniques. However, the main disadvantage of the algorithms in this category is high computational complexity which leads to poor performance (Calhoun *et al.*, 1999).

The following subsections explain in detail the basic direct volume rendering algorithms and then discuss a number of optimisation techniques that address the speed problem. The specific volume rendering techniques designed for use with CTC are reviewed in Section 2.1.3.

2.1.1 Basic Algorithms

Four algorithms are commonly used in volume rendering: ray casting, splatting, shear-warp and 3D texture-mapping.

2.1.1.1 Ray Casting

Ray casting is an image-based volume rendering technique, which casts a ray from each pixel in the viewplane through a 3D data set, as shown in Figure 2.1. Equidistant sampling and trilinear interpolation are then used along the part of the ray that lies within the data set to determine the sample point value from the surrounding voxels. The final image is generated from the composition of all sample points along each ray (Levoy, 1988).

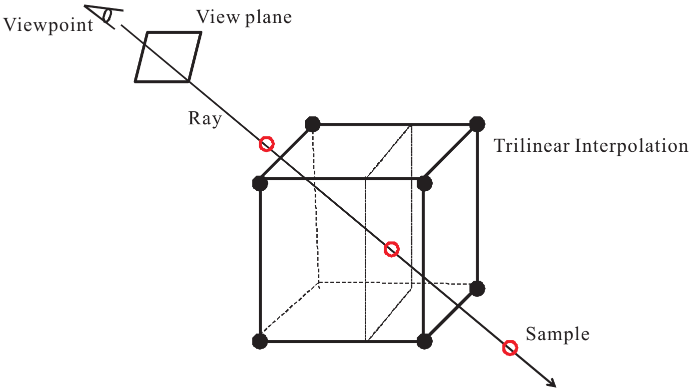

Figure 2.1: An illustration of ray casting. A ray starting from a viewpoint is cast through the volume.

The composition operator is based on Equation 3.8:

$$C_{out} = C_{in}(1 - \alpha) + C\alpha \tag{2.1}$$

where C_{out} defines the accumulated colour emerging from the current voxel, C_{in} denotes the accumulated colour going into the current voxel, α represents the opacity at the current voxel and C is the colour of the current voxel.

This compositing process is illustrated in Figure 2.2. Due to the generality of this composition method, it is also applied in other volume rendering techniques.

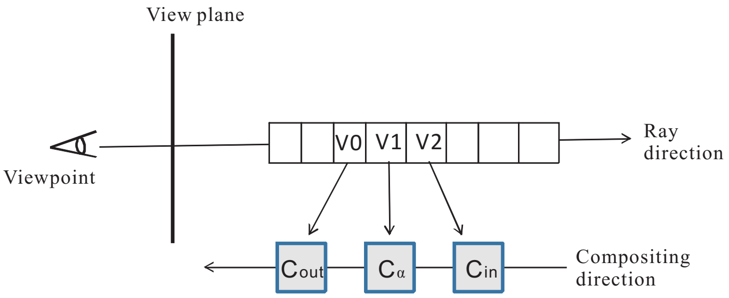

Figure 2.2: The ray compositing process in volume rendering.

The key advantage of ray casting lies in its high-quality rendering result. However, each voxel needs to be processed several times and each time the direction of observation is changed this technique has to resample the entire data set. These facts mean that the procedure is extremely expensive from a computational perspective.

2.1.1.2 Splatting

Splatting is an object-based technique (Westover, 1989), which imitates throwing snowballs at a wall where each snowball "splats" on the wall, leaving a diffusion trace (see Figure 2.3). The final image is an accumulation of these distributions.

The accumulation of distributions in this technique is based on a reconstruction kernel in a convolution operation. This reconstruction function is calculated in a preprocessing stage and the results can be stored in a look-up table. Therefore, it is easy to calculate the contribution of each voxel to the image plane by

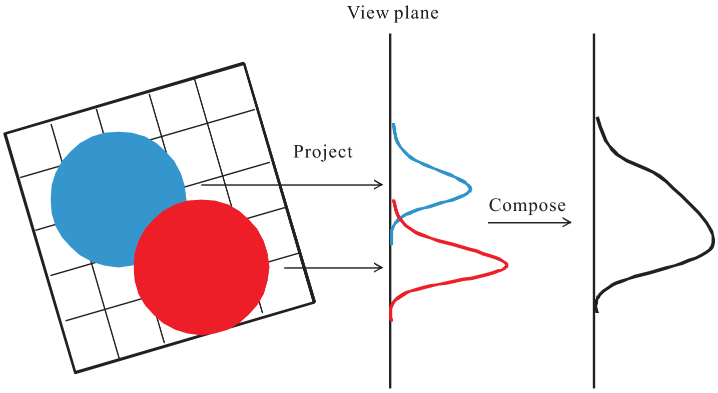

Figure 2.3: An illustration of splatting. Each voxel is projected onto the image plane using a footprint.

consulting the look-up table. This technique is fast, but quality is sacrificed for speed due to the approximation of each voxel's contribution.

2.1.1.3 Shear-warp

Shear-warp is a hybrid algorithm which integrates the features of both image-based and object-based rendering approaches (Lacroute & Levoy, 1994). The procedure can be illustrated in the following three steps:

1. The original data set is transformed into sheared object space by translating and resampling each slice (see Figure 2.4).
2. The resampled slices are projected into a 2D intermediate image in front-to-back order.
3. The intermediate image is transformed to image space by warping so as to generate the final image.

The amount of computation involved in this algorithm is greatly reduced compared with the ray casting and splatting methods as only two resampling

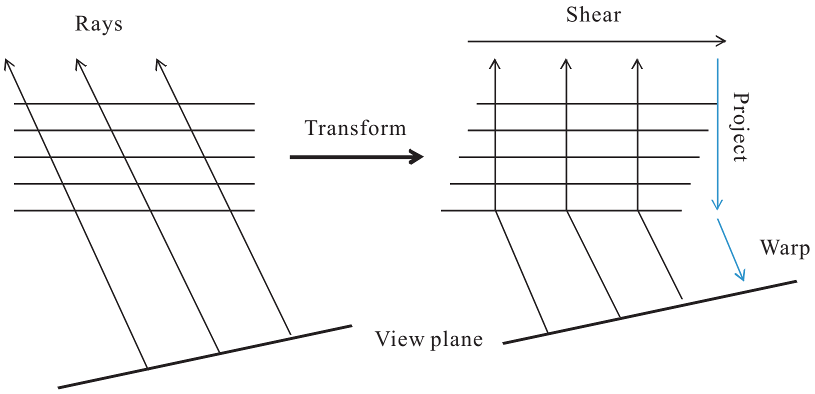

Figure 2.4: A demonstration of the three stages of the shear-warp method.

processes of the whole data set are required. However, this technique has some deficiencies. For example, aliasing occurs when the viewing angle is a multiple of 45^o and, once enlarged, the image is blurred.

2.1.1.4 3D Texture-mapping

The previous three algorithms attempt to implement volume rendering using software. However, the most recent volume rendering algorithm, 3D texture-mapping, is a hardware-based approach, supported by specialised computer graphics hardware (Cabral *et al.*, 1994).

In this approach, the data set is first loaded into texture memory as a 3D texture map. Then, it is resampled into polygonal slices perpendicular to the view direction. This slice data is converted to the corresponding colour values and opacity values using a look-up table. The final step is to compose this data in back-to-front order. In the texture space, the interpolation and composition operations are accelerated by the *Graphics Processing Unit* (GPU) hardware.

However, a significant disadvantage associated with this technique is a heavy dependence on hardware. With the increasing size of medical image data sets, there is a need for powerful hardware to implement this technique. In addition, the rendering quality of this approach has been proven to be inferior to that achieved by the ray casting and splatting algorithms (Alakuijala *et al.*, 1996).

2.1.2 Acceleration Techniques

Among the various volume rendering algorithms, ray casting is one of the main techniques used in the medical domain due to its high quality rendered images. However, this technique is highly computationally intensive resulting in poor performance. A number of researchers have proposed many acceleration methods for ray casting. These approaches can be categorised into two main groups: software-based and hardware-based methods. This section concentrates on a review of software-based acceleration methods. This is motivated by the fact that the software-based acceleration methods are a low-cost and widely available solution to address the speed issue associated with the ray casting approach.

A simple but effective software-based acceleration technique is early ray termination (Levoy, 1990). There are two situations in which a sampling process can be stopped early. The first is when the accumulated opacity reaches one unit and the second is when the ray has left the volume. This acceleration method can efficiently reduce the time required for ray casting, thus it is commonly used in volume rendering techniques.

Alternatively, acceleration can be achieved by adaptive sampling. Based on the observation that oversampling commonly occurs at the area close to the viewpoint in the case of perspective projection, Novins *et al.* (1990) proposed an acceleration approach to avoid the unnecessary computational time caused by oversampling. Their approach started with a small number of rays. When the sampling rate was less than the volume resolution, the ray would split into four divergent rays to increase the sampling density. This progressive sampling technique reduced the execution time of ray casting, while preserving the rendering quality. Based on the same observation, Brady *et al.* (1998) divided the sample points into several regions according to the distance from the viewpoint. There were fewer rays in the region nearer the viewpoint. The number of rays would then increase as the distance from the region to the viewpoint increased. Both methods were able to avoid the loss of information that was further away from the viewpoint, while reducing the sampling time in the area near the viewpoint.

Another important type of volume rendering acceleration approach is space leaping (Yagel & Shi, 1993). This method is used to skip the empty space surrounding the target object in an efficient manner. For example, in the case of CTC, most regions in CTC data sets comprise air, soft tissue and fat, as shown in Figure 2.5. The areas associated with air and fat can be seen as empty regions due to the fact that the information in these regions is not useful for colon cancer detection. Skipping these empty regions to reach the soft tissue directly is more time efficient, as illustrated in Figure 2.6.

Many researchers (Levoy, 1990; Kruger & Westermann, 2003) have attempted to propose efficient space leaping approaches. An initial method is based on the hierarchical representation of volumetric data. In such a representation, a ray traversal algorithm can skip the empty space by inspecting each node of the hierarchy, rather than a voxel by voxel investigation. Early research into such acceleration techniques was conducted by Levoy (1990). He used hierarchical spatial enumeration to decompose the data and demonstrated that incorporating early termination and space leaping approaches into ray casting algorithms could reduce the rendering time by 80%. Motivated by this significant reduction with respect to the execution time of ray casting, several studies applied different hierarchical structures to obtain further improvements, i.e. octree (Kruger & Westermann, 2003), orthogonal binary space partitioning tree (Li *et al.*, 2003) and k-dimensional tree (Vidal *et al.*, 2008).

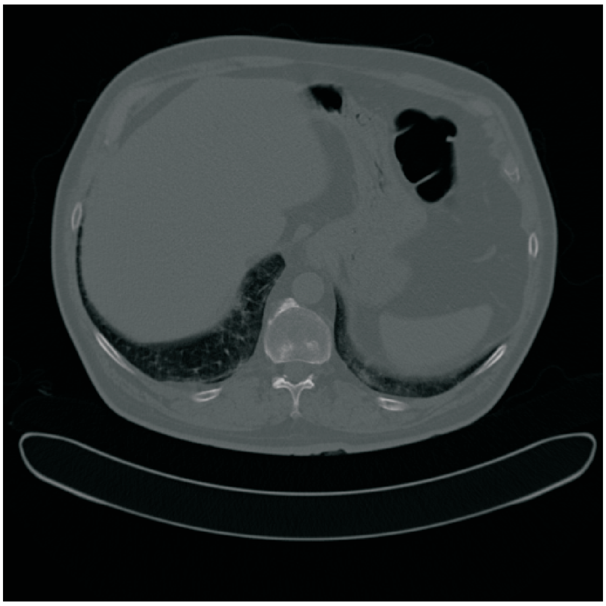

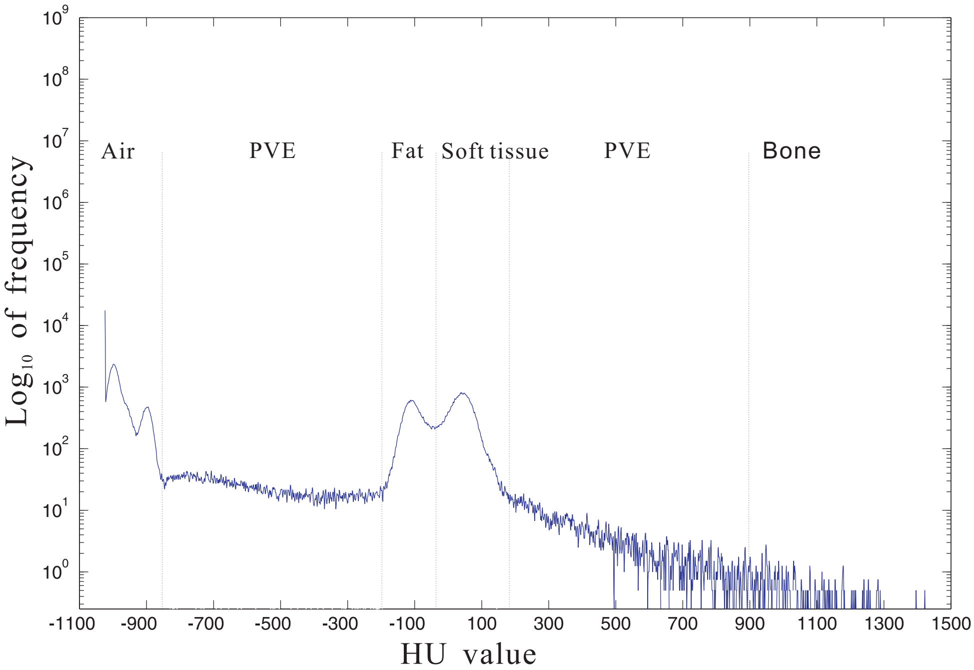

Figure 2.5: A sample CT image and its histogram.

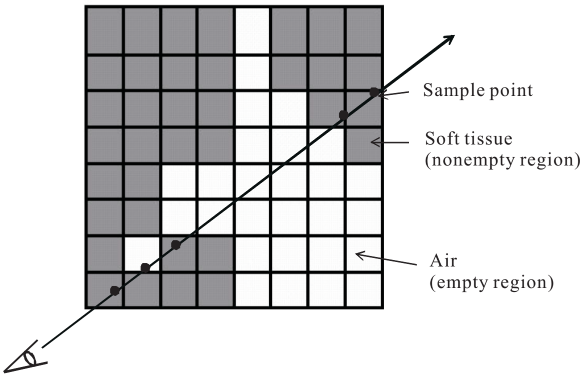

Figure 2.6: An illustration of skipping empty areas within the colon.

Another technique used for space leaping is referred to as proximity clouds (Cohen & Sheffer, 1994) which is a distance map-based method. It precalculates the distance from an empty voxel to its nearest boundary and stores it as a distance map. When the ray encounters an empty voxel, it can safely make a leap forward to skip a number of empty voxels based on the predefined map. However, the size of the ray step depends not only on the predefined distance value, but also on the ray direction. Figure 2.7 gives a 2D example of a distance map and presents the process of a ray skipping the empty areas based on the information stored in the distance map.

As shown in Figure 2.7, let A(x_1,y_1) and B(x_2,y_2) be two points on the ray. The vector of the ray is (V_x,V_y) and the distance value of A is R based on the distance map. The value R indicates how far the point A is from a surface boundary. Thus, the maximum step size at point A is R and the sequential point B along the ray is calculated as

$$x_2 = RV_x + x_1 \tag{2.2}$$

$$y_2 = RV_y + y_1 \tag{2.3}$$

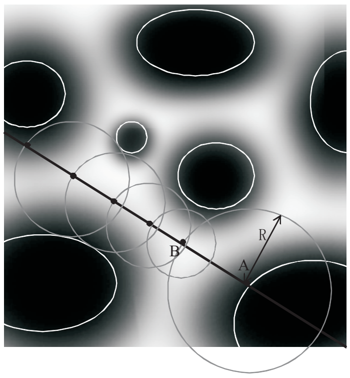

Figure 2.7: A ray traversing a slice from a volumetric data set based on the proximity clouds technique.

In order to avoid the calculation of each step size and to obtain a further improvement in efficiency, Lim & Shin (2008) introduced an advanced distance map to facilitate empty space skipping. In their map, the distance for each empty voxel was precalculated with respect to all potential forward directions. Thus, the ray can move forward directly to the boundary voxels by referencing a precalculated step size.

There are a number of other space leaping techniques in addition to those based on hierarchical representations and proximity clouds. Wan *et al.* (1998) proposed a boundary cell-based acceleration technique that located the boundary of a target object in the preprocessing stage. When implementing ray casting, their technique only required a short time to calculate the skip distance for each ray. Fung & Heng (1998) proposed a space leaping approach to skip not only empty space but also homogeneous regions. In their approach, they used a new data representation form, which they refer to as an isoregion, to efficiently store homogeneous voxel cubes. The sample points within this isoregion were then preaccumulated. Thus, when the ray encounters these homogeneous isoregions, there is no need to execute accumulation and transparency calculations, reducing the computational complexity of the volume rendering procedure. Lakare & Kaufman (2004) exploited the coherence between the current ray and its neighbouring rays to implement fast space leaping. Based on their observation that a group of rays often traversed the same distance before reaching the target object, it was possible to use the skipping information from previous rays to guide fast leaping across the empty space for the current ray. Their experimental results indicated that this technique was efficient and accurate. Çelebi & Çevik (2010) proposed a backward steps method to efficiently skip empty spaces. In their approach, the ray did not step one unit at a time; instead, it stepped by a predetermined number of units. The sample point would be moved back by the predefined size when the boundary of interest was encountered. This method was capable of traversing empty regions at high speed without losing any information. Qing *et al.* (2010) applied a bounding box technique to enable the ray to reach the target object directly. In their preprocessing stage, they built a bounding box to locate the target object and recorded the coordinates and the size of the box. When the ray traversed a data set, it was able to jump over the area outside the box and begin the sampling process until the ray intersected the bounding box.

When implementing interactive volume rendering techniques, it is also possible to exploit the coherence between consecutive frames to detect empty areas quickly. Yagel & Shi (1993) introduced a coordinates-buffer to store the location of the first non-empty voxel for each ray according to the previous rendering result. The depth value of the pixel in the current image plane was then calculated based on the reprojection of the first non-empty voxel to the image plane. The depth value refers to the distance that a ray travels to reach the object boundary. However, the reprojected point on the image plane is usually not aligned with the integer pixel grid and thus the calculated depth value has to be assigned to the nearest pixel. In this case, there must be some pixels on the image plane that have no depth value. For these pixels, the normal ray casting technique has to be performed which increases the rendering time. In order to solve this problem, Wan *et al.* (2002) proposed a cell-based projection technique which projects the boundary areas rather than the exact pixels to the image plane. This technique could significantly reduce the number of pixels that have no depth value.

2.1.3 Methods Designed for CTC

All of the above acceleration techniques were proposed for general volume rendering. However, volume rendering for CTC is a special case as the colon has some unique characteristics, such as a cavity structure and a thin surface. In addition, a volume rendering technique for use with CTC must have some specific features. Firstly, perspective rendering is a critical requirement (Rubin *et al.*, 1996). There are two basic types of rendering projections, namely perspective projection and parallel projection. In perspective projection, the centre of projection is at a finite distance from the viewplane, and in parallel projection the centre of projection lies at an infinite distance. As a result, perspective projection renders objects with depth and distance, where objects closer to the viewplane appear larger than objects farther away the viewplane. Parallel projection, on the other hand, cannot provide this depth information. An illustration of these two projection methods is provided in Figure 2.8. Perspective projection works in the same way as the human visual system and hence this type of rendering simulates an endoscopist's view of internal structures which can produce more realistic colonic images than parallel rendering. Secondly, the movement of the viewpoint (camera) should be fully interactive in order to allow the user to observe the structure as desired. Finally, the rendering speed should be acceptable in order to improve the radiologist's efficiency and productivity. Due to these facts, it is necessary to tailor a CTC volume rendering technique so that it satisfies all of the above requirements.

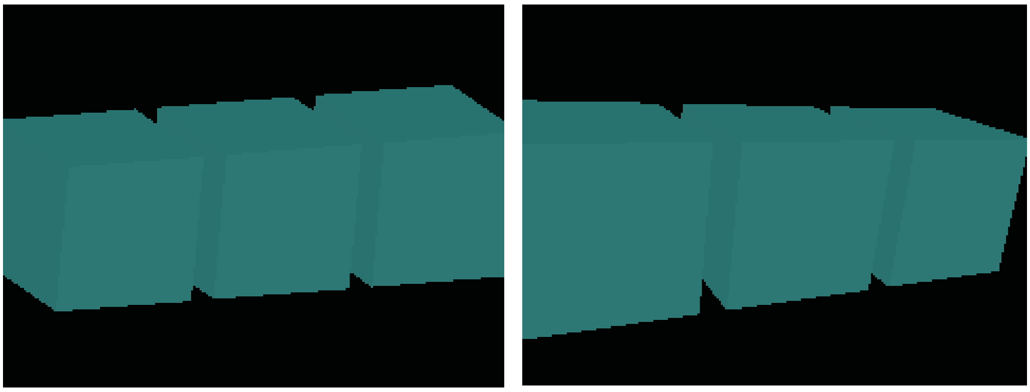

Figure 2.8: Examples of parallel (left) and perspective (right) projections.

Recently, a number of specific volume rendering methods in the context of CTC have been developed by the Center for Visual Computing (CVC) at the State University of New York. The CVC group initially developed a technique for interactive navigation within the colon based on surface rendering (Hong *et al.*, 1997). This technique provides an overview of the inner surface of the colon in order to facilitate the detection of abnormalities on the surface. Once the potential abnormalities are detected, a detailed study and analysis of the tissues beneath the colonic surface is required (You *et al.*, 1997). However, this feature is not possible in the case of surface rendering. On the other hand, the volume rendering techniques have the ability to provide a flexible visualisation of the interior structures of polyps and other abnormalities. Utilisation of this technique can help the radiologist to distinguish between benign and malignant lesions. Based on this fact, the CVC group improved the initial navigation system by the introduction of direct volume rendering (You *et al.*, 1997). In order to achieve interactive rendering speeds, their new volume rendering algorithm utilised a surface-assisted ray casting approach. This approach extracted the colonic surface in the preprocessing stage and used this surface information to efficiently locate the first sampling point for each ray. With the integration of hardware acceleration, this improved system could provide a fast volume rendering process for CTC. One of the major disadvantages of this system is the significant overhead associated with the identification of the colon surface. In order to address this issue, Wan *et al.* (1999), members of the same group, developed a potential-field-assisted ray casting approach. This approach incorporated the proximity clouds technique into the volume rendering process to efficiently skip the empty space within the colon. Their experimental results showed that, based on the parallel implementation, this new method was faster than the surface-assisted ray casting method. More importantly, it does not have a significant overhead for surface extraction. The systems described above all required workstation computers with hardware acceleration. In order to improve the availability of the system for low-cost PCs, the CVC group integrated a volume-rendering PC board, called VolumePro [1], to implement fast volume rendering on PC platforms (Wan *et al.*, 2000; Li *et al.*, 2001). The VolumePro board has the ability to provide very high frame rates. However, it has a limited amount of memory and only supports parallel volume rendering. The CVC group solved these problems by rendering with subvolumes and applying an adaptive perspective projection simulation. With the help of the VolumePro board, this new system could achieve real-time volume rendering performance even on a standard PC platform. Subsequently, Dachille *et al.* (2001) compared their previous workstation-based system and the VolumePro board-based system, in terms of the quality of the volume rendering results and the execution time. Both systems were capable of providing interactive navigation within the colon and demonstrated the same rendering quality. This result shows that a specialist hardware-based solution is a viable option for the use of volume rendering in CTC on standard PC platforms.

---

[1] VolumePro is a graphics card that can provide high-speed volume rendering.

Motivated by the same reason, Lee *et al.* (1999) also developed a low-cost PC-based CTC visualisation system which incorporated automatic colon segmentation, navigation path generation and fast surface rendering. However, they used surface rendering, instead of volume rendering, which limited the diagnostic capability of their system.

2.1.4 Discussion

It is clear from Sections 2.1.2 and 2.1.3 that the speed problem associated with volume rendering has received a great deal of attention and a considerable number of acceleration techniques have been described in the literature. These techniques are briefly summarised (where possible) in Table 2.1.

This table illustrates that the volume rendering techniques reviewed above are generally either unsatisfactory in terms of speed or not applicable in the case of a standard PC platform. Although Wan *et al.* (2000) and Li *et al.* (2001) attempted to implement real-time volume rendering on a low-cost PC platform, their approaches still require specific volume-rendering hardware. On the other hand, the existing software-based volume rendering approaches have far from real-time performance when deployed on a standard PC platform. It is clear from this observation that there is a need for a low-cost PC-based system that is capable of providing real-time volume rendering of CTC data without any specialist hardware. Chapter 3 presents such a system which is based on an improved ray casting technique designed specifically for use with CTC.

2.2 Medical Data Compression

Data compression is one of the main research topics in the area of medical imaging and has been investigated intensely for more than two decades (Wong *et al.*, 1995).

Table 2.1: An overview of previously published volume rendering techniques

Author(s)	Method	Data set	Image plane	Hardware	Time (seconds)
Novins *et al.* (1990)	Split rays to achieve progressive sampling	119 × 112 × 73	256 × 256	Hewlett-Packard 835 workstation	356
Wan *et al.* (1998)	Pre-locate boundary to assist skipping	50 × 50 × 50	256 × 256	SGI Power Challenge with 16 R 10000 processors, 3GB RAM	1.85 (parallel)
Brady *et al.* (1998)	Increase the number of rays to achieve progressive sampling	256 × 256 × 154	160 × 160	Intel Pentium II, 300 MHz, 256MB RAM, NeTpower ULTRAfx2TM graphics accelerator card	1.48
Fung & Heng (1998)	Homogeneous region leaping	256 × 256 × 256	256 × 256	Sun Ultra 1/170, 512MB RAM	2.63
Wan *et al.* (2002)	Pre-store the non-empty cells to achieve fast skipping	512 × 512 × 107	256 × 256	16-processor SGI Power Challenge	0.06 (parallel)
Lakare & Kaufman (2004)	Light weight space leaping using ray coherence	512 × 512 × 361	256 × 256	Pentium-IV 2.6 GHz, 1GB RAM	0.16
Designed for use in CTC					
You *et al.* (1997)	Surface-assisted ray casting	512 × 512 × 358	128 × 128 256 × 256 512 × 512	16-processor SGI Power Challenge	0.06 0.25 1.01 (parallel)
Wan *et al.* (1999)	Potential-field-assisted ray casting	512 × 512 × 411	256 × 256 512 × 512	16-processor SGI Power Challenge	0.09 0.36 (parallel)
Wan *et al.* (2000)	Utilise a volume-rendering PC board	-	-	VolumePro board	< 0.04

This has been motivated by the fact that efficient compression of medical images plays a key role in the storage, transmission, and management of these images.

As indicated in previous reviews on medical image compression (Wong *et al.*, 1995; Strintzis, 1998; Menegaz, 2006; Ukrit *et al.*, 2011), the existing compression approaches can be classified into two main groups: lossless compression and lossy compression. Figure 2.9 depicts a development timeline of medical image compression techniques. It is clear that prior to 2010 medical data was mainly compressed in a lossless way, such as lossless prediction coding and lossless transform coding. However, modern imaging modalities generate a huge amount of medical data, creating a heavy burden on both storage and access. Consequently, lossy compression techniques have recently been used to increase transmission speed and save storage space. These techniques either compress the whole image in a lossy way or compress the region of interest in a lossless way while lossy compression is applied to the remaining areas. Although these techniques yield high compression ratios, they can result in the loss of crucial diagnostic information. Hence, many medical organisations, e.g. the U.S. Food and Drug Administration and the Royal Australian and New Zealand College of Radiologists, strongly recommend the use of lossless compression for the purpose of accurate diagnosis. Consequently, the research outlined in this thesis focuses solely on lossless compression techniques. The following subsections review some of the most widespread lossless image coding algorithms that have been used to compress medical image data.

2.2.1 Predictive Coding

Predictive coding is one of the earliest compression techniques used in the field of medical imaging (Wong *et al.*, 1995). It is based on the analysis of spatial distributions and relationships between the current pixel and its neighbours to

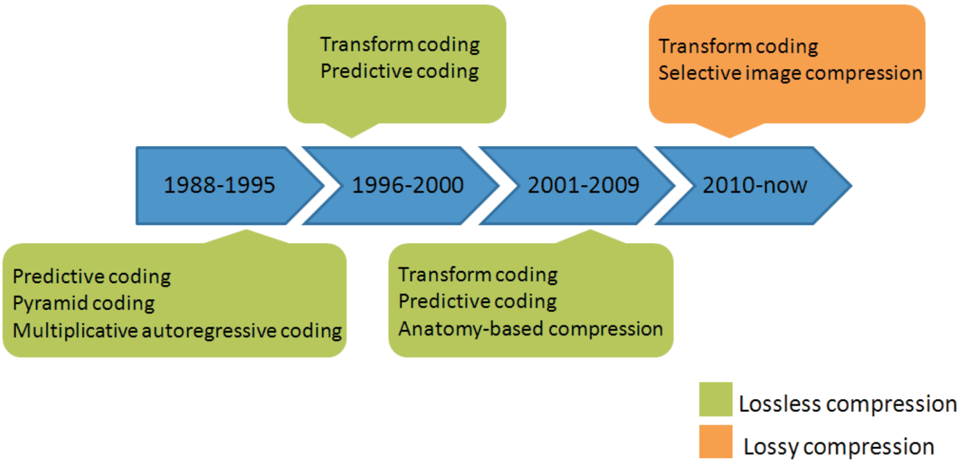

Figure 2.9: A development timeline of medical image compression techniques.

predict the current pixel value. This technique includes two major stages: the first is prediction modelling, for the purpose of data decorrelation, the second is entropy encoding of the decorrelated data (see Figure 2.10). If the data decorrelation stage is effective, a significant improvement in the performance of entropy coding can be achieved. Therefore, one of the key challenges in this compression technique is to generate an accurate prediction model.

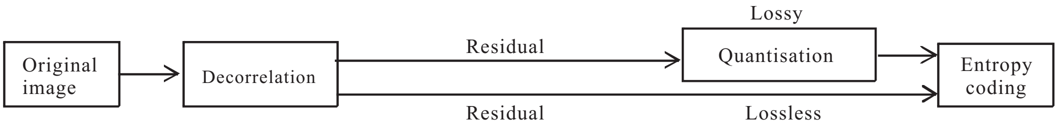

Figure 2.10: A block representation of a general predictive coding method.

In the initial studies of medical image compression, differential pulse code modulation (DPCM) was one of the most widely used prediction techniques (Bramble, 1989; Rabbani & Jones, 1991; Kuduvalli & Rangayyan, 1992). This prediction technique combines several previously encoded pixels with fixed coefficients to generate the prediction model. After the data is decorrelated, Huffman coding (Huffman, 1952), arithmetic coding (Witten *et al.*, 1987) or Lempel-Ziv coding (Lempel & Ziv, 1977; Ziv & Lempel, 1978) is used to further reduce the statistical redundancy in the residual data. In order to achieve a higher compression ratio, Ramabadran & Chen (1992) improved conventional predictive coding by introducing a context model before the entropy coding stage. Their results showed that the improved version of predictive coding could achieve 20% to 30% higher compression ratios than the conventional method.

Recently, predictive coding has enjoyed a resurgence of interest in the medical imaging domain due to its various forms and excellent performance. Ait-Aoudia *et al.* (2006) and Avramović & Savić (2011) introduced some of the most recent prediction models used for general image compression into medical image coding and evaluated the performance of these models using volumetric medical data. The experimental results in both papers showed that general prediction models were applicable in the case of medical image compression and these models significantly improved the overall compression results. The remainder of this section discusses the three main types of prediction models, which are JPEG-based methods, context-based adaptive methods and least-square (LS) -based adaptive methods.

1) JPEG-based methods

The most popular prediction model for 2D image compression is based on a series of JPEG-based predictors. The predictor combines three neighbours P_W, P_N and P_{NW}, as illustrated in Figure 2.11, to produce prediction results. There are seven predictors that can be used to estimate the value of the current pixel X based on these three neighbours (Wallace, 1991). These predictors are outlined in Table 2.2 and an illustration of the three neighbours is provided in Figure 2.11.

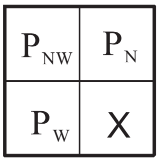

Figure 2.11: The pixel neighbourhood used to predict the value of X in JPEG compression.

Table 2.2: The seven JPEG predictors used to estimate the value of the current pixel based on its neighbours P_W, P_N and P_{NW}.

Predictor	**Prediction**
1	P_W
2	P_N
3	P_{NW}
4	$P_W + P_N - P_{NW}$
5	$P_W + (P_N - P_{NW})/2$
6	$P_N + (P_W - P_{NW})/2$
7	$(P_W + P_N)/2$

JPEG-LS [1] is the latest ISO/ITU-T standard for lossless coding of still images. In this scheme, a new predictor, called Median Edge Detection (MED) or LOCO-I (Weinberger *et al.*, 1996) is used to perform the decorrelation of the input data. The operation of MED is outlined as follows:

$$X = \begin{cases} min(P_N, P_W) & if P_{NW} \geq max(P_N, P_W) \\ max(P_N, P_W) & if P_{NW} \leq min(P_N, P_W) \\ P_N + P_W - P_{NW} & otherwise \end{cases} \tag{2.4}$$

The JPEG-based prediction technique is attractive due to its low computational cost, but performs poorly when used to compress complex images. This is due to the fact that JPEG predictors cannot adapt well to suit a particular image context.

---

[1] `http://www.jpeg.org/jpeg/jpegls.html`

2) Context-based adaptive methods

In order to address the problem associated with the JPEG-based prediction technique, Wu & Memon (1997) proposed a context-based adaptive method, which is referred to as the Gradient Adjusted Prediction (GAP). This prediction method can switch to different subpredictors when there is a significant change in the intensity gradient near the current pixel. The 2D version of this prediction scheme begins by estimating the horizontal and vertical intensity gradients for the current pixel. Based on these gradients, the pixels can be classified into one of six contexts: sharp horizontal edge, sharp vertical edge, horizontal edge, vertical edge, weak horizontal edge and weak vertical edge. Decorrelation is then performed using the optimum subpredictor for each context.

In the case of volumetric data, the 3D version of the GAP predictor (Wu & Memon, 2000) first calculates the similarity of adjacent slices in the region of interest. If there is a strong similarity, it uses all of the information from the surrounding areas in the previous slice. Otherwise, if there is a significant change in the intensity gradient between the slices, it switches back to the 2D prediction technique. Although GAP utilises a switch mechanism to adapt itself to the image context changes, this prediction technique requires a longer execution time for both encoding and decoding stages compared to the JPEG-based prediction techniques, as it needs to identify the context of each pixel in the input image data.

In order to speed up the prediction stage, Avramović & Reljin (2010) proposed a simplified version of GAP. They selected only some significant pixels to create a new predictor which they referred to as the Gradient Edge Detection (GED) predictor. Their experiments were conducted on medical images and the results showed that GED was comparable with GAP in terms of decorrelation performance, while maintaining low complexity with regard to prediction.

However, a potential shortcoming associated with this type of prediction technique is that the parameters of the prediction model, such as the switching threshold and the predictor coefficients, are experimentally predefined. As a result, this model cannot adaptively change based on the local statistical characteristics of the data being compressed. This is potentially problematic as the decorrelation performance can be significantly degraded if predefined parameters are not appropriate.

3) Least-square (LS) -based adaptive methods

Recently, a new type of prediction method, LS-based adaptive prediction, has demonstrated impressive improvements over context-based adaptive prediction schemes due to its locally adaptive strategy. Unlike context-based prediction methods that use a predefined model, the LS-based adaptive prediction technique updates the model by locally optimising the prediction coefficients to generate an accurate prediction value. These optimised coefficients are usually calculated by the least mean square principle. This principle is described by Rao & Toutenburg (1999). The detailed process of this principle used for the generation of an optimised prediction model is summarised as follows.

If a prediction model includes N variables, it can be expressed as follows:

$$\hat{p} = \beta_0 + \beta_1 x_1 + \beta_2 x_2 + ... + \beta_N x_N \tag{2.5}$$

where $\hat{p}$ is the predictive value, $x_1, x_2...x_N$ are the prediction variables and $\beta_0, \beta_1...\beta_N$ are the coefficients of the prediction model.

Let $P(x, y)$ denote an actual pixel value at location (x, y) in an image, the prediction error $\varepsilon(x, y)$ is then defined as:

$$\varepsilon(x, y) = \hat{p}(x, y) - P(x, y) \tag{2.6}$$

The prediction error usually has lower entropy than the original pixel value. Therefore, encoding this error, instead of the actual pixel value, leads to more efficient compression in the entropy coding stage. The coefficients $\beta_0, \beta_1...\beta_N$ are determined by minimising the energy of the prediction error based on past predictions as described below

$$minEnergy = min \sum_{x,y \epsilon M} \varepsilon(x,y)^2 \tag{2.7}$$

where M represents past encoded pixels. Solving this equation yields the optimised coefficients. Consequently, β is given by

$$\vec{\beta} = (C^T C)^{-1}(C^T \vec{P}) \tag{2.8}$$

where $\vec{P}$ is an $M \times 1$ column vector containing the previous M encoded pixels as presented below

$$\vec{P} = [P_1, P_2...P_M]^T \tag{2.9}$$

and C is an $M \times N$ matrix consisting of the relevant neighbouring pixels of $\vec{P}$ in the following form

$$C = \begin{bmatrix} x_{11} & x_{12} & ... & x_{1N} \\ \vdots & \vdots & & \vdots \\ x_{M1} & x_{M2} & & x_{MN} \end{bmatrix} \tag{2.10}$$

where x_{ij} is the jth predictor variable of P_i.

It can be seen that calculating the matrix of optimal weights $\beta_0, \beta_1...\beta_N$ using Equation 2.8 for each pixel in the image is extremely computationally intensive, especially for large images. This drawback significantly discourages the use of LS-based prediction methods in practice. Consequently, a number of studies have proposed efficient LS-based compression methods that offer a compromise between computational complexity and coding efficiency.

Seemann *et al.* (1997) proposed a history-based compression algorithm which blended several predictors and applied a penalty in the case of predictors that previously generated poor prediction results. Motta *et al.* (1999) defined a search window around the current pixel and then used a classifier to find a pixel with a context that was similar to the current pixel. The predictor for this pixel was then used to derive the predictor for the current pixel. Ye *et al.* (1999) proposed an acceleration method that turned off the LS optimisation process when the surrounding area was smooth. Since a simple predictor, such as a JPEG predictor, can work well in smooth areas, applying the simple predictor in these regions, instead of LS-based prediction, could significantly reduce computational complexity. Li & Orchard (2001) developed an Edge-Directed Prediction (EDP) technique, based on the same idea, that only recalculated the predictor coefficients at region boundaries. Thus, the predictor could adapt itself from one region to another. Their technique was much more efficient than standard adaptive techniques, as edge areas are usually only found in a small portion of an image. In addition, when LS operations are applied, the calculations are restricted to edge neighbours in order to further reduce the computational cost. Knezovic *et al.* (2006) classified images into several types of regions, such as smooth, noisy, texture regions, and blended different sub-predictors according to the current pixel type.

All of the above LS-based approaches applied LS operations to adaptively update their prediction models during the encoding and decoding stages. However, there is another paradigm for implementing the LS-based prediction approach. This alternative only performs the LS calculation in the encoding stage, abolishing the heavy computation in the decoding stage. In this paradigm, a set of optimal subpredictors is predetermined using the LS method and a switch mechanism is applied to select an appropriate subpredictor based on the context of the current pixel. The coefficients for each of the subpredictors are stored as header information with the compressed data. Based on the header information, future decoding will directly generate the prediction model and completely avoid the complex computations associated with the LS calculation. Kwon *et al.* (1999) and Tiwari & Kumar (2008) applied this paradigm and demonstrated that this asymmetrical prediction technique could provide a high compression ratio with a fast decoding stage, in spite of its higher encoding complexity.

2.2.2 Transform Coding

Transform coding represents another important category of compression techniques in the medical field. This coding procedure involves three major steps: transformation, representation of transformed coefficients and entropy coding as shown in Figure 2.12.

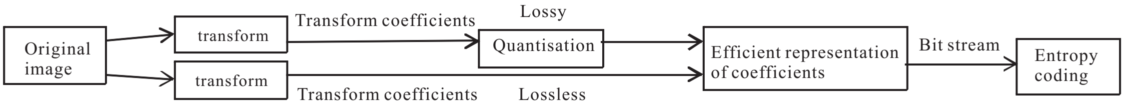

Figure 2.12: A block representation of a general transform coding method.

There are three pixel correlation categories that can be considered for use in compression. These are outlined below:

1. Spatial correlation: the likeness between adjacent pixels
2. Spectral correlation: the relationship between frequency subbands
3. Temporal correlation: the similarity among consecutive frames (Bhavani & Thanushkodi, 2010)

Unlike predictive coding which exploits the spatial correlation and temporal correlation to facilitate decorrelation, transform coding groups spectrally correlated pixels to reduce spectral redundancy. It transforms image data from the spatial domain into the spectral domain and tends to compact most of the energy of an image into the low-frequency components, while separating the high-frequency components such as edges and noise into clustered highpass components. After such a transformation, an effective coding strategy is used to encode this transformed data.

From a previous review of medical image compression techniques (Wong *et al.*, 1995), it is clear that transform-based compression was mainly used for lossy image compression in the medical domain. However, motivated by its excellent compression performance and by consideration for accurate diagnosis, a number of lossless transform coding techniques have been published in the field of medical image compression (Roos *et al.*, 1988; Bilgin *et al.*, 1998; Xiong *et al.*, 1998; Kim & Pearlman, 1999). Among those studies, most research has focused on the use of the wavelet transform in the transformation stage. This technique uses a finite-length or fast-decaying oscillation waveform to represent a signal. In order to match the input signal, the oscillation waveform will be translated or scaled and this translation or scale information is stored as wavelet coefficients. Due to the superior performance of the wavelet transform over other types of transform in terms of decorrelation ability and localisation properties in both the time and frequency domains, the wavelet transform has been employed in the JPEG 2000 compression method.

After applying the wavelet transform, the coefficients can be encoded using Embedded Zerotree Wavelet (EZW) based coding (Shapiro, 1993) and the Set Partitioning in Hierarchical Trees (SPIHT) algorithm (Said & Pearlman, 1996). Both exploit the parent-child relationships between the wavelet coefficients in different subbands of the same orientation to generate an efficient coding strategy. In the case of Zerotree, the basic hypothesis is that, if a wavelet coefficient c at a coarse scale is insignificant with respect to a given threshold T, i.e. $|c| < T$, then all its descendants are likely to be insignificant with respect to T. The descendants refer to all coefficients corresponding to the same spatial location at finer scales of similar orientation. When the above hypothesis is true, a large number of insignificant descendants associated with the same insignificant parent node do not need to be encoded and hence this algorithm can perform efficient data compression. However, there are still many tree structures where the root is significant but other nodes are not. In these cases, EZW is not an efficient representation for insignificant coefficients.

In order to address this problem, Said & Pearlman (1996) proposed a new coding strategy called SPIHT. The main steps of this algorithm are partial ordering by magnitude of the transformed coefficients, set partitioning into hierarchical trees, and ordered bit plane transmission of the refinement bits. One of the essential differences between EZW and SPIHT is in their set partitioning strategies. SPIHT introduces several sets of coordinates to represent small structures as illustrated in Figure 2.13, where $T(i,j)$ contains coefficient $X(i,j)$ and all descendants of $X(i,j)$, $D(i,j)$ is the set of coordinates of all descendants of $X(i,j)$, $O(i,j)$ is the set of coordinates of four direct children of $X(i,j)$ and $L(i,j)$ is the set of coordinates of all descendants of $X(i,j)$ but excludes direct children.

Based on the set definitions of the SPIHT algorithm in Figure 2.13, a descendant is further split into four single-element sets within $O(i,j)$ and a grand-descendant set $L(i,j)$. If the $L(i,j)$ set is significant, a recursive algorithm is applied to partition $L(i,j)$ into four sets $D(i,j)$. SPIHT uses this recursive algorithm to partition $T(i,j)$ until it locates all significant coefficients. EZW does not include this partitioning strategy and usually provides an inferior performance

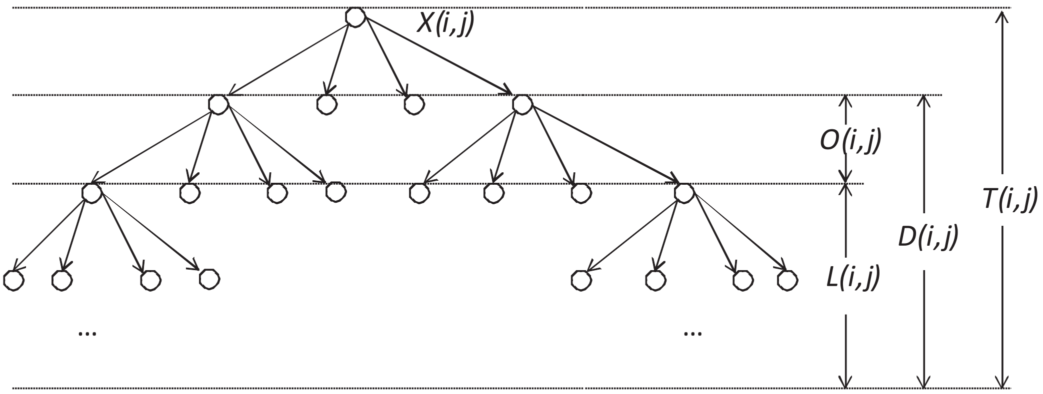

Figure 2.13: An illustration of the set definition in SPIHT.

when compared to SPIHT.

In addition to the EZW and SPIHT algorithms, several other techniques also attempt to efficiently encode wavelet coefficients, such as Cube Splitting (Schelkens *et al.*, 2000), Quad Tree Limited (Munteanu *et al.*, 1999), and Embedded Block Coding with Optimal Truncation (Taubman, 2000). Since they are not popular coding strategies in the field of medical image compression, there will be no further discussions of these strategies in this thesis.

The initial study dealing with wavelet transformation in the field of lossless medical image compression was conducted by Bilgin *et al.* (1998). In this study, they applied a 3D integer wavelet transform with EZW coding to exploit correlations which potentially exist in three dimensions. Additionally, they also introduced a context model for arithmetic coding in order to achieve a better coding performance. Their experimental results showed that this method achieved a higher lossless compression ratio than the other 2D lossless alternatives available at that time. In order to improve the efficiency of the coding strategy, Xiong *et al.* (1998) proposed a 3D SPIHT technique to encode the wavelet coefficients and obtained slightly better compression results than previous techniques (e.g. Bilgin *et al.* (1998)). Kim & Pearlman (1999) later implemented the method proposed by Xiong *et al.* (1998) with different 3D integer transform filters and smaller coding units and applied it to medical image data. Their study indicated that the use of an optimal filter, even with a smaller coding unit, could achieve the same level of performance as previous compression methods. Thus, this study improved the performance of transform coding by reducing memory usage. In order to improve coding speed, Kofidis *et al.* (1999) developed a RLE-based entropy coder to encode the final bit stream in a simple and effective way. More recently, Cho *et al.* (2004) improved the SPIHT algorithm for medical image compression by revising the search sequences. Their improvement was motivated by the fact that tree-based coding could be more efficient by making the tree as long as possible so that it uses less symbols to represent a large number of zero coefficients. General 3D SPIHT algorithms have a limitation in that the image size and the number of slices are usually inconsistent which may limit the decomposition process. The asymmetric tree structure proposed by Cho *et al.* (2004) was intended to solve this problem and has the ability to provide much higher compression ratios when the transaxial and axial dimensions are different.

2.2.3 Pyramid Coding

Pyramid coding is a multi-resolution compression technique that drew some attention in the early stages of medical image compression. It represents an image as a hierarchical structure in scale (resolution) space. The original image is defined as the highest resolution version at the bottom of the pyramid (see Figure 2.14). Decomposition iteratively subsamples pixels to generate lower resolution versions of the original image up to a predefined level. This technique uses the decomposition procedure to reduce statistical redundancy and then encodes the residuals using Huffman, Lempel-Ziv, or arithmetic coding, thus allowing progressive image transmission and reconstruction. Roos *et al.* (1988) conducted a comparison of the pyramid-based coding technique with the predictive coding and transform coding techniques available at that time. Their results show that implementation by hierarchical interpolation (HINT) could give the best decorrelation results on medical images. Based on this study, Roos & Viergever (1993) later extended HINT for use with 3D medical images. They observed that the 3D HINT technique was capable of achieving a higher compression ratio than the 2D version when the data set has a smaller slice thickness than the intraslice resolution. This is due to the fact that the smaller slice thickness indicates a higher correlation between adjacent slices. Therefore, the 3D prediction method outperforms the 2D version in this situation. On the other hand, for the images that have a large slice thickness, they suggested that it would be better to choose the 2D version of the technique for the sake of coding efficiency.

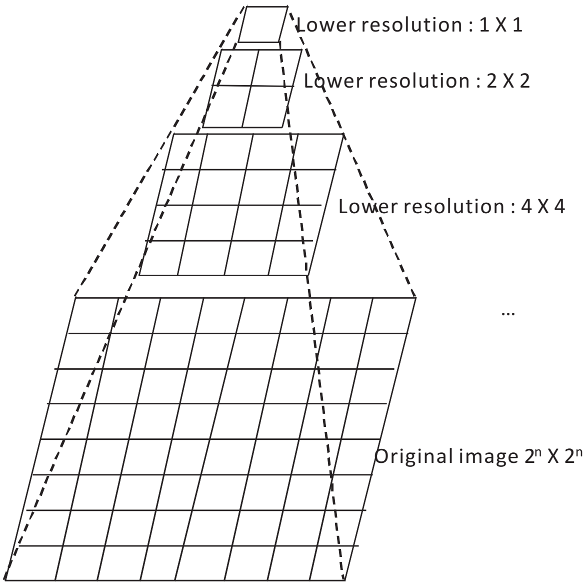

Figure 2.14: A four-level pyramid decomposition.

2.2.4 Multiplicative Autoregressive Models

Multiplicative autoregressive (MAR) models were also used in early compression techniques in the field of medical imaging. This technique initially divides the original image into several smaller blocks. A linear stochastic model is used to predict the image data within each block. The residuals and model coefficients for each block are coded using entropy coding. This method was first used for medical image compression in a study by Das & Burgett (1993). Their results indicated that this technique was capable of providing higher compression ratios than HINT and DPCM coding. Based on this result, they continued to improve this method in terms of efficiency. Due to the fact that the information associated with the blockwise model coefficients always takes up a significant amount of the compressed file, Das & Lin (1996) proposed a hierarchical multiplicative autoregressive (HMAR) model to reduce the size of the side information. HMAR applied a multi-layered modelling approach that generated multiple layers and attempted to model the AR coefficients of the current layer in the subsequent layer using a new AR model. Applying this recursive approach could significantly reduce the model coefficients. Their experimental result showed that this HMAR compression method significantly outperformed the DPCM and HINT techniques. Chen *et al.* (1999) improved the conventional MAR method by adding the JPEG-based prediction stage before applying the MAR predictor. This improved version of MAR has the ability to achieve higher compression ratios than conventional MAR algorithms. However, all of these coding algorithms suffer from high computational complexity.

2.2.5 Hybrid Techniques

Recent research in medical image compression has yielded some hybrid techniques which take advantage of the combination of different coding algorithms. These hybrid techniques improve compression performance when compared with standard approaches. This section describes five representative hybrid techniques in the field of medical image compression.

Segmentation-based lossless image coding (SLIC) The SLIC method, which is based on a simple but efficient region growing procedure, was proposed by Shen & Rangayyan (1997). In this algorithm, the first step involves region growing, followed by JBIG coding to encode the segmentation result. The third step is adaptive arithmetic coding which allows a significant reduction in the statistical redundancy of residual data. Shen and Rangayyan demonstrated that the SLIC algorithm could achieve a high level of compression when tested on a variety of medical images.

Context Adaptive Lossless Image Compression (CALIC) CALIC is a lossless image compression technique (Wu & Memon, 1997). Its core idea is to emphasise modelling by utilisation of a large number of contexts for both adaptive prediction and entropy coding. As previously described in Section 2.2.1, its predictor, GAP, has six contexts and each context has a corresponding optimised subpredictor. Based on the pixel context, the predictor can switch between these subpredictors. When dealing with prediction error, CALIC estimates the conditional expectation of the prediction errors using the error means within the context instead of calculating error conditional probabilities. Its superior performance for medical image compression has been proven by Denecker *et al.* (1997), Kivijärvi *et al.* (1998), and Clunie (2000).

Revision of scanning sequences Another study, conducted by Liang *et al.* (2008), introduced the Hilbert space-filling technique into medical image compression. Their experimental results show that the Hilbert space-filling curve ordering has the ability to enhance the locality of the differences in the residual image. Therefore, a higher compression ratio could be achieved by a later entropy coding stage.

Combination of transform coding and predictive coding Recently, some studies which combined prediction methods with transform coding have improved the level of compression when used on medical images. Chen & Tseng (2007) proposed a combination of the wavelet transform and the LS-based adaptive prediction for medical data compression. Their approach began by choosing a proper wavelet basis function to decompose the image into different bands and then constructing an adequate predictor to reduce the redundancy between parent-child wavelet coefficients in LH, HL and HH subbands respectively. The illustration of these subbands is shown in Figure 2.15. Adaptive arithmetic coding was then used to code the prediction errors. When generating subband predictors, they used the F test to select important predictor variables and Minimum Mean Square Error (MMSE) estimation was used to determine coefficients of the predictor. Ramesh & Shanmugam (2010) applied the same idea as described above except a different method was utilised for predictor variable selection. They used a graphic method which plotted the results generated by different combinations of variables and then selected the value with the best match to the original input.

Zhao *et al.* (2009) applied the steps of prediction and transformation in the opposite order to that in the papers described above. They initially applied a prediction method, followed by integer wavelet transformation. Their results showed that the use of the wavelet transformation has the ability to further reduce the entropy of the decorrelated data.

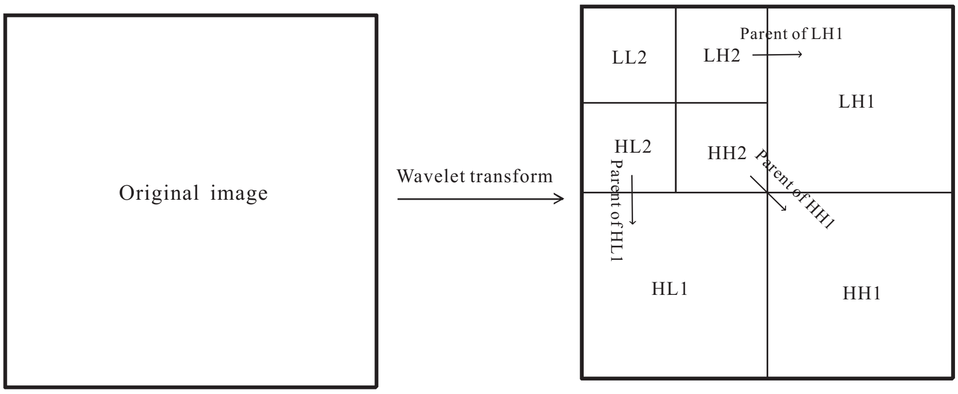

Figure 2.15: The wavelet transform representation of an image.

Combination of JPEG-LS and video coding As previously described, JPEG-LS is a lossless compression standard for 2D images. In order to deal with 3D medical images, Miaou *et al.* (2009) suggested that integrating the technique used in video compression into medical image compression could reduce temporal (interframe) redundancy. When they combined motion estimation and motion compensation (MEMC) with JPEG-LS, the overall compression ratio was significantly higher than that achieved by performing JPEG-LS directly. Clearly, this achievement can be primarily attributed to the high similarity between adjacent slices in volumetric medical image data sets.

Ramkumar & Raglend (2012) also applied this hybrid compression strategy to medical images. However, in order to reduce the coding time, they firstly estimated the similarity between the two adjacent slices. If the estimated similarity value was higher than a predefined threshold, they used MEMC technique to reduce redundancy between slices. Otherwise, only JPEG-LS was applied to compress the image data.

2.2.6 Anatomy-based Compression

In addition to the above general compression methods used for medical image compression, a more noteworthy study was conducted by Sanchez *et al.* (2009). As described in their paper, a human skeleton is left-right symmetric and they took advantage of this feature to develop a symmetry-based compression technique. Their technique began by applying the wavelet transform to the entire data set. The wavelet coefficients for one half of the data set were then subtracted from the coefficients for the other half, leaving residual data with very low entropy. Subsequently, a modified version of the embedded block coder was used for the entropy coding stage. They concluded that their technique significantly outperformed standard image compression methods, such as JPEG 2000 2D and 3D.

2.2.7 Discussion

In this section several state-of-the-art algorithms for medical image compression are discussed and characterised. Some techniques, such as JPEG-LS prediction and the wavelet transform, have been published officially in the JPEG standard due to their efficiency and speed. Other cited compression techniques are not included in the compression standards. The compression performance of these approaches when used on medical image data, such as CT images, MR images, mammography studies and chest X-ray, is summarised in Tables 2.3 and 2.4.

It should be noted that some methods reviewed in the previous sections are not included in Tables 2.3 and 2.4 due to the fact that pixel depth information is not provided or the fact that entropy coding was not applied to the decorrelated data. In addition, it should also be noted that actual clinical data is usually stored using 12 bits per pixel, however, some studies quantised the data to 8 bits. The techniques presented in those studies are summarised in Table 2.3. These

Table 2.3: Previous compression results tested on 8-bit medical images.

Author(s)	Method	Results (bit per pixel)				Results yielded by standard technique (bit per pixel)			
		CT	MR	Mammo	Chest Xray	JPEG-LS		JPEG 2000	
						CT	MR	CT	MR
Das & Lin (1996)	HMAR		2.25						
Shen & Rangayyan (1997)	SLIC			1.75					
Wu & Memon (1997)	CALIC	3.63	5.73		5.83				
Bilgin *et al.* (1998)	3D CB-EZW	1.50	2.12			1.83	2.75		
Xiong *et al.* (1998)	3D SPIHT	1.99	2.00			2.85	2.93		
Chen *et al.* (1999)	APMAR	2.86	4.81		4.45				
Bilgin *et al.* (2000)	3D CB-EZW	1.36	2.01			1.83	2.75		
Xiong *et al.* (2003)	3D ESCOT	1.27	1.79			1.83	2.75		
Cho *et al.* (2004)	AT-SPIHT	1.36				1.83		2.04	
Ait-Aoudia *et al.* (2006)	DPCM+PPMd	1.37	2.06						
Knezovic *et al.* (2006)	LS	2.00	4.77			1.98	4.71	2.23	4.76
Chen & Tseng (2007)	Wavelet + adaptive prediction	1.42	2.7					1.63	2.91
Liang *et al.* (2008)	DPCM+Hilbert+LZW+Huffman	2.35				> 2.35			
Miaou *et al.* (2009)	JPEG-LS+video coding		1.65				2.93		3.08
Zhao *et al.* (2009)	DPCM+IWT+Huffman	2.01			3.74				

Table 2.4: Previous compression results tested on 12-bit medical images.

Author(s)	Method	Results (bit per pixel)			Results yielded by standard technique (bit per pixel)					
		CT	MR	Medical images	JPEG-LS			JPEG2000		
					CT	MR	Medical images	CT	MR	Medical images
Roos & Viergever (1993)	3D HINT	6.49	8.61							
Seemann *et al.* (1997)	History-based compression			4.34			4.55			
Sanchez *et al.* (2009)	Anatomy-based	3.17	3.32					3.74	3.81	
Avramović (2011)	GED	4.37			4.32					

techniques were originally designed for natural image compression and this type of image typically has bit depths of 8 bits per pixel or 8 bits per colour plane. However, medical images have a larger pixel depth, generally 12 bits per pixel, and application of general compression techniques requires a quantisation process which essentially sacrifices diagnostic information to shrink the intensity range. In this case, the techniques should be classified as lossy compression techniques due to the quantisation process. The subsequent discussion focuses solely on the lossless compression techniques due to their relevance to the material discussed in this thesis.

It is clear from Table 2.4 that the previously documented compression techniques are usually compared with standard image compression methods, such as JPEG-LS or JPEG 2000, in order to evaluate their efficiency. Most of the techniques reviewed in the table are examples of natural image compression techniques applied to medical data and only reduce spatial, temporal and spectral redundancies in the compression process. As can be seen in the table, these techniques only provide small improvements over standard compression. For example, the improvements obtained by history-based compression and GED are 5% and 1%, respectively. However, in the case of medical images, there is an additional redundancy that could be exploited to improve compression. This redundancy can be expressed as anatomical redundancy. It does not exist either between the current pixel and its neighbours or between the high-frequency components and the low-frequency components. It is derived from the anatomical features, e.g. bilateral symmetry in the human body. Sanchez *et al.* (2009) incorporated this anatomical feature into their compression technique. They only stored one half of the data and the other half was the residual information subtracted from the stored data. This process further reduced the left-right redundancy of the source data. As can be seen in Table 2.4, this anatomy-based compression technique has achieved a significant improvement over standard compression (JPEG 2000) in terms of compression ratio with an average improvement of 15%. However, with the exception of this study, no other attempt has been made to exploit the inherent characteristics of medical images in order to improve the level of compression achievable.

The study by Sanchez *et al.* (2009) confirms that medical characteristics can be utilised to improve the level of compression achievable on medical images. However, their technique is restricted to situations where there is a very high level of symmetry, such as MRI scans of the head, and it is not applicable in situations where the level of symmetry is low, e.g. abdominal CT studies. This specific problem is addressed in Chapters 4, 5, and 6, which present a new anatomy-based compression scheme for use with abdominal CT data sets. The proposed method exploits the similarity of anatomical structure among different patients to improve the level of compression. More importantly, it is applicable in the case of asymmetrical data.

2.3 Conclusion

From the literature review detailed in this chapter, it can be concluded that considering the inherent characteristics of medical image data is the key to achieving both fast volume rendering and high compression ratios. Although several attempts have been made towards the development of specific algorithms for medical image compression and volume rendering for CTC, some limitations still exist in these approaches. Firstly, in the field of volume rendering, most previous methods designed for CTC rely on particular hardware to accelerate rendering speed. However, in the remote access CTC scenario, none of the previous methods can be applied as it is unlikely that the necessary hardware will be available on the client machine. Therefore, there is a clear need to develop a new volume rendering technique which can provide real-time performance on low-cost PC platforms. Secondly, with regard to improving the level of compression achievable in the case of medical images, Sanchez *et al.* (2009) demonstrated a promising research direction which utilised anatomical information to improve the compression result. However, their method is specifically designed for use in the situation where there is a high degree of symmetry in medical image data. It is not feasible to extend their method to compress CTC data sets due to the lack of symmetry in the abdomen. In this case, it is desirable to create a new compression solution for CTC data sets.

Thus, the main objectives of this thesis are to develop a novel medical image compression method that is capable of achieving a high compression ratio on CTC data sets and a real-time volume rendering technique that is capable of operating on low-cost PC platforms. The details of these techniques are presented in the following chapters.

Chapter 3

Software-based Real-time Volume Rendering

Volume rendering plays an important role in polyp detection. It can provide clear 3D images to help the radiologist to detect polyps that might be hidden around sharp bends and within deep folds of the colon wall. Primary 3D CTC for polyp detection increases the sensitivity for median sized polyps by 44% (Pickhardt *et al.*, 2007) and decreases the interpretation time by 30% (Kim *et al.*, 2007b). Thus, this functionality can greatly help radiologists to make a timely and accurate diagnostic decision. According to a recent survey (Hara *et al.*, 2011), 50% of radiologists prefer a primary 3D approach or combined 2D and 3D when performing CTC examinations.

Unfortunately most current volume rendering techniques depend heavily on particular hardware to accelerate the rendering speed. This chapter presents a fast software-based alternative to these techniques which is designed specifically for use with CTC data and capable of running on a low-cost PC platform. This technique is an optimised ray casting approach which utilises a novel subvolume-based method to accelerate the rendering speed in the case of CTC data. To further improve rendering efficiency, general acceleration methods, such as constant forward step and optimised trilinear interpolation, are also included in the technique. A number of experimental results are presented in this chapter in order to provide a qualitative and quantitative evaluation of the proposed technique.

3.1 Overview of the Proposed Volume Rendering Technique

CTC is a field in which rendered image quality is paramount. Therefore, most volume rendering techniques in this area are based on the ray casting algorithm due to its ability to generate high-quality images. In this thesis, this algorithm is used as the basis for the proposed volume rendering technique.

As discussed in Chapter 2, there are three requirements when applying volume rendering techniques to CTC. These are perspective projection, user interaction and an acceptable frame rate. A number of the previous techniques (Wan *et al.*, 1999, 2000; Li *et al.*, 2001) have achieved these requirements. However, they all suffer from a heavy dependence on hardware acceleration and hence cannot be ported to a remote PC platform. Since the research reported in this thesis deals with a remote distributed scenario, it is necessary to have a high level of hardware independence. As a result, only software-based acceleration methods can be applied to increase the rendering speed. Therefore, in addition to the three requirements mentioned above, the technique described in this chapter should also be a purely software-based approach.

The proposed volume rendering technique attempts to meet all the requirements and its operation is illustrated in Figure 3.1. The original data set is first processed to generate a series of finite differences. A new 3D interpolation operator utilises these computation results to decrease the complexity associated with interpolation of sample points along each ray. A region of interest is interactively selected by the user which defines a subvolume. The perspective volume rendering is subsequently applied in this subvolume and the rendering process is accelerated by several methods, such as constant forward step, empty space skipping, fast 3D interpolation and early ray termination. Details of these acceleration methods are provided in the next section. In addition, this technique supports a high level of user interaction with the 3D model. Operations, such as rotation and translation of viewpoint, enable a thorough examination of the colonic wall.

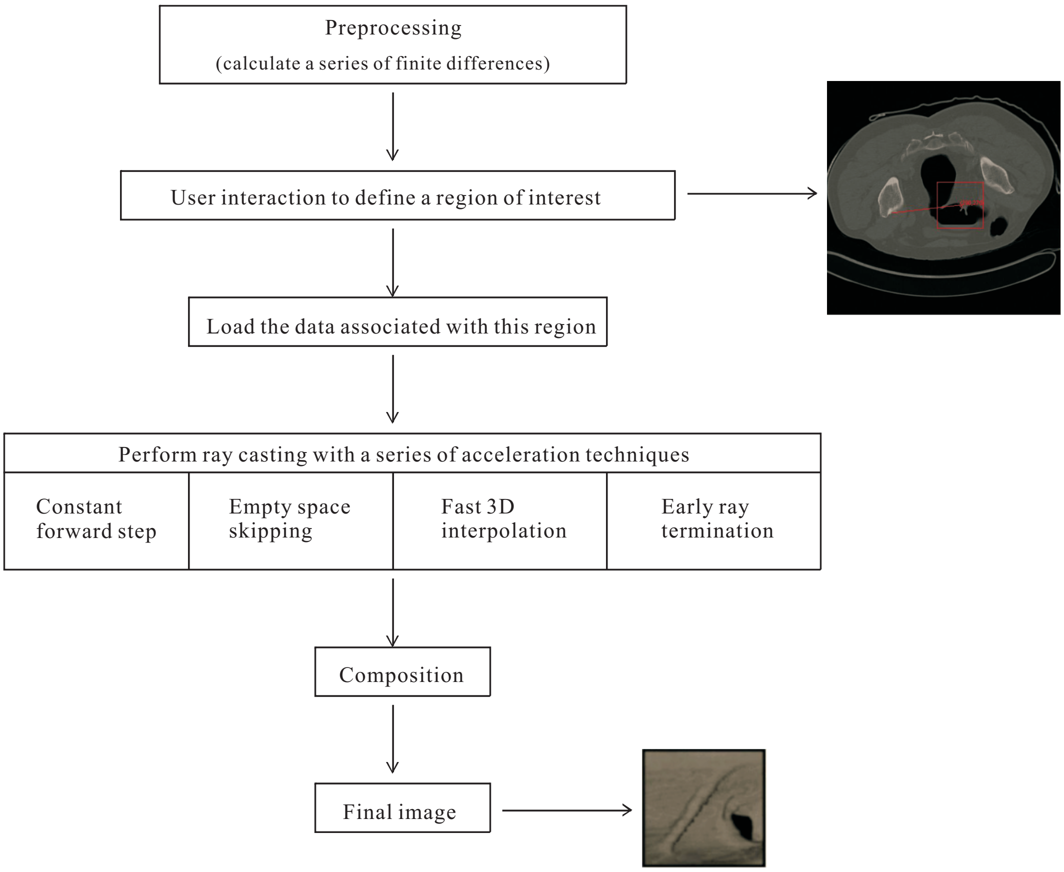

Figure 3.1: A flowchart of the proposed volume rendering technique.

3.2 Acceleration Methods

There are three acceleration methods that have been developed to accelerate volume rendering. These are rendering with subvolume, constant ray step and optimised trilinear interpolation.

3.2.1 Rendering with Subvolume

Recently, with the increasing size of volumetric medical data sets, it has become even harder to render the whole data set in real-time. A distinct feature of CTC applications is that the camera is always located inside the colon, and hence a large part of the data set falls outside of the field of view and will not need to be rendered. Consequently, during the implementation of CTC navigation, the volume rendering technique only needs to process a small portion of the data and focuses on a region of interest to accelerate the rendering speed.

The region of interest can be selected in such a way that the user clicks on the image to locate the initial viewpoint and a subvolume centred at this viewpoint is generated. Volume rendering is then applied in this subvolume. The subvolume can be moved in 3D space with the arrow and plus/minus keys. This operation is illustrated in Figure 3.2. The up and down arrow keys control the movement of the subvolume along the z-axis, the left and right arrow keys control the movement of the subvolume along the x-axis, and the plus and minus keys control the movement of the subvolume along the y-axis. Additionally, the user can interact with the viewpoint and perform operations, such as rotation and translation, using a combination of Ctrl with the arrow and plus/minus keys. This technique provides a full field of view within the colon. The user can examine the whole colonic wall by rotating the viewpoint and controlling the subvolume movement. Although this method shrinks the region of volume rendering, it will not affect the ability to make a diagnosis as the whole data set can still be rendered step by step.

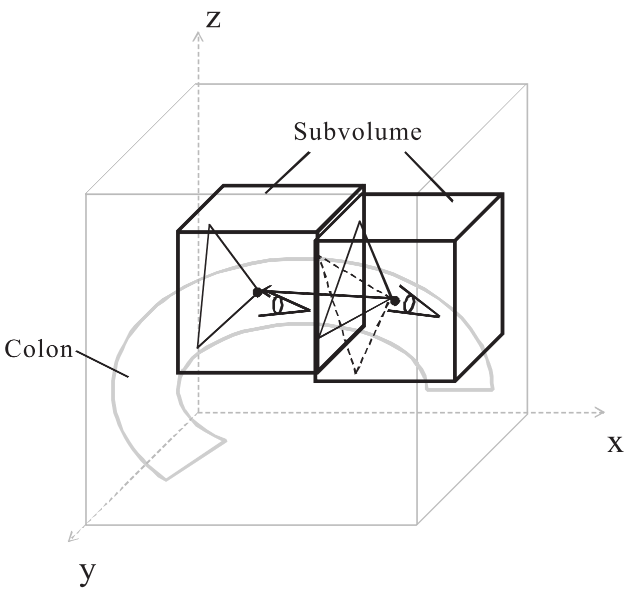

Figure 3.2: Navigation within the colon using the subvolume technique.

3.2.2 Constant Ray Step

General ray casting algorithms calculate the sample point location, and then use the eight neighbouring voxels to perform trilinear interpolation. In order to obtain the sample point location, the ray step sizes in the x, y, and z directions should be calculated. In Figure 3.3, the ray step size along the x-axis is:

$$step.x = l * cos\alpha / cos\beta \tag{3.1}$$

where l is the length of the ray step, α is the angle between the ray and xy plane and β is the angle between the ray projection on the xy plane and x' axis. It is clear that if the ray is increased by the same length in each step i.e. l is a constant value, the ray step size ($step.x$) is a constant value along the same ray.

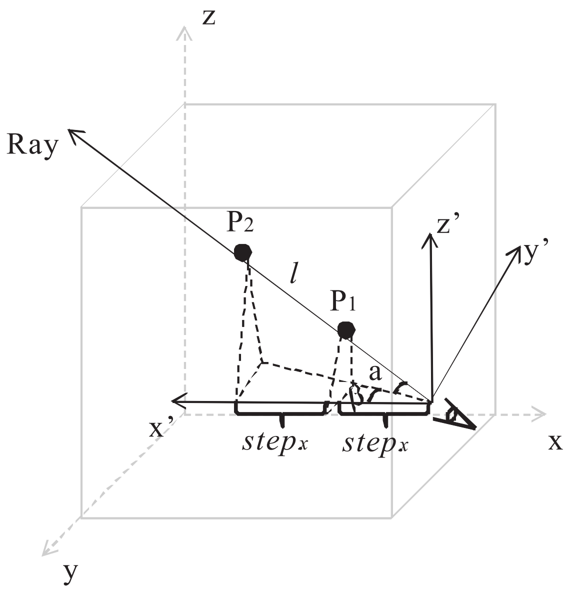

Figure 3.3: Determining ray step length in the x direction.

The ray step sizes along the *y* and *z* axes can be defined in a similar way. Therefore, when sampling along each ray, the coordinate of the sample point is calculated by simply adding the step sizes along the *x, y*, and *z* axes to the previous point, instead of carrying out complicated geometric calculations.

Since moving the viewpoint forward or backward does not change the angles, the calculations for ray step sizes along the *x, y*, and *z* axes only need to be performed once. However, when the viewpoint is rotated, this technique needs to recalculate the ray step sizes along each axis.

3.2.3 Optimised Trilinear Interpolation

Once the sample point has been located, the next step is to estimate the sample value at an arbitrary 3D location which requires the use of trilinear interpolation. The formula for trilinear interpolation is derived from Lagrange interpolation. This interpolation method constructs an interpolation polynomial based on a series of given points to yield the interpolated value at a new point. This process is described by Jeffreys & Jeffreys (1988). Given a set of *n+1* known samples $f(x_k)$, *k=0,1,2,...n*, the Lagrange interpolation polynomial can be expressed as:

$$y(x) = \sum_{k=0}^{n} l_k(x) f(x_k) \tag{3.2}$$

where

$$l_k(x) = \prod_{i=1,k\neq i}^{n} \frac{x - x_i}{x_k - x_i} = \frac{(x - x_0)}{(x_k - x_0)} ... \frac{(x - x_{k-1})(x - x_{k+1})}{(x_k - x_{k-1})(x_k - x_{k+1})} ... \frac{(x - x_n)}{(x_k - x_n)} \tag{3.3}$$

When *n=1*, it means that there are only two known points. These points can be denoted as *k* and *k+1*. The $l_k(x)$ and $l_{k+1}(x)$ are:

$$l_k(x) = \frac{x - x_{k+1}}{x_k - x_{k+1}} \tag{3.4}$$

$$l_{k+1}(x) = \frac{x - x_k}{x_{k+1} - x_k} \tag{3.5}$$

Therefore, the first-order Lagrange polynomial interpolation can be described in the following form:

$$y(x) = \frac{x - x_{k+1}}{x_k - x_{k+1}} y_k + \frac{x - x_k}{x_{k+1} - x_k} y_{k+1} = y_k + \frac{y_{k+1} - y_k}{x_{k+1} - x_k}(x - x_k) \tag{3.6}$$

In this first-order case, the Lagrange polynomial interpolation reduces to linear form. Trilinear interpolation can then be achieved by extending this one dimensional linear interpolation into three dimensions. The standard trilinear interpolation operator is as follows:

$$\begin{aligned} V_p = & V_0(1-\Delta x)(1-\Delta y)(1-\Delta z) + V_1(1-\Delta x)\Delta y(1-\Delta z) + V_2(1-\Delta x)(1-\Delta y)\Delta z \\ & + V_3(1-\Delta x)\Delta y\Delta z + V_4\Delta x(1-\Delta y)(1-\Delta z) + V_5\Delta x\Delta y(1-\Delta z) \\ & + V_6\Delta x(1-\Delta y)\Delta z + V_7\Delta x\Delta y\Delta z \end{aligned} \tag{3.7}$$

where $\Delta x, \Delta y$, and Δz are fractional offsets of the sample position along x, y, and z axes. The associated 3D structure is illustrated in Figure 3.4. From Equation 3.7, it is clear that a total of 24 multiplications and 19 additions are necessary to compute the interpolated value. Consequently, trilinear interpolation is a time-consuming operation in ray casting.

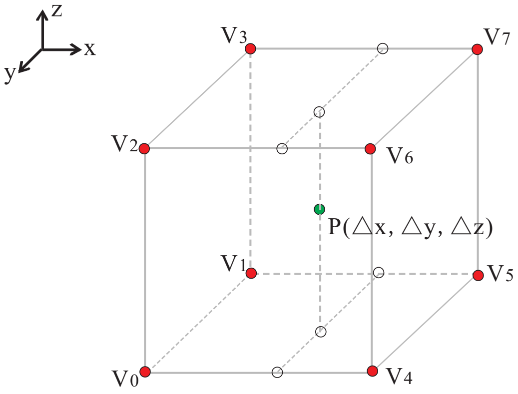

Figure 3.4: The trilinear interpolation process. The red dots show the known voxels and the green dot is the point to be interpolated.

In order to reduce the computational complexity, a previous study (Zhuge *et al.*, 2003) employed a series of finite differences to create a high performance trilinear interpolation operator:

$$\begin{aligned} V_p =& \Delta x \Delta y \Delta z \Delta V_{75} + \Delta x (1-\Delta y) \Delta z \Delta V_{64} + \Delta x \Delta y \Delta V_{54} + \Delta x \Delta V_{40} \\ & + (1-\Delta x) \Delta y \Delta z \Delta V_{31} + (1-\Delta x)(1-\Delta y) \Delta z \Delta V_{31} \\ & + (1-\Delta x)(1-\Delta y) \Delta z \Delta V_{20} + (1-\Delta x) \Delta y \Delta V_{10} + V_0 \end{aligned} \tag{3.8}$$

where the differences are defined as follows:

$$\begin{aligned} & \Delta V_{75} = V_7 - V_5; \Delta V_{64} = V_6 - V_4; \Delta V_{54} = V_5 - V_4; \Delta V_{40} = V_4 - V_0; \\ & \Delta V_{31} = V_3 - V_1; \Delta V_{20} = V_2 - V_0; \Delta V_{10} = V_1 - V_0; \end{aligned}$$

All these differences can be obtained in the preprocessing stage. Therefore, the computational complexity is reduced from (19 ADD + 24 MLT) for the standard operator to (12 ADD + 17 MLT) for the approach proposed by Zhuge *et al.* (2003).

However, it is possible to precompute more results so that the computation in the rendering stage will be further reduced. Based on this observation, a new trilinear interpolation technique is proposed in the following form:

$$\begin{aligned} V_p =& \Delta x \Delta y \Delta z (\Delta V_{75} - \Delta V_{64} - \Delta V_{31} + \Delta V_{20}) + \Delta x \Delta z (\Delta V_{64} - \Delta V_{20}) + \Delta x \Delta y (\Delta V_{54} \\ & - \Delta V_{10}) + \Delta y \Delta z (\Delta V_{31} - \Delta V_{20}) + \Delta x \Delta V_{40} + \Delta z \Delta V_{20} + \Delta y \Delta V_{10} + V_0 \end{aligned} \tag{3.9}$$

All of the difference calculations can be implemented in the preprocessing stage. Consequently, the computational complexity is reduced to (7 ADD + 12 MLT). It is worth noting that this method is over twice as fast as the standard trilinear interpolation operator.

In addition, the proposed volume rendering technique also employs empty space skipping and early ray termination approaches to further improve performance.

3.3 Experiments and Results

Two types of experiments are conducted in order to assess the performance of the proposed volume rendering technique. The first set of experiments were carried out in order to identify the execution time for this technique on a low-cost PC platform. The purpose of this investigation was to evaluate the applicability of the developed volume rendering technique in a remote distributed scenario. In order to illustrate the validity of the proposed technique, the second set of experiments compared the results produced by the proposed volume rendering technique with those achieved by advanced visualisation software.

These tests were conducted on a Dell desktop computer equipped with 2.80GHz Intel(R) Pentium 4 CPU and 512M of RAM. All the software was written using the Java programming language. This is motivated by the fact that Java is not only a multi-platform programming language but also an efficient software development technique which can provide comparable performance to C or C++ for equivalent computational tasks (Niemeyer & Knudsen, 2005).

A range of CTC data was used in this thesis. This data was obtained from the Department of Radiology at the Mater Misericordiae University Hospital in Dublin. Thirty-five patient studies were selected without any prior knowledge of the patient. All the patients were scanned in both prone and supine positions. In general, 35 patient studies will generate 35 prone and 35 supine CTC data sets. It should be noted that the data used in this thesis consists of two parts: the first is the CTC data set and the second is the colonoscopy report from the colonoscopy examination. The latter is used as the gold standard to identify polyps in the acquired CTC data set. A total of 40 data sets (24 prone data sets and 16 supine data sets) that had corresponding gold standards were ultimately used to develop and evaluate the techniques outlined in this thesis. The average number of slices per data set was 267 and each slice contained 512 × 512 pixels. Thus, the average data set consisted of approximately 70 million pixels. In general, the slice thickness was 1.5 mm and the pixel size ranged from 0.566 mm to 0.808 mm. A complete description of the data sets is provided in Appendix A.

Five CTC data sets were randomly selected from the database and used in these experiments. The IDs of these data sets are 3, 4, 21, 22 and 40.

3.3.1 Rendering Time

The proposed method uses the subvolume technique to improve rendering speed. Thus, the size of the subvolume significantly affects rendering performance. A smaller subvolume size yields a higher rendering speed. The different subvolume sizes have been applied in this experiment in order to deduce the maximum subvolume size that continues to offer a high performance. This technique in conjunction with subvolume sizes of 100 × 100 × 100, 150 × 150 × 150, 200 × 200 × 200 and 250 × 250 × 250 was tested on five data sets and repeated 100 times respectively. The average performance of the proposed technique for different subvolume sizes is shown in Table 3.1.

Table 3.1: Volume rendering performance using different subvolume sizes.

Subvolume size (voxels)	Image plane size (pixels)	Initial time (second)	Frame rate (frames per second)
100 × 100 × 100	100 × 100	0.563	66.01
150 × 150 × 150	150 × 150	0.875	44.74
200 × 200 × 200	200 × 200	5.015	25.40
250 × 250 × 250	250 × 250	108.500	3.59

The initial time includes the time for file I/O and preprocessing. It is clear from these results that when the subvolume size is below 200 × 200 × 200, the proposed technique can achieve real-time rendering (25 frames per second).

A more noteworthy comparison of the proposed technique with standard methods is presented in Figure 3.5. The traditional sample point calculation method and the standard trilinear interpolation method were tested. It is clear that the proposed approach is significantly faster than other traditional methods due to a lower computational complexity.

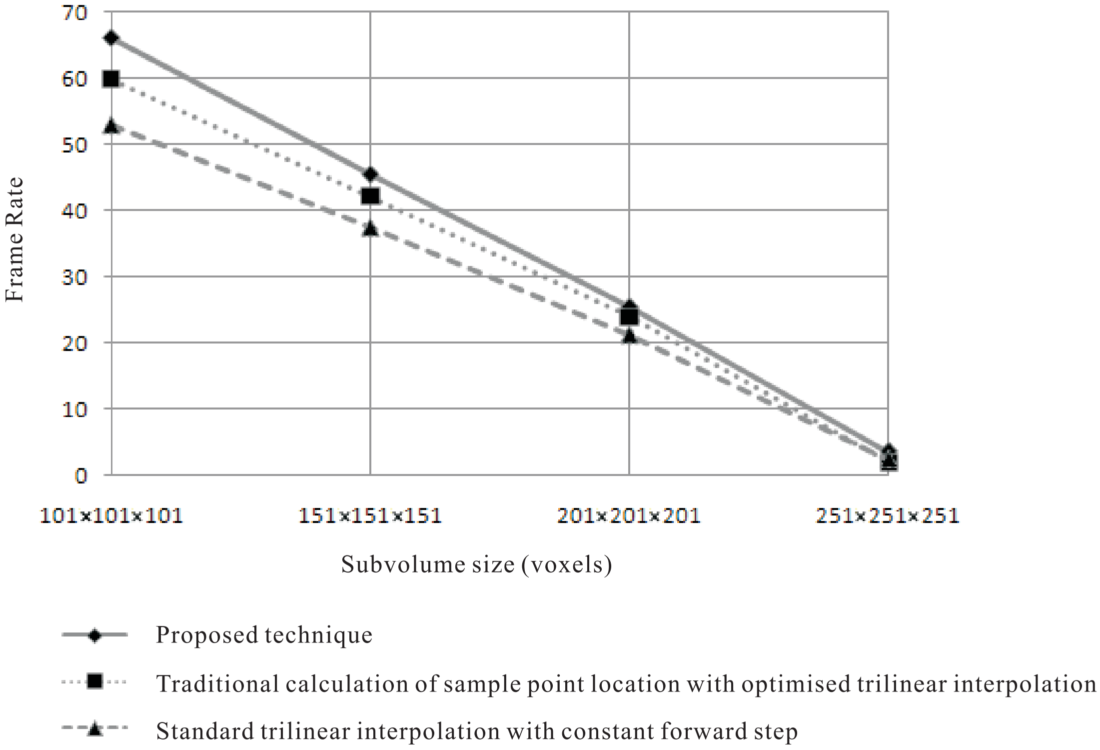

Figure 3.5: Volume rendering performance provided by different techniques in conjunction with a range of different subvolume sizes.

3.3.2 Rendering Quality

In order to illustrate the validity of the proposed technique, the rendering results achieved by this technique have been compared with those obtained using Visualisation Toolkit (VTK). This is an open-source software package developed for 2D/3D image processing, isosurface generation and 3D volumetric visualisation. It has been widely used in the field of medical imaging processing due to its rich set of image processing functions and powerful visualisation capabilities (Wolf *et al.*, 2005; Caban *et al.*, 2007; Wang & Pu, 2009). Therefore, the results achieved by the VTK are used as benchmarks for qualitative evaluation.

In this experiment, the proposed volume rendering method was applied to the five CTC data sets. In each data set, four 101 × 101 × 101 regions were selected and rendered with the proposed technique and with the VTK. The four sets of renderings that were obtained are presented in Figures 3.6 - 3.9.

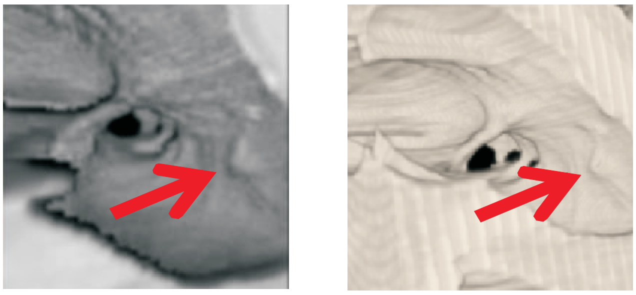

Figure 3.6: Volume rendering using the proposed method and the VTK to display a polyp.

It is difficult to evaluate rendering quality in a quantitative manner due to different shading models, viewing parameters and transfer functions. In CTC images, the detailed structure of the colon wall, the possible abnormalities, and even the tissue beneath the colon surface should be clearly visualised. This can be used as a quality criterion for comparing two rendered images which are produced

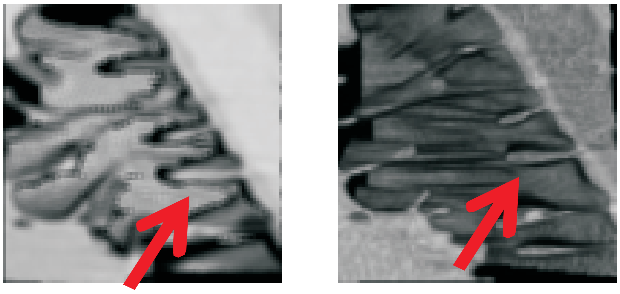

Figure 3.7: Volume rendering using the proposed method and the VTK to display folds in the colon.

Figure 3.8: Volume rendering using the proposed method and the VTK to display colonic wall.

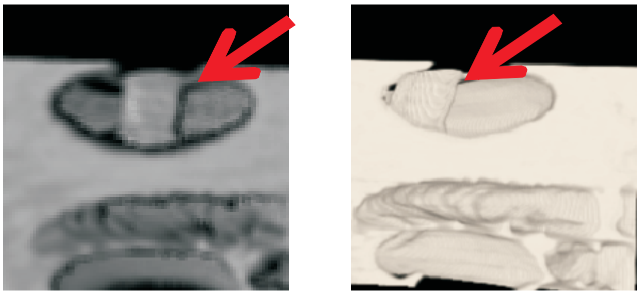

Figure 3.9: Volume rendering using the proposed method and the VTK to display the inflation tube that is used in a CTC examination.

by the proposed method and the VTK respectively. The polyps, folds, colonic wall and inflation tube are important features within a CTC data set. It is clear from Figures 3.6 - 3.9 that the proposed technique can provide representations of these features that comparable with the representations generated by the VTK. Thus, it can be concluded that the proposed method achieves a level of rendering quality that is similar to the VTK. More importantly, the proposed method can be ported to any operating system that supports Java (e.g. mobile devices), whereas the VTK is a software system that depends on a specific platform and is difficult to use in Web-based applications.

3.3.3 Diagnostic Capability

Since CTC is a screening technique to detect colonic abnormalities such as colon polyps, the volume rendering technique used for CTC should have the ability to clearly display these abnormalities. Therefore, a further evaluation of the performance of the proposed technique in terms of its diagnostic capability is carried out. This is achieved by visualising various polyps with different shapes (pedunculated, sessile, or flat) and different diameters using the proposed volume rendering technique. Colonic polyps used in this evaluation were identified by a medical colleague with expertise in the area of CTC. The 3D visualisations of these polyps rendered using the proposed technique are presented in Figures 3.10 and 3.11.

As is evident from these figures, even though some polyps are very small ($<$ 2 mm in diameter), they can still be easily seen in the images generated by the proposed volume rendering technique. Therefore, this technique can be used to help radiologists detect colonic polyps which are of a small size.

In addition, a comparison of this 3D tool and VTK in terms of their ability to detect polyps has been carried out. A database which includes 40 pairs of

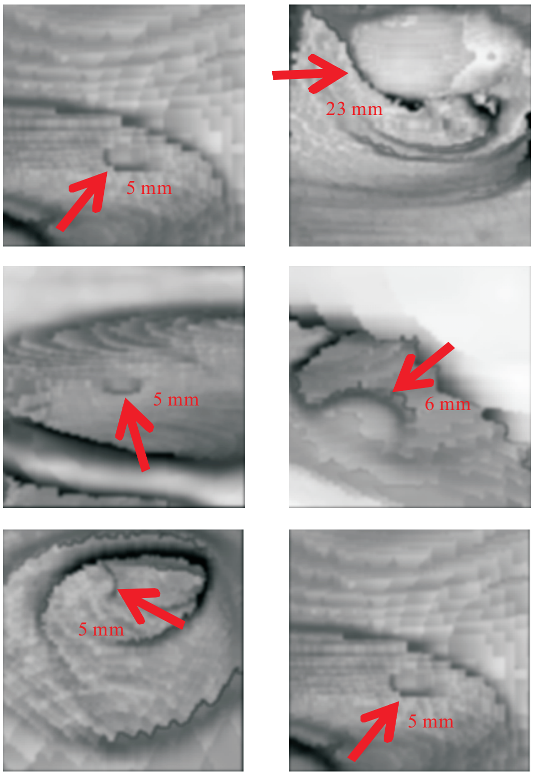

Figure 3.10: Visualisations of polyps with size $\geq 5mm$ using the proposed volume rendering technique.

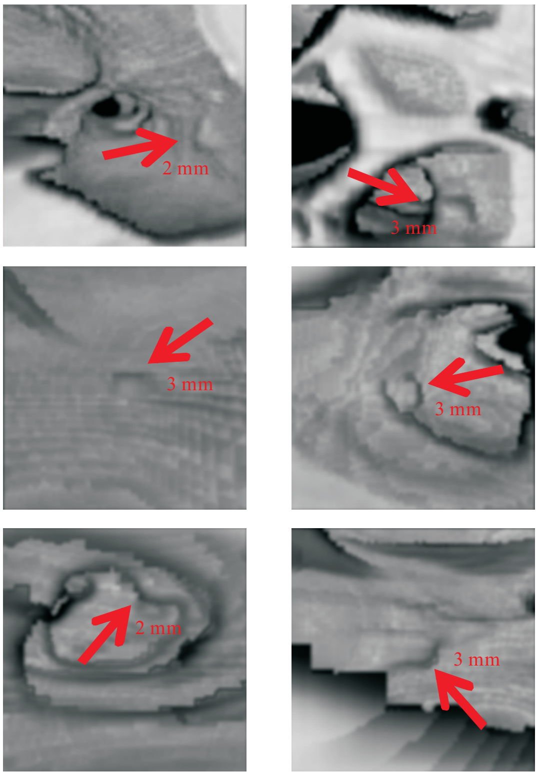

Figure 3.11: Visualisations of small polyps ($< 5mm$) using the proposed volume rendering technique.

3D images generated from CTC data sets, was created for this experiment. The first 40 images were obtained using the VTK and a further 40 corresponding images were created using the proposed method. Each pair of images rendered the selected colon segment using the same view direction. This ensured that the rendered region was the same for both 3D techniques. There were 20 true-positive, 5 potential false-positive and 15 true-negative results in the 40 scenarios. The total of 80 images were stored in two sets and each set had 40 images. The first set contained scenarios 1-40 and the images were generated either using the VTK or the proposed method. The second set contained the counterparts to the images in the first set. Once the image database was created, a CTC expert, blinded to the polyp findings, was asked to identify the polyps from the images. The two sets of images were interpreted over two days, one set each day. The results showed that the sensitivities of the reader were 85% for the VTK images and 80% for the images generated using the proposed method. Although there is a discrepancy in performance between these two techniques, it may result from a small sample size or chance variation. The F-test is used to verify the significance of this difference and the result of this test shows no statistically significant difference between the two sets (alpha=0.05), thus, confirming that the proposed method is comparable to the VTK in terms of polyp detection accuracy.

3.4 Conclusion

Perspective volume rendering can provide clear visualisations of the interior of the human body. However, software-based volume rendering techniques typically suffer from poor performance due to the computationally intensive nature of the volume rendering process. The most straightforward approach for accelerating this process is a trade-off in image quality. However, lower quality renderings can result in serious consequences, such as misdiagnosis. This chapter presented a novel software based volume rendering technique that has solved the performance issue through a series of innovative optimisations. The proposed system can run on a standard PC platform without the need for any specialised graphics hardware. More importantly, the experimental results demonstrate that this level of performance has been achieved without sacrificing the quality of the rendered image.

Chapter 4

An Anatomy-based Segmentation Method for Image Compression

Generally speaking, segmentation is a fundamental operation in the field of image processing that is carried out in order to extract objects in an image for further analysis. In the context of data compression, the purpose of the segmentation process is to split the image into multiple regions characterised by the homogeneity of the image intensity. Different segmented regions may then be compressed separately using a locally optimised method to achieve a high compression ratio. This is motivated by the fact that the encoded image pixel is always correlated with its neighbours. Utilisation of this correlation characteristic can significantly reduce the image entropy so as to yield substantial compression gains. However, the correlation characteristic is not always constant over the whole image. A global compression model for all pixels would result in a suboptimal compression result for at least some areas of the image. Therefore, the compression technique proposed in this thesis uses a segmentation process to generate a 'divide and conquer' approach to deal with medical image data sets.

The advantage of segmentation in relation to medical images is that the general contents of the image are known beforehand. Therefore, it is preferable to use prior knowledge to tailor a general segmentation method to the specific application. The objective of this chapter is to combine a traditional intensity-based segmentation algorithm with anatomical knowledge to develop a segmentation method that is used as a preprocessing stage for the compression technique.

4.1 Overview of the Proposed Compression Scheme

The compression scheme proposed in this thesis is based on predictive coding. Predictive coding is chosen for its simplicity and efficiency. As mentioned in Section 2.2.1, one of the key challenges associated with predictive coding is to generate an accurate prediction model. Current prediction methods have been designed for use with general images and have achieved a high level of performance when tested on this type of image. Medical images have distinctive characteristics which differ from general images, e.g. weak edges due to a phenomenon known as the *Partial Volume Effect* (PVE). This effect occurs in medical imaging because of the limited resolution of the imaging systems. These systems try to average several densities on the boundaries between different regions. As a result, the pixels on the boundaries have an average value of all of the surrounding pixels and hence cause some 'blurring' over the boundary areas (see Figure 4.1). Thus, general prediction methods are not suitable for direct application to medical image compression. Furthermore, it is also taken into consideration that medical image data has some inherent characteristics, i.e. bilateral anatomical symmetry and similarity of anatomical structure across different patients. Exploitation of these characteristics provides an unparalleled opportunity to improve the level of compression achievable on medical images. There is no doubt that a compression algorithm tailored for medical images leads to improved performance when compared with the performance of general purpose algorithms that are designed for natural image compression.

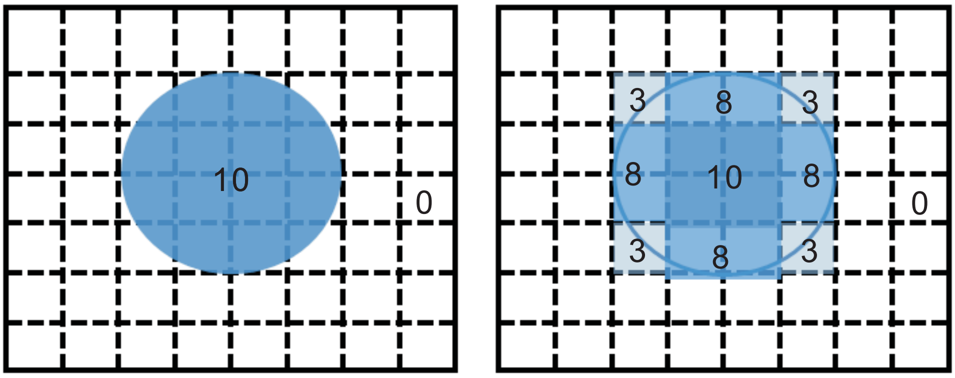

Figure 4.1: Influence of image sampling on the PVE. The actual object is displayed in the left image and the right image is processed by sampling. In the right image, pixels on the edges of the object are associated with both the object and the surrounding tissues. The densities of these pixels are the mean of the underlying regions.

In this thesis, an anatomy-directed, locally optimised prediction technique, called Anatomy-based Adaptive Prediction (AAP), is proposed. The combination of AAP and an entropy coder creates the complete compression scheme, which is referred to as Anatomy-based Lossless Medical Image Compression (ALMIC). This compression scheme utilises the anatomical characteristics of the patient to prelocate different anatomical regions within a medical data set. An AAP model that contains a series of predictors, which are optimised for each specific anatomical region, is then applied to produce a predicted value. The final prediction errors achieved by subtracting the predicted value from the actual value are then sent for entropy coding.

In this study, the validity of the developed compression scheme is demonstrated using CTC data sets. A schematic description of the complete compression scheme for CTC data is illustrated in Figure 4.2 and the main steps of the scheme are briefly outlined below.

A) Segmentation

a) The segmentation process begins by extracting the whole body from the CTC data set and recording its outline using a series of chain codes (one chain code for each slice in the data set). The automatic segmentation of the whole body is described by Kim *et al.* (2011). Once the entire body has been extracted, it is preferable to store the outline information rather than the whole body region in order to save space. The body outline is obtained using the Roberts edge detector (Roberts, 1965) and represented using a 4-connected chain code. When encoding the body outline, a point on the boundary is selected and its coordinates are stored. The encoder then follows the boundary in a sequential manner and keeps track of the directions from one boundary pixel to the next. A symbol that represents the direction of the movement is stored using a chain code. In order to further reduce the size of the outline file, the chain code is compressed using a lossless coding technique.

b) The next step in the segmentation process is to identify the four regions outside the scan area, i.e. the regions in the four corners of the image with a constant density of -1024 Hounsfield Units (HU) (see Figure 4.3). This can be achieved using seeded region growing, initiated from the four corner points. These regions can then be stored in a very efficient manner by simply recording a parametric representation of the circular boundary between the regions and the actual scan data.

c) Once the entire body and the regions outside the scan area have been extracted, the remaining pixels in the image can then be assigned to one of the predefined categories (e.g. air, soft tissue and bone) based on their location and density features. Details of each pixel category can be found in Sections 4.3 and 4.4.

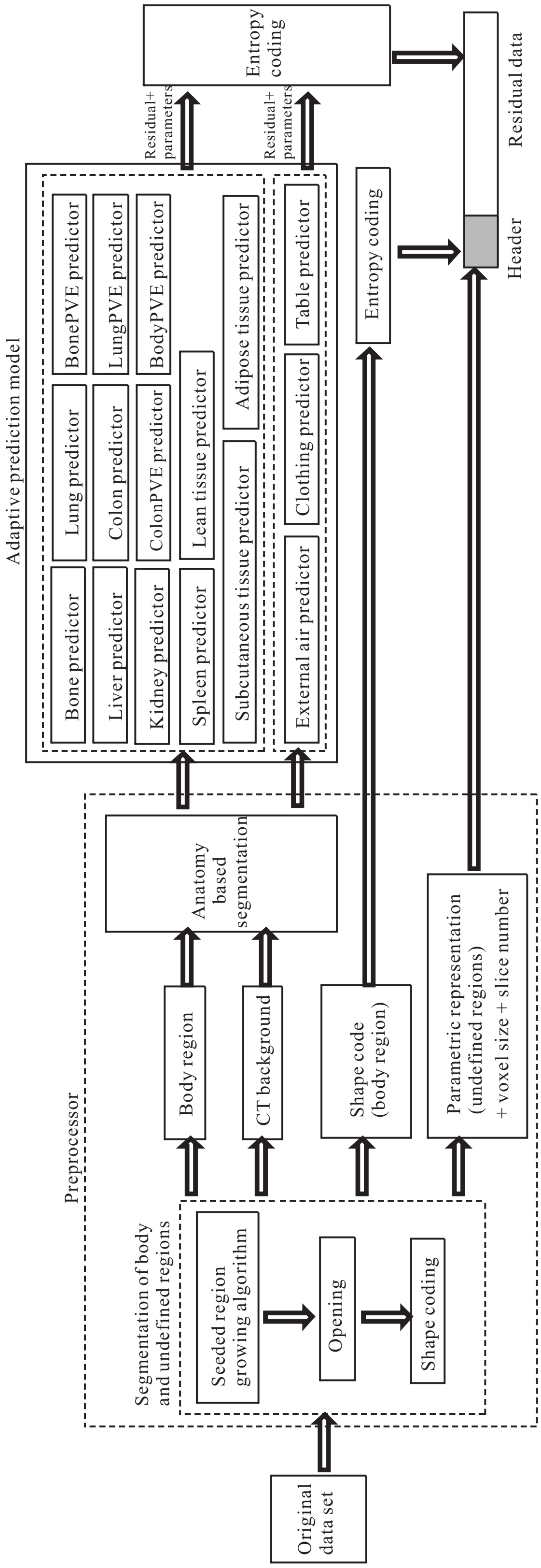

Figure 4.2: A block diagram of the proposed compression scheme (ALMIC).

]

B) Adaptive prediction model

Based on the segmentation results in step A, a series of predictors, optimised for each specific anatomical region, are subsequently generated. An adaptive prediction model that consists of these optimised predictors is then applied to the whole data set. The formulation of this adaptive prediction model is described in Chapter 5.

C) Entropy coding

After decorrelation using the adaptive prediction model, the contour code, predictor parameters and residual data are sent to an entropy encoder. An efficient entropy coding technique is identified in Chapter 6. The final compressed file contains two parts, the header and the main body. The header of this file contains the contour code, the predictor parameters, the voxel size, the number of slices and the parametric representation of the circular boundary (from Step A (b)); and the body of the file contains the residual data.

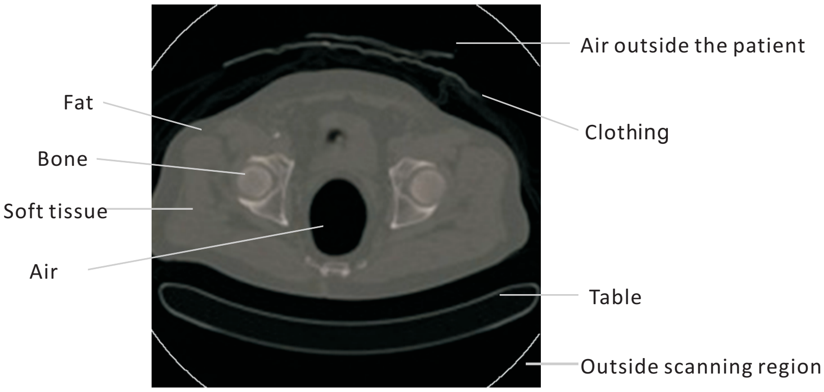

Figure 4.3: An illustration of the main regions typically found in a CT data set.

4.2 Anatomical Terms

In order to avoid terminology-based confusion, this section details some of the important anatomical terms that appear in this chapter. These terms are related to the description of body parts and their relative positions.

4.2.1 Anatomical Terms for Tissues

Soft tissue: refers to tissues that connect, support, or surround other structures and organs of the body.

Adipose tissue: or fatty tissue is used for storing energy. Depending on its location this tissue has different names: visceral fat is located within the abdominal wall (i.e. beneath the wall of the abdominal muscle) whereas subcutaneous fat is located beneath the skin (and includes fat that is located in the abdominal area beneath the skin but above the abdominal muscle wall).

Lean tissue: usually refers to muscle.

4.2.2 Anatomical Terms for Describing Positions

Superficial: refers to a location closer to the body surface (e.g. the skin is superficial to the muscle).

Deep: is the opposite of superficial i.e. far from the surface.

Inferior: refers to a direction away from the head or toward the lower part of the body (e.g. the heart is inferior to the head).

Bilaterally symmetrical: means the left and right structures appear to be identical.

4.3 Categorisation of Different Anatomical Regions

A typical CTC data set contains a vast amount of detailed information representing organs e.g. the colon, the kidneys and the liver. However, it is possible to describe the actual patient data using just four categories, i.e. soft tissue, fat, bone and internal air.

In addition to the voxel categories that are mentioned above, there is a special category for CT images, called the PVE voxels. PVE voxels can be seen as subvoxels that contain a mixture of two or more surrounding regions. The tissue-air and tissue-bone transition areas have a large number of PVE voxels.

Furthermore, a radiology image also contains objects that are outside the patient's body, e.g. the scanning table and the patient's clothes (see Figure 4.3); hence, there are two additional regions defined for these objects. Also, as can be seen in Figure 4.3, CT images contain a significant amount of background information which is represented by black pixels. The majority of this information corresponds to regions inside the scanning area, while the areas in the four corners are outside the detector ring. The former is filled with air which has a low density value typically around -1000 HU while the latter, outside the ring, can be seen as an undefined region and has a constant density value, specifically -1024 HU.

With the inclusion of these additional regions, the CTC data set can be subdivided into nine main categories. These categories are bone, soft tissue, internal air, PVE regions, adipose tissue, table, clothing, air outside the patient, and undefined regions. Soft tissue, internal air, PVE regions and adipose tissue are classified into subgroups according to their anatomical positions. All the categories used in the segmentation process are shown in Table 4.1. The density and anatomical features for each category are explained in the next section.

Table 4.1: The properties of the main regions typically found in a CTC data set.

	Category		**Density range**
Inside the body	bone		≥+1000 HU
	soft tissue	liver	≥50 HU & ≤250 HU
		kidney	≥30 HU & ≤250 HU
		spleen	≥40 HU & ≤240 HU
		lean tissue	≥-30 HU & ≤150 HU
	air	lung	≤-700 HU
		colon	≤-900 HU
	PVE regions	colon PVE	≥-30 HU
		bone PVE	≥250 HU
		lung PVE	≥-30 HU
		body PVE	around -400 HU
	adipose tissue	Subcutaneous	≥-190 HU & ≤-30 HU
		visceral, intermuscular, bone marrow	remaining regions inside the body (≥-190 HU & ≤-30 HU)
Outside the body	table		>-800 HU
	clothing		>-800 HU
	undefined region		==-1024 HU
	air outside the patient		remaining regions outside the body (≤-800 HU)

4.4 Analysis of the Features for Each Category

Two features are used to guide the segmentation process: density features and anatomical features.

4.4.1 Density Features

The CT scanning system has standard HU values for each type of tissues (e.g. fat and bone). The attenuation of water is defined as 0 HU and the attenuation of air is defined as -1000 HU. The HU value of soft tissue in the CTC data set is in the range of -200 HU to 200 HU, while bone has a much higher density value (above 700 HU) (Gunderman, 2006). Although CT data sets may be generated by different scanners for patients, there is a small variation in HU values for each type of tissue due to the fact that all CT scanners are calibrated to the x-ray attenuation of water (Deglint *et al.*, 2007). Therefore, it is reasonable to assume that the HU value for each type of tissue in a CT data set is applicable for all CT scanners. Motivated by this fact, density-based segmentation approaches are widely used to extract a region of interest in medical images.

Histogram thresholding is an example of a density-based image segmentation approaches. It analyses the histogram of an image, finds the valley points between consecutive major peaks and then uses the intensity values that corresponds to the valley points as thresholds to segment the image into different regions. Figure 4.4 presents a sample histogram of a CTC data set. It can be concluded from this histogram that the ranges that should be employed to segment internal air, adipose tissue, soft tissue and bone using the thresholding technique are $\leq$ -900 HU, -200 HU $\rightarrow$ -30 HU, -30 HU $\rightarrow$ 250 HU and $\geq$ +1000 HU respectively. It should be noted that after analysing 20 CTC histograms, the HU distributions were found to be nearly the same and the thresholds for each region were in line with the values listed above, thus confirming the generalisability of these thresholds. Air which resides in both the lungs and colon takes up a large part of the body. However, the density of the air in each of these regions is different. The density in the lungs is ≤ -700 HU and the density in the colon is ≤ -900 HU. Furthermore, although the organs within the body are essentially composed of soft tissues, their density ranges are slightly different, e.g. the liver is in the range of 50 HU → 250 HU (Alomari *et al.*, 2008), the kidney is in the range of 30 HU → 250 HU (Zagoria, 2004), and the spleen is in the range of 40 HU → 240 HU (Rabushka *et al.*, 1994).

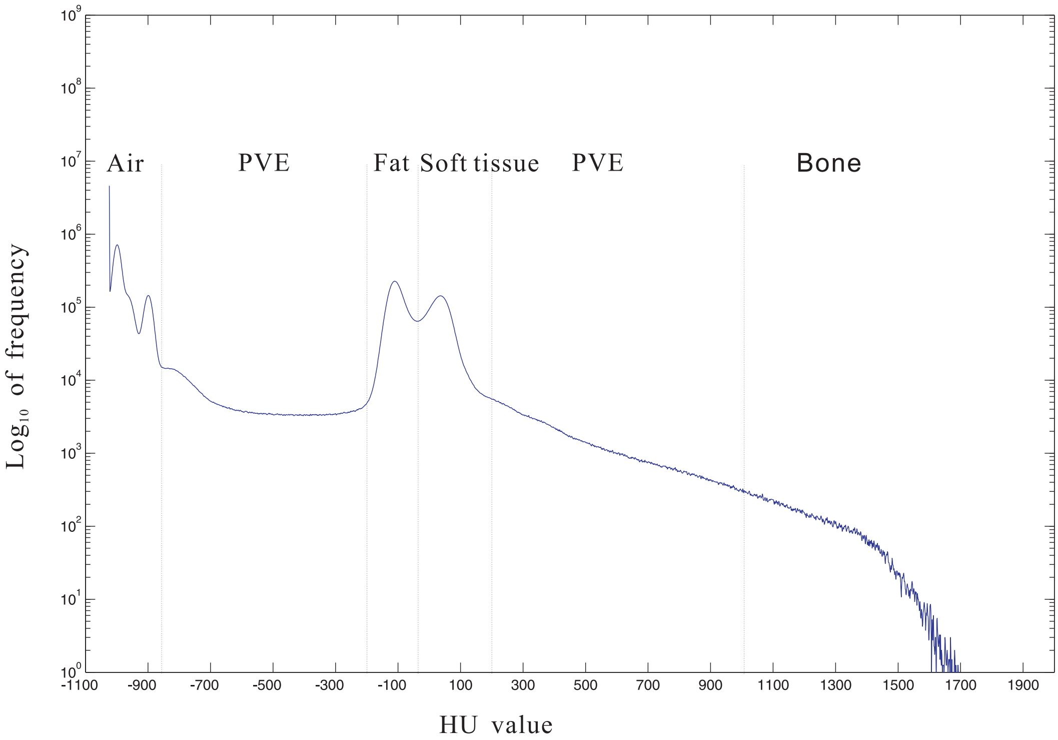

Figure 4.4: A global histogram of a sample CTC data set.

The PVE voxels, which can be seen as bone-tissue or tissue-air transitions, have a density which is the average of that in the surrounding regions. In the case of bone-tissue transition, the density of the PVE voxels in this region is certainly lower than the lowest density of bone and higher than the highest density of soft tissue. Therefore, bone PVE voxels are in the range 250 HU → 1000 HU. PVE voxels around the colon and the lungs are defined in a similar way. Therefore, if the value of a voxel belongs to the PVE density range, and if the distance between the voxel and previous air or bone area is less than or equal to 3 voxels (the approximate width of the PVE region (Wang *et al.*, 2008)), then the voxel is defined as a PVE voxel. PVE voxels around the outside of the body can be easily identified as the body outline is already recorded in the previous segmentation step. The use of erosion and dilation operations on the body area can determine the body PVE region.

Regarding the categories outside the body, the thresholds for the clothing and the table are both greater than -800 HU, otherwise the voxel belongs to external air. The voxels outside the scan area have a constant value of -1024 HU.

4.4.2 Anatomical Features

The density-based segmentation method is sufficient for the recognition of air, soft tissue and bone regions. However, it is difficult to distinguish between specific organs, such as the lungs and the colon, based solely on density features due to the fact that both organs contain air. In addition, the liver and surrounding muscles also have nearly the same density range which means the histogram thresholding method does not work properly for segmenting these objects either.

In order to identify specific organs, it is reasonable to exploit the anatomical position to define candidate regions. A density-based segmentation is then applied in these regions to avoid incorrect segmentation. Figure 4.5 presents approximate anatomical information for each organ that is typically found in an abdominal

CT data set. This figure indicates prior knowledge of organs such as their relative position in the body and their approximate shape. The following parts of this section discuss how to use this anatomical information to automatically detect specific organs in an abdominal CT data set. The other regions, such as bone, clothing, and external air, can be directly extracted using the density-based segmentation technique. Segmentation of these regions is not further discussed in this section.

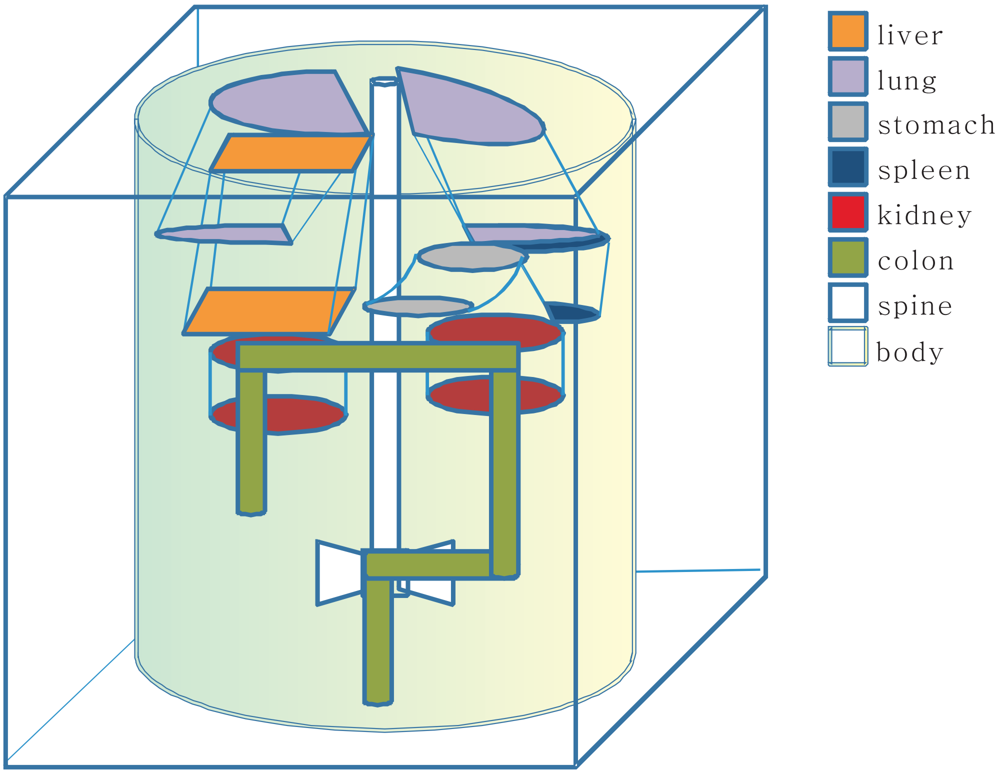

Figure 4.5: A model of the anatomical structure in an abdominal CT data set.

Subcutaneous tissue

Subcutaneous tissue is located beneath the skin (see Figure 4.6). The outline of the body is identified in the body segmentation stage. Thus, it is feasible to erode the body outline to determine the location of the subcutaneous tissue region. Regarding the number of erosion steps, Gibney *et al.* (2010) state that normal skin thickness is 2.2 mm and that the normal thickness of the subcutaneous adipose tissue layer is 13.9 mm. Therefore, the total number of erosion steps can be calculated as:

$$steps = (thickness\_skin + thickness\_subcutaneous\_tissue)/pixel\_dimension \tag{4.1}$$

If a pixel's dimensions in a slice are 0.76 × 0.76 mm (width×height), the total number of erosion steps is 18 in order to extract skin and subcutaneous tissue.

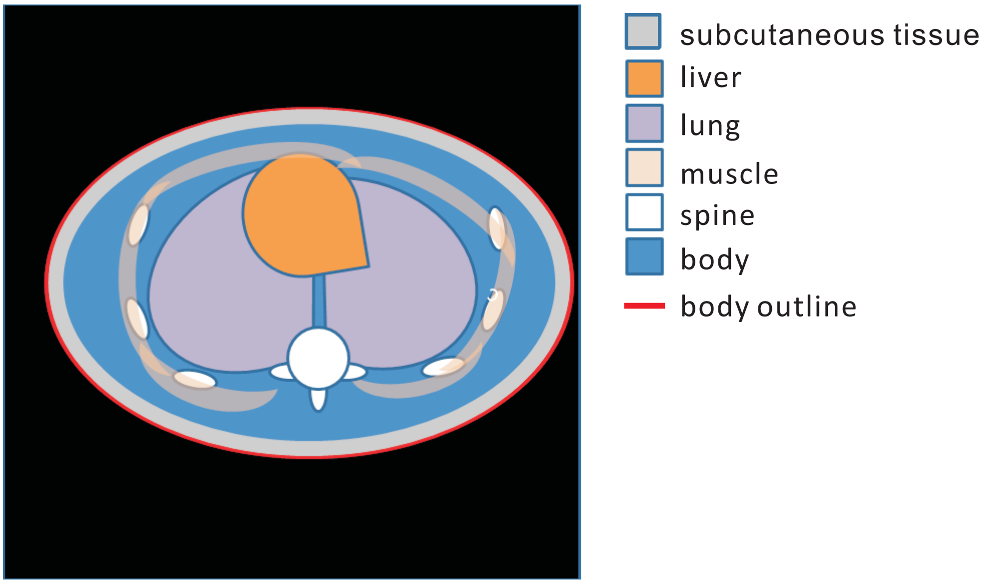

Figure 4.6: An illustration of the identification process for the subcutaneous tissue region. The candidate subcutaneous tissue region is indicated by grey colour.

Lung

In the case of lung segmentation, there is difficulty in discriminating between the lung voxels and the colon voxels. This is due to the fact that both the lung and the colon are filled with air and hence have nearly the same density characteristics. However, their anatomical positions are significantly different. The lungs are always situated in the upper part of the body, while the colon is located in the middle, lower section, beneath the lungs. Since an abdominal CT data set is acquired from the bottom of the lungs, if the air voxels exist in the top slice of the data set, they definitely belong to the lungs rather than the colon (see Figure 4.7). Consequently, it is sufficient to use the simple thresholding technique to extract the lungs in the top slice. Based on this initial segmentation result, the segmentation of the lung can be achieved using a simple top-down segmentation approach. In this approach, if an air voxel in the current slice is connected to the segmented lung region in the previous slice, it belongs to the lungs, otherwise it belongs to the colon. It is possible to take advantage of anatomical structures to distinguish the lung from the colon.

Liver

Another organ which is also present at the top of the abdominal CT data is the liver. However, the liver may not be easily segmented as it has nearly the same density as the surrounding tissue, e.g. soft tissue and muscle. Additionally, the muscles of the lower chest wall and upper abdomen overlay the liver which makes accurate segmentation of the liver more difficult. If the thresholding method is directly applied to extract this region, the result of the segmentation usually contains a lot of muscle and soft tissue regions which are not part of the liver.

This problem has been addressed by Wang *et al.* (2009). They make use of the relative location of the liver with respect to the ribs to remove the muscle around the liver. It can be seen from Figure 4.8 that the muscle is primarily situated around the ribs. The ribs have high density values and can be readily extracted. Thus, they can provide sufficient information to locate the muscle and distinguish it from the liver.

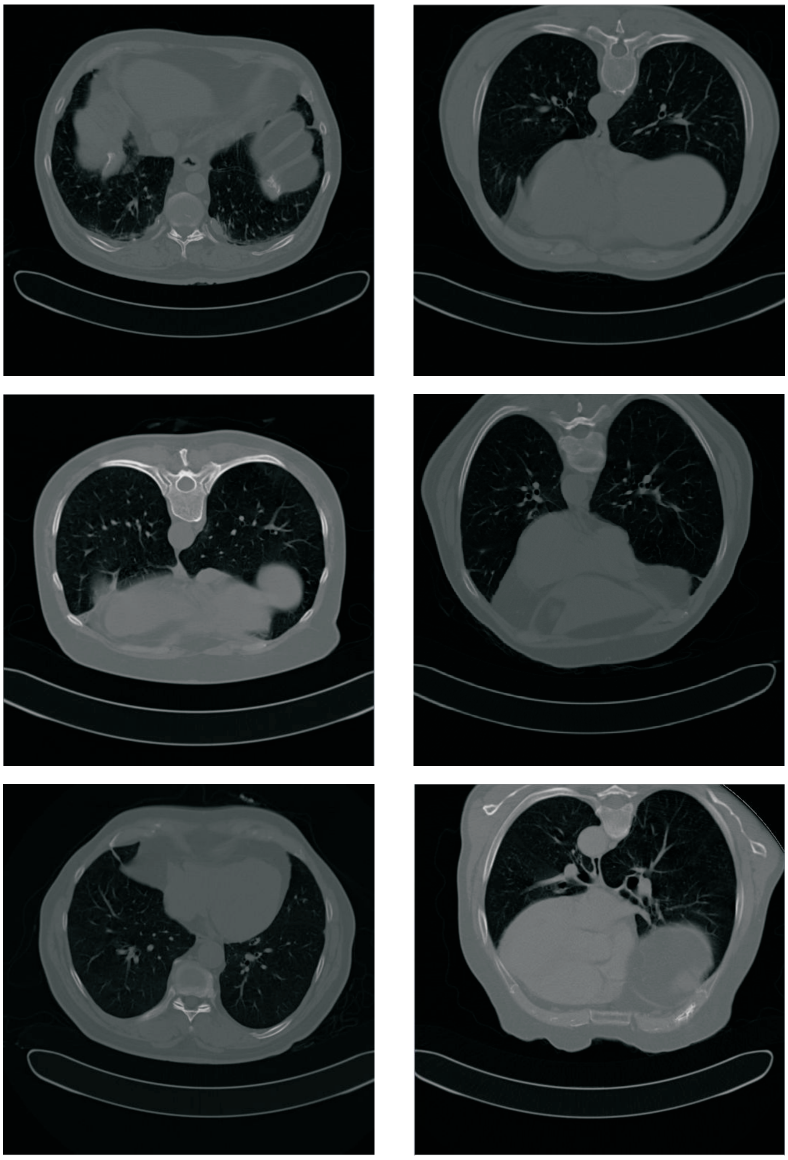

Figure 4.7: The top slices of six abdominal CT data sets.

In this thesis, liver detection also uses anatomical information and exploits the fact that the liver is deep to the muscle. Muscles and ribs are superficial to the lungs and liver. Once the lungs have been identified, it is possible to shrink the body outline to achieve an approximate region representing the abdominal cavity which excludes the ribs and most of the muscle regions. This process is presented in Figure 4.8. The red solid line depicts the body outline and the red dotted line indicates the abdominal cavity region. This cavity region contains three pixel categories: bone, soft tissue and air in the lungs. Due to the differences in density among these categories, the thresholding technique can be used to remove the bone and the lung pixels inside the dotted line region.

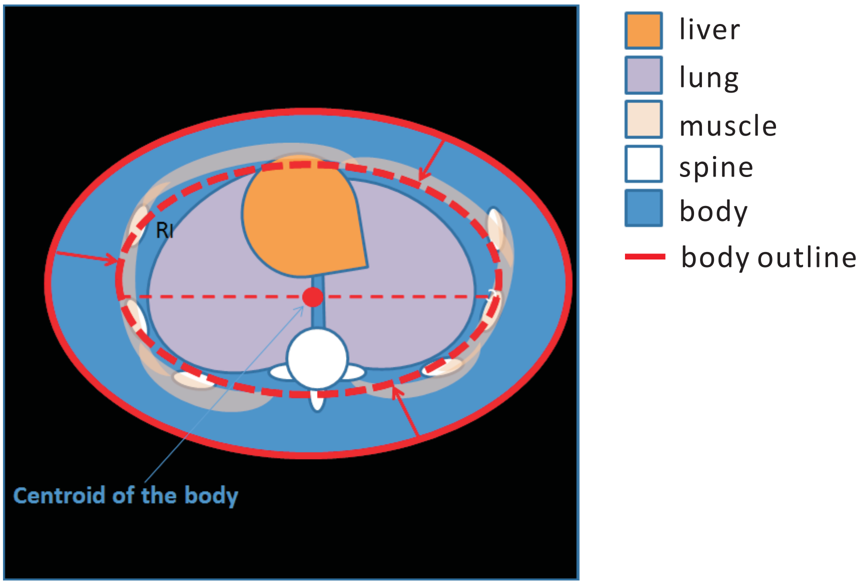

Figure 4.8: An illustration of the liver region identification process. The candidate liver region (R_l) is indicated within the red dashed semi-ellipse.

However, there are still some soft tissue regions that remain within the dotted line, i.e. bone marrow. This region has nearly the same density as the liver and hence can not be directly removed using the density-based segmentation method. A potential solution to this problem is the utilisation of the liver location in the body to remove the remaining areas. The liver is always situated in the front section of the body, whereas the soft tissue in the spine is present towards the back of the patient. The centroid of the body can serve as a dividing line between the top and the bottom parts within the body. Therefore, it is possible to obtain an approximate location of the liver by using the centroid of the body. Using the above approach, segmentation of the liver can be achieved by applying both anatomical and density based rules.

Kidney

The kidneys are two small organs located on each side of the spine, just underneath the ribcage. These location features can be used to define the vertical and horizontal positions of the kidneys in an abdominal CT data set. In the top-down sequence, the top of the kidneys can be identified by tracking the ribs. After a certain point when the location of the current slice in a CTC data set is below the lowest rib, the kidney is apparent.

Once the top of one kidney is identified, the next step is to locate the two kidneys in subsequent slices. Lin *et al.* (2006) calculated the relative distance of the kidney regions to the spine and used this information to extract the candidate kidney regions. This process is illustrated in Figure 4.9, where the terms h and v refer to the length of the horizontal axis and the length of the vertical axis of the body. The candidate kidney region (R_k) is within two rotated ellipses, which are located at a distance of $0.28h$ from the spine. After analysing 20 CTC data sets, the dimensions of the ellipse were found to be $0.13h \times 0.2v$ (short axis $\times$ long axis) and the rotation angles were found to be 60^o for the left kidney and -60^o for the right kidney. Therefore, the two kidney regions can be represented as follows:

$$\begin{aligned} left\_kidney: (xcos60^o - zsin60^o)(xcos60^o - zsin60^o)/(0.13h * 0.13h) \\ +(zcos60^o + xsin60^o)(zcos60^o + xsin60^o)/(0.2v * 0.2v) \leq 1 \end{aligned} \tag{4.2}$$

$$\begin{aligned} right\_kidney: (xcos(-60)^o - zsin(-60)^o)(xcos(-60)^o - zsin(-60)^o)/ \\ (0.13h * 0.13h) + (zcos(-60)^o + xsin(-60)^o)(zcos(-60)^o + \\ xsin(-60)^o)/(0.2v * 0.2v) \leq 1 \end{aligned} \tag{4.3}$$

The two kidneys are actually not bilaterally symmetrical; the right kidney being approximately 1 cm lower than the left, due to its location inferior to the liver (Gray, 1977). Thus, a kidney region appears earlier on the left side of the body when viewing the data set in a top-down manner. In addition, Emamian *et al.* (1993) have reported normal dimensions for each kidney in adults, which are 11.2 cm for the length of the left kidney and 10.9 cm for the right along a standard longitudinal view of the kidney. This information indicates how many slices contain a kidney region along the long axis of the body. Consequently, kidney regions can be extracted in the same way as the lungs and the liver.

Spleen

The spleen is situated in the left upper abdominal quadrant of an abdominal CT data set acquired in the supine position and its normal dimensions are 4 × 7 × 11 cm (thickness × width × length) (Burgener & Kormano, 1996). Based on this anatomical feature, Campadelli *et al.* (2009) used a box to define the region occupied by the spleen, shown in Figure 4.10. In the segmentation method proposed in this chapter, this box is placed on each slice of the data set to search for the spleen region. Although some other organs, such as the left lung and the

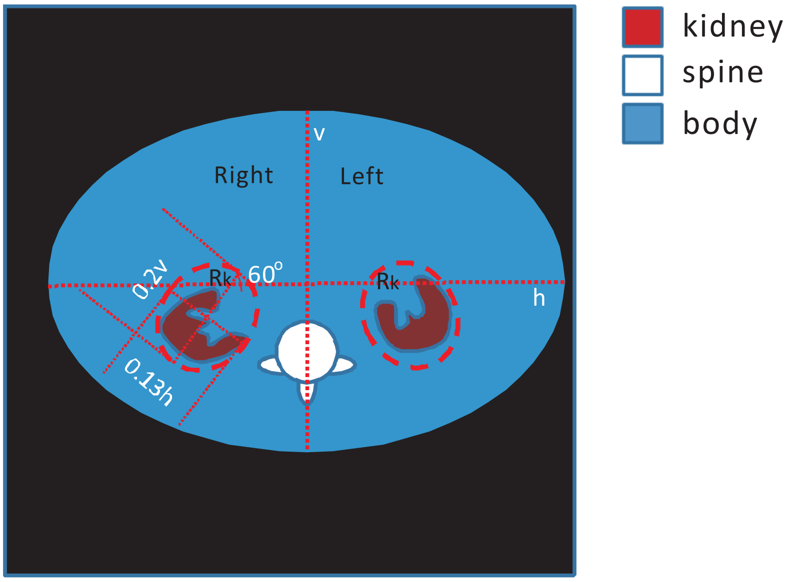

Figure 4.9: An illustration of the kidney region identification process. The candidate kidney regions (R_k) are indicated within the red dashed ellipse.

left kidney, exist inside the box area, these organs have already been segmented and hence can be directly excluded from the spleen region. Therefore, the previous segmentation results are helpful in accomplishing spleen segmentation.

It should be noted that the spleen is in direct contact with the left kidney, which means some overlapping regions exist between the candidate areas for the left kidney and the spleen. In order to avoid processing the same data twice, the spleen detection stops once the left kidney appears in the data set.

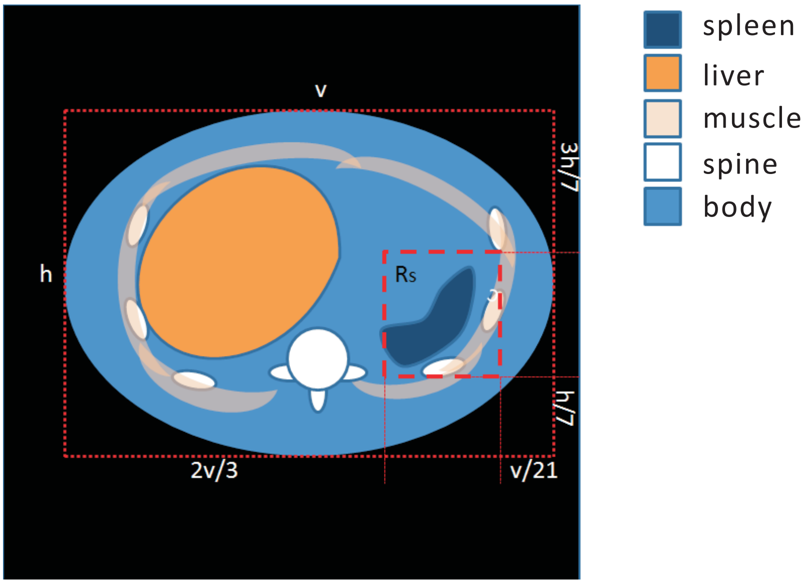

Figure 4.10: An illustration of the spleen region identification process. The candidate spleen region (R_s) is indicated within the red dashed box.

4.5 Automatic Segmentation in the Context of Compression

4.5.1 The Proposed Segmentation Method

The proposed segmentation method extracts different regions in a progressive manner, from the most straightforward to the most complex. The flowchart of the segmentation process is shown in Figure 4.11. After the body area and the region outside the scan area are extracted, bone, bone PVE, colon, colon PVE, body PVE, clothing, table and external air regions are identified based on their density features and the previous segmentation results, i.e. the body outline. These segmented regions can be used to provide useful information to guide the subsequent segmentation process, which is used to extract the specific organs. This is achieved using segmentation based on the combination of density and anatomical features. After the organ segmentation is finished, the remaining voxels within the body area are either assigned to adipose tissue or lean tissue based on their density features. It should be noted that the proposed segmentation method is designed in a hierarchical fashion. Based on this approach, mistakes in the earlier steps cannot be corrected in the subsequent stages. Therefore, the earlier segmentation steps need to minimise under- or over-segmentation as much as possible. Due to this requirement, some regions, e.g. bone and colon, which have distinguishing features are segmented earlier. High segmentation accuracy can be achieved in these regions, thus ensuring the greatest possible accuracy in the following steps during the segmentation process.

This region segmentation is implemented in the context of compression. The proposed compression technique is based on predictive coding. For this type of compression technique, only previously encoded pixels will be available to decode the data, thus only previously encoded pixels can be used during the segmentation process. However, due to the fact that the anatomical structures inside the CTC data set show a high level of homogeneity, it is feasible to predict the category of the current pixel based solely on the subset of neighbouring pixels whose values are known.

The proposed method uses the JPEG prediction template for the purpose of region identification. Automatic identification is accomplished by examining the two known face connected neighbours of the current pixel (see Figure 4.12). The details of this process are as follows:

Inside the body:

```
If $P_N \epsilon$ bone & $P_W \epsilon$ bone $\Longrightarrow X \epsilon$ bone
else if $P_N \epsilon$ air & $P_W \epsilon$ air
        if $L_X \epsilon$ lung $\Longrightarrow X \epsilon$ lung
        else $X \epsilon$ colon
```

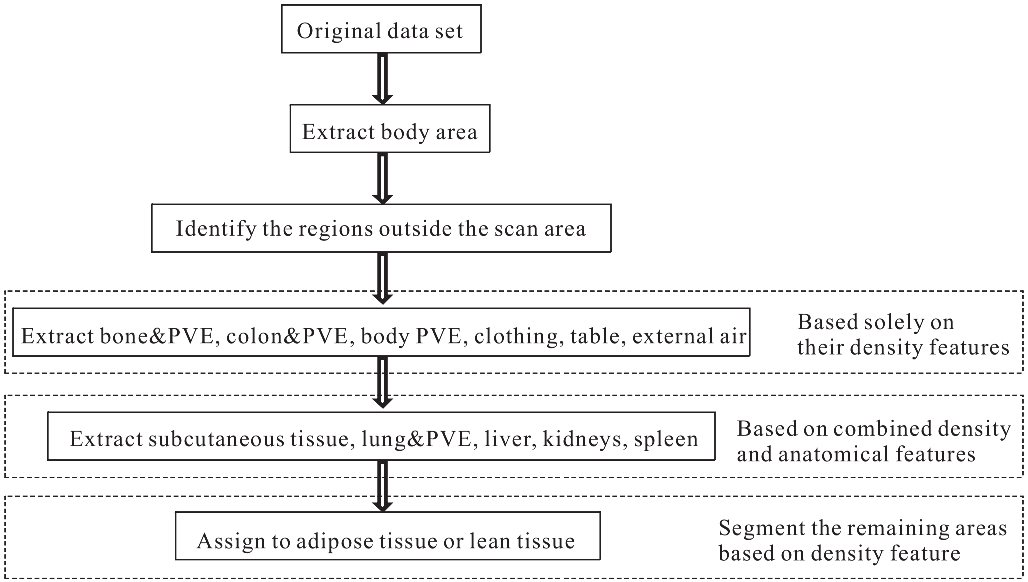

Figure 4.11: Flowchart of the segmentation process using the proposed technique.

```
else if $P_N \epsilon$ soft tissue & $P_W \epsilon$ soft tissue
        if $L_X \epsilon$ liver $\Longrightarrow X \epsilon$ liver
        if $L_X \epsilon$ left kidney $\Longrightarrow X \epsilon$ left kidney
        if $L_X \epsilon$ right kidney $\Longrightarrow X \epsilon$ right kidney
        if $L_X \epsilon$ spleen $\Longrightarrow X \epsilon$ spleen
        else $X \epsilon$ lean tissue
else if $P_N \epsilon$ PVE & $P_W \epsilon$ PVE
        if $L_X$ near bone $\Longrightarrow X \epsilon$ bonePVE
        if $L_X$ near colon $\Longrightarrow X \epsilon$ colonPVE
        if $L_X$ near lung $\Longrightarrow X \epsilon$ lungPVE
else $X \epsilon$ adipose tissue
  On the body boundary:
if $L_X \epsilon$ bodyPVE $\Longrightarrow X \epsilon$ bodyPVE
if $L_X \epsilon$ subcutaneous tissue $\Longrightarrow X \epsilon$ subcutaneous tissue
  Outside the body but inside the scan area:
If $P_N \epsilon$ table & $P_W \epsilon$ table $\Longrightarrow X \epsilon$ table
else If $P_N \epsilon$ clothing & $P_W \epsilon$ clothing $\Longrightarrow X \epsilon$ clothing
else $X \epsilon$ external air
```

where P denotes the pixel value and L denotes the location.

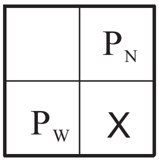

Figure 4.12: The template used for region identification.

Therefore, the proposed segmentation technique in the context of compression is performed by a simple prediction template combined with the density and anatomical features.

4.5.2 Experiments and Results

The segmentation strategies discussed in the previous sections of this chapter were applied to three CTC data sets. Figure 4.13 illustrates all 17 categories segmented by the proposed method. From a visual evaluation of these results, it can be observed that almost all pixels in the image are assigned to the correct category. This achievement can be attributed to the inclusion of the anatomical knowledge in the segmentation process.

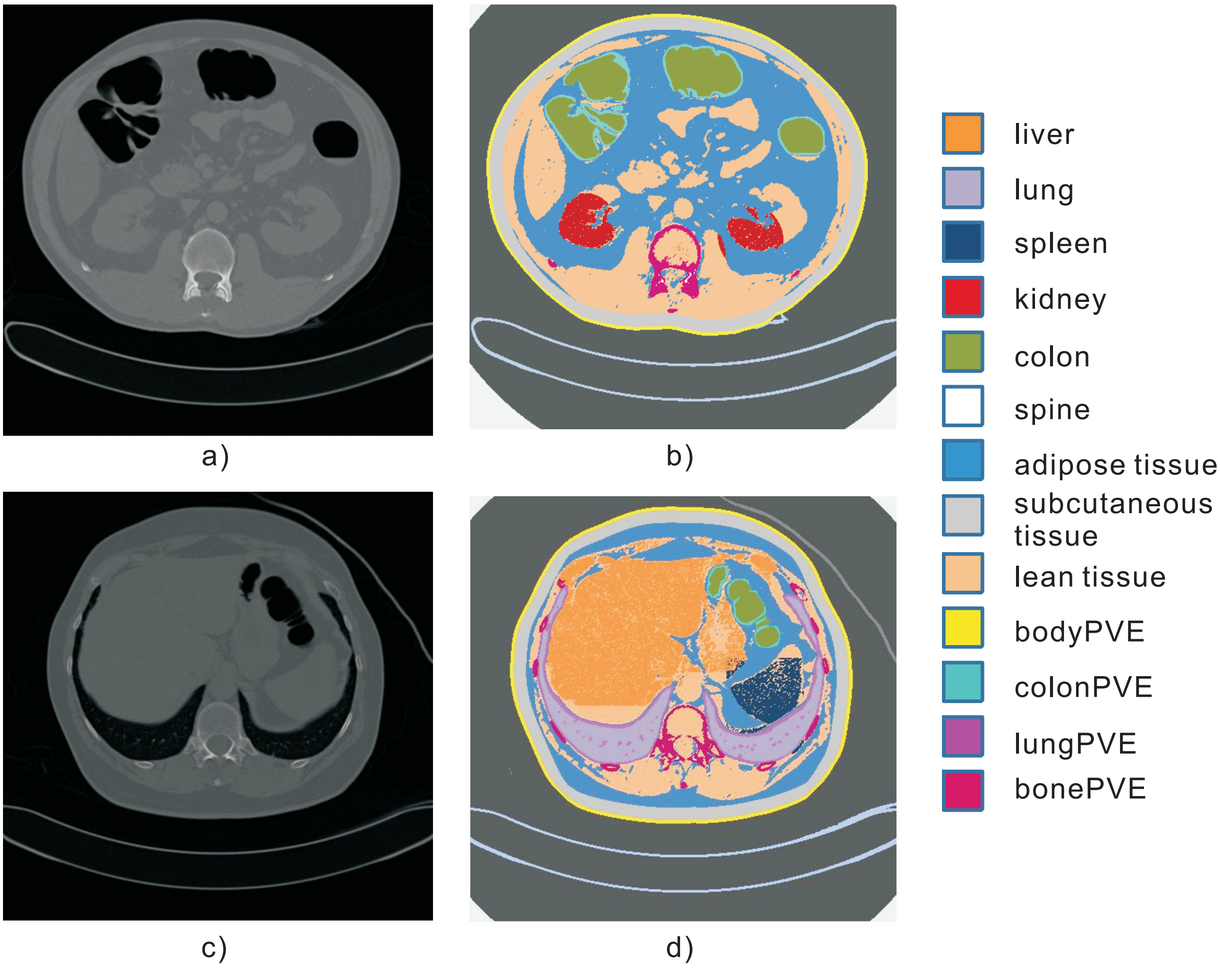
a) b) c) d)

Figure 4.13: The segmentation results using the proposed technique. (a, c) original images. (b, d) segmented images.

In order to assess the performance of segmentation algorithms, several evaluation methods have been proposed, such as evaluation metrics-based clustering (Jiang *et al.*, 2005), local and global consistency error (Martin *et al.*, 2001) and the Huang-Dom evaluation measure (Huang & Dom, 1995). These techniques are used to measure the discrepancy between an automatic segmentation result and a ground truth data set of manually segmented images. Among these evaluation techniques, the Jaccard similarity coefficient (JSC), which is a metrics-based measurement, is one of the most popular evaluation methods due to its simplicity and robustness. As a result, this approach was selected for use in this evaluation. The Jaccard similarity coefficient represents the similarity between the automatically segmented region (S_1) and the manually segmented one (S_2). A higher value of this coefficient indicates a more accurate segmentation result. The JSC is calculated using the following equation:

$$I(S_1, S_2) = (S_1 \cap S_2)/(S_1 \cup S_2) \tag{4.4}$$

The statistical evaluation was performed on two anatomical regions, the colon and the kidneys. The ground truth of the colon region was manually traced by two experienced radiologists, whereas the left and right kidney regions were manually segmented by a medical imaging expert in the Centre for Image Processing and Analysis in Dublin City University. The similarity of the measurements from the automatic segmentation results in comparison with the manual segmentations are presented in Table 4.2. Three CTC data sets were randomly selected from the database (see Appendix A) and used in the experiment. The IDs of these data sets are 1, 2 and 11. The number of slices per data set were 246, 284 and 238.

As shown in the table, the average overlap rates between the ground truth and the proposed segmentation method are approximately 0.86 for the colon and 0.46 for the kidneys. It should be noted that kidney segmentation is the most difficult

Table 4.2: Statistical evaluation of colon and kidney segmentation quality.

Data set	3D dimension	DSC		
		Colon	Left kidney	Right kidney
1	512 × 512 × 246	0.89	0.18	0.49
2	512 × 512 × 284	0.89	0.49	0.52
11	512 × 512 × 238	0.80	0.49	0.52

task in the whole segmentation process. This is due to the fact that the kidneys have nearly the same density range as the surrounding soft tissue, which means it is not easy to distinguish between them. In addition, variations in the kidney shape and position make the segmentation task even harder. This is particularly true in the case of data set 1, where a poor segmentation result was obtained due to the fact that the left kidney was not in the expected location. As a result, the proposed segmentation method could not provide a high level of accuracy in this region. However, as shown in Figure 4.13, the incorrectly segmented kidney is treated as the lean tissue. Considering that both the kidneys and the lean tissue regions have almost the same properties, application of the compression method designed for the lean tissue to the incorrectly segmented kidney will not significantly degrade the overall compression result and consequently this segmentation result is still acceptable. It should also be noted that other regions, such as the lungs and bone, have strong anatomical and density features and higher segmentation accuracy can be expected in these cases.

4.5.3 Discussion

A segmentation method has been proposed that complements the density feature with anatomical information. This method is designed for segmentation of specific organs in abdominal CT data sets. The candidate region of each organ is first obtained based on prior anatomical knowledge of the current data set. A density-based method is then used in this candidate region to accurately extract the organ.

There are several merits associated with this technique. Firstly, CT scans can be performed with different settings, which will result in a difference in the size of the body region in the images. The proposed approach exploits a relative position of the organ in the body, thus, it is applicable to images of different patient sizes. Secondly, this technique is performed in a progressive manner that roughly defines a candidate region and then refines the target region using a density-based segmentation method. Based on this approach, segmentation accuracy is not significantly affected by small anatomical variations. Twining *et al.* (2007) listed a number of common abdominal abnormalities which are presented in Table 4.3. It is clear from this table that the liver is the most frequent source of abnormality. Chronic liver disease usually causes a reduction in liver size where regions normally occupied by liver are occupied by fat instead. When implementing segmentation, the candidate region for the liver is extracted according to the ideal anatomical model. However, liver and fat have significantly different densities. Thus, the region outside the liver will not be detected based on the density feature during the refinement process. This procedure ensures that the proposed technique is not sensitive to organ size. In the case of other organs, they can be segmented based on the same procedure. Twining *et al.* (2007) identified that the spleen and kidneys are the second and third most common sources of abnormality and the proposed technique can also adapt to accurately segment these organs if abnormalities are present. It should be noted that other common abnormalities associated with small organs, such as gall bladder, are not addressed by the proposed segmentation technique. However, these organs only represent a small part of the whole body and have nearly the same density features as soft tissue, thus, they are treated as soft tissue in the proposed method for the sake of simplicity and efficiency.

Table 4.3: Common sources of abnormalities within the abdomen.

Rank (based on how frequently the abnormality occurs at each location)	Location of the abnormality	Disease that causes the abnormality
1	Liver	Chronic liver disease
		Liver tumours
		Liver cysts
2	Gall bladder	Gallbladder disease
3	Spleen	Splenic cysts
		Splenomegaly
4	Adrenal glands	Adrenal masses
		Adrenal cysts
		Adrenal haemorrhage

In summary, the proposed technique exploits both anatomical and density features to guide the segmentation process. It can be used to segment individual organs from medical data sets and can adapt to anatomical variability that exists among different patients. This helps to reduce segmentation errors which ultimately helps to improve the operation of the subsequent compression stage.

4.6 Conclusion

The aim of this chapter was to develop a segmentation method in the context of medical image compression. Due to its use for data compression, only previously encoded voxels are available for the segmentation process. None of the conventional segmentation approaches can be applied. Consequently, a custom segmentation method that combines anatomical and density features with a series of image processing techniques has been proposed. Most regions in the CTC data set are initially extracted based on their density features, e.g. bone, clothing, and external air. However, the specific organs, e.g. the liver and the kidneys, cannot be segmented using density-based segmentation techniques. This is due to the fact that most of these organs have similar density values and hence it is impossible to distinguish between them relying solely on density features. In the proposed method, the density information is thereby complemented with the anatomical features in the organ segmentation process. The anatomical position and size of each organ can be used as a priori knowledge to guide the segmentation. The experimental results confirm that this method can achieve acceptable segmentation accuracy and is appropriate for use in the context of data compression.

This anatomy-based segmentation method forms the basis of an adaptive prediction model that is elaborated on in subsequent chapters.

Chapter 5

Adaptive Prediction Model

Data decorrelation is one of the main components of a compression scheme. This is accomplished by subtracting the predicted pixel value from the actual pixel value. A highly accurate prediction model can result in good compression performance. This chapter presents an adaptive modelling method that exploits anatomical features to significantly improve the accuracy of the prediction model. The proposed method uses the segmentation technique described in Chapter 4 to divide the original data into different regions and subsequently generates a series of predictors that are optimised for these specific regions. There are two main region categories within a CTC data set, which are edge and interior regions. Both of these categories have significantly different statistical characteristics and, consequently, separate modelling approaches are utilised to generate optimised predictors for each of these categories. The combination of the predictors in both categories ultimately creates the adaptive prediction model.

5.1 Interior-based Prediction Model

Bone, air, and other segments (except PVE regions) are examples of interior regions where a high degree of smoothing is present. This characteristic makes modelling the interior regions relatively simple as the value of the pixels is typically constant. Thus, generating the optimised predictor only requires the identification of an optimum predication template.

It is a common rule that a prediction model can only use past observations. When processing the data frame by frame and in a raster-scanned order within a frame, the set of past observations includes all pixels in the previous frames, the pixels in the current frame that lie above the current pixel, and the pixels in the current scanline that lie to the left of the current pixel. However, if all the previous pixels are used in the prediction, a multicollinearity problem is likely to occur due to the fact that some previous pixels are not useful for prediction. On the other hand, in order to reduce the computational complexity, the insignificant pixels should be removed from the prediction model.

Therefore, this section discusses how to choose a series of neighbouring pixels to create an optimised predictor. Two specific issues will be addressed, which are the selection of the template structure and the choice of the template size. These two factors ultimately determine the number of causal pixels to be used in the prediction model.

5.1.1 Template Identification

As previously indicated in Section 2.2.2, there are some correlations that can be utilised to predict current pixel values, such as spatial and temporal correlations. These correlations mainly exist between the current pixel and its surrounding neighbours. Thus, these neighbours are usually involved in the development of a prediction model. The combination of these surrounding pixels is determined by a prediction template. The general prediction template can be classified into three categories. These are diamond-based (Wu & Memon, 1997; Motta *et al.*, 1999), circle-based (Wu & Memon, 2000) and square-based templates (Weinberger *et al.*, 1996; Li & Orchard, 2001; Knezovic *et al.*, 2006). Figures 5.1, 5.2 and 5.3 present the 3D versions of these templates.

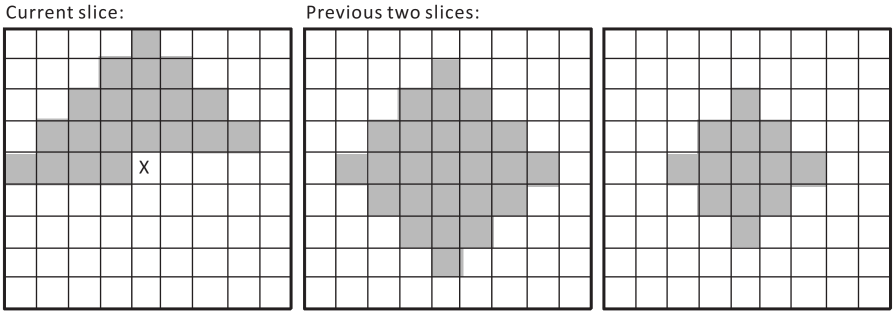

Figure 5.1: The diamond template used for prediction. The size of this template is 9 pixels.

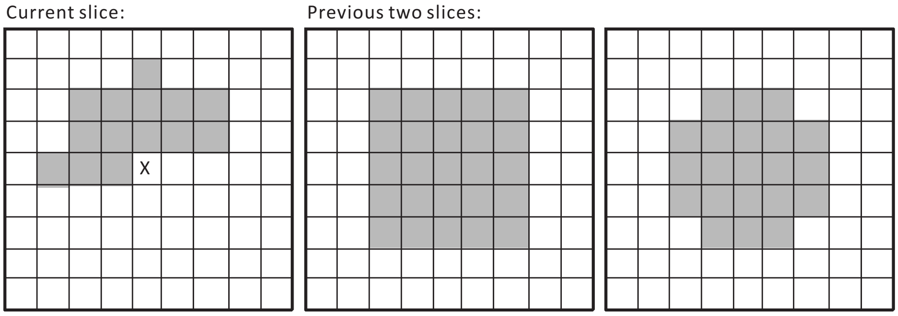

Figure 5.2: The sphere template used for prediction. The radius of this template is 3 pixels.

In order to determine the prediction efficiency of different template structures, a numerical evaluation was carried out using 20 training data sets. The details of these data sets are described in Appendix A. This evaluation is designed to test the hypothesis that, given the same number of input variables, the optimal

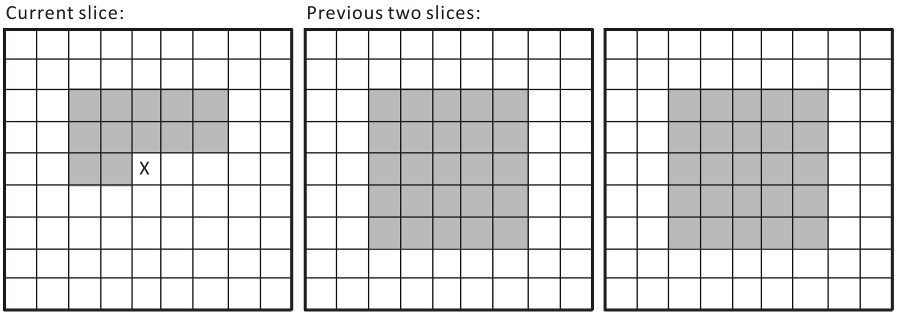

Figure 5.3: The cube template used for prediction. The size of this template is 5 pixels.

template strategy is the one that achieves the smallest entropy of the residual data. The linear prediction model for each template structure is generated using the least mean square principle. This process has been described in Section 2.2.1. The template sizes used in this test are presented in Table 5.1. The experimental results for the application of each template on the different regions, i.e. bone, soft tissue, adipose tissue and air, are shown in Figures 5.4, 5.5, 5.6 and 5.7 respectively.

As shown in these figures, although all of the templates have almost the same performance with respect to decorrelation, the diamond-based technique is slightly more accurate than the other two techniques in all cases. In addition, n-fold cross-validation was used to assess whether the diamond template is an optimal technique in practice. This was achieved by randomly dividing the training data sets into 5 subsets of equal size. Then one of the 5 subsets was selected as the testing data and the remaining 4 subsets were used as the training data. This process was repeated 5 times so that every subset was used once for testing. The results of this cross-validation are shown in Table 5.2. It is clear from this table that the diamond-based technique achieves the lowest entropies on all of the test data, thus confirming the validity of the proposed template.

Table 5.1: The number of causal pixels associated with different sizes of diamond-based, sphere-based and cube-based templates.

Template size (pixels)	Number of causal pixels	Template size (pixels)	Number of causal pixels	Template size (pixels)	Number of causal pixels
Diamond size=5	12	Sphere radius=2	16	Cube size=3	22
Diamond size=7	30	Sphere radius=3	60	Cube size=5	62
Diamond size=9	58	Sphere radius=4	106	Cube size=7	122
Diamond size=11	96	Sphere radius=5	176	Cube size=9	202
Diamond size=13	144				

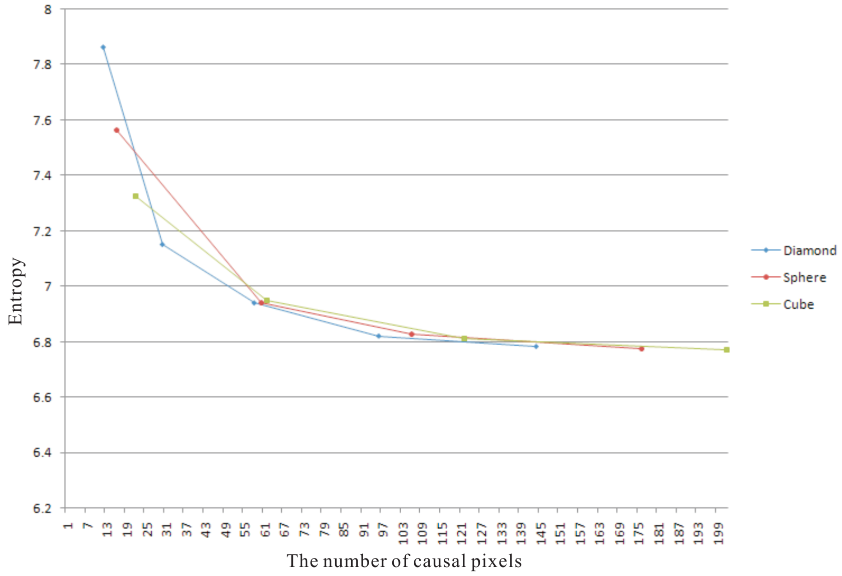

Figure 5.4: The average residual entropies of the bone region tested on 20 CTC data sets.

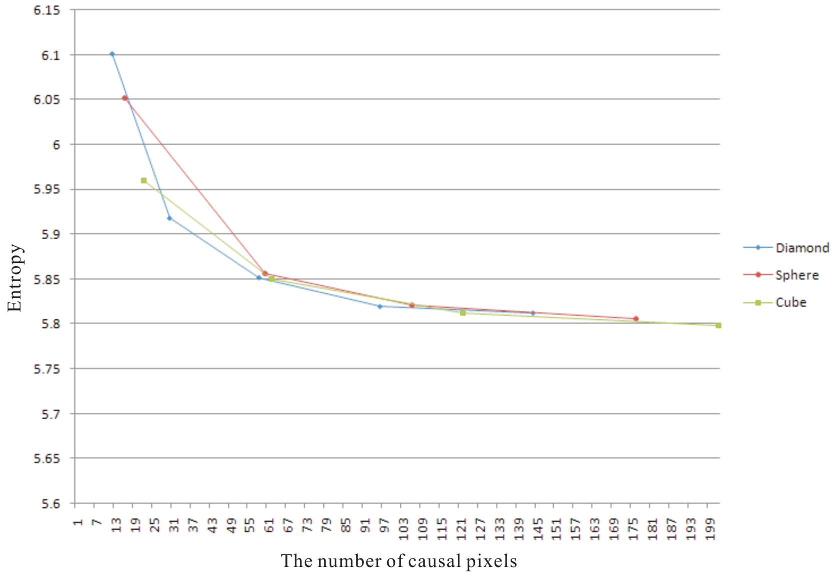

Figure 5.5: The average residual entropies of the soft tissue region tested on 20 CTC data sets.

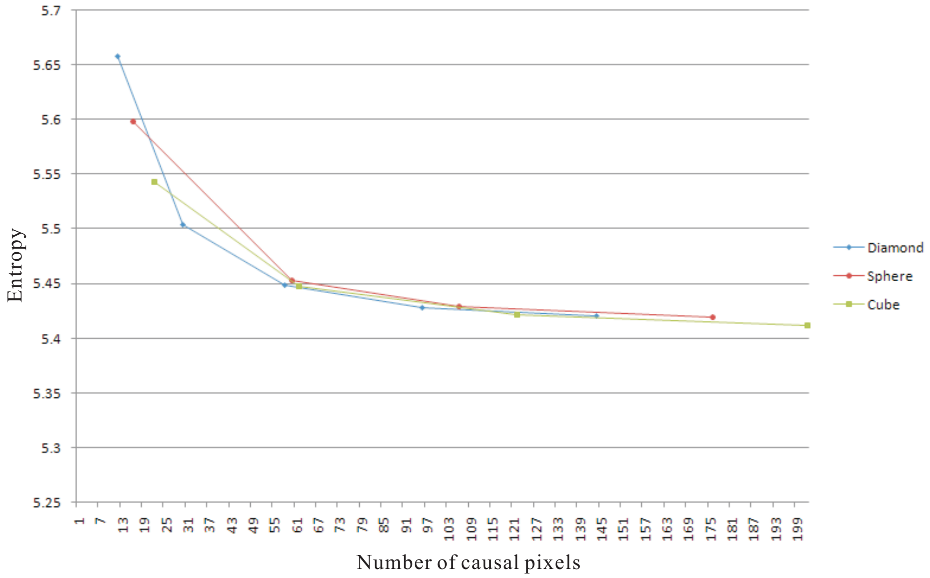

Figure 5.6: The average residual entropies of the air region tested on 20 CTC data sets.

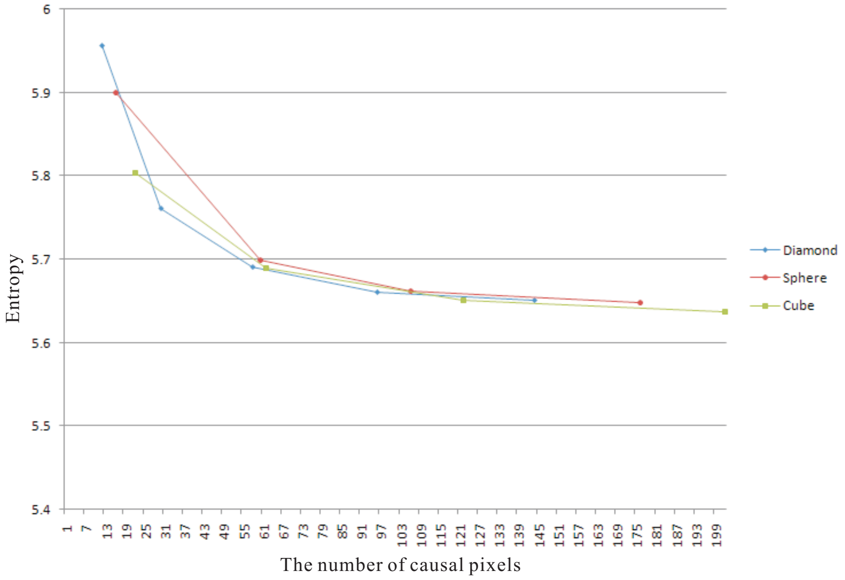

Figure 5.7: The average residual entropies of the adipose tissue region tested on 20 CTC data sets.

Table 5.2: The results of the cross-validation study comparing the performance of the different templates. D represents diamond, S represents sphere and C represents cube. The sizes of diamond, sphere and cube are 9, 3 and 5 pixels respectively.

Test	Training result (The optimal template)				Testing result (The entropy after prediction using different templates)											
	Air	Soft tissue	Adipose tissue	Bone	Air			Soft tissue			Adipose			Bone		
					D	S	C	D	S	C	D	S	C	D	S	C
1	D	D	D	D	**5.41**	**5.41**	**5.41**	**5.70**	**5.70**	5.71	**5.62**	5.63	5.63	**7.06**	7.07	7.08
2	D	D	D	D	**5.36**	5.37	5.38	**5.75**	5.76	5.77	**5.56**	5.57	5.58	**7.02**	7.03	7.06
3	D	D	D	D	**5.85**	5.86	5.86	**6.38**	**6.38**	**6.38**	**6.13**	6.14	**6.13**	**7.28**	**7.28**	7.31
4	D	D	D	D	**5.41**	5.42	5.42	**5.74**	5.75	**5.74**	**5.66**	5.67	5.67	**6.73**	**6.73**	6.74
5	D	D	D	D	**5.18**	5.19	5.19	**5.67**	5.68	**5.67**	**5.47**	5.48	5.48	**6.60**	6.61	6.61

The superior performance obtained using the diamond-based technique can be explained by the fact that the slice thickness in CTC data sets is much larger than the intraslice resolution. In this case, the spatial correlation is strong and the temporal correlation is relatively weak. Thus, the neighbouring pixels in the current slice are more significant than the pixels in the previous slices. Based on this observation, the diamond- and cube-based prediction techniques provide better prediction performances than the sphere-based prediction technique due to the fact that they use more pixels in the current slice than the sphere-based technique given the same number of input causal pixels. However, the cube-based template includes some pixels that are quite far away from the pixel being compressed, i.e. pixels at the corners. These pixels are less significant in the prediction model compared to those located in closer proximity to the current pixel. Therefore, the diamond-based prediction technique achieves the best performance among the three prediction techniques due to its efficient combination of the most significant neighbours to generate the prediction model.

After the diamond-based template has been chosen, the next issue is to identify a suitable template size. This size determines the number of causal pixels in a prediction model. It should be considered that increasing the number of variables in a prediction model improves the fitting performance to the data. However, the inclusion of too many causal pixels is likely to significantly increase the computational cost. Therefore, it is necessary to identify an adequate template that can give high prediction accuracy with fewer causal pixels.

As can be seen in Figures 5.4 - 5.7, the residual entropies for all the regions decrease dramatically when the number of causal pixels is increased in the initial stage. After the number of causal pixels reaches a certain value, the entropy decrease achieved by the increasing the number of causal pixels is very small. Thus, this value can be seen as the best choice for the template size as increasing the number of causal pixels further leads to high computational complexity while providing only minor gains with regard to compression.

It can be seen from Figure 5.5 that there is no significant improvement in performance when the number of causal pixels is above 58. Therefore, the best choice for the template size of the diamond shape for the soft tissue region is 9 pixels. The same conclusion can be drawn from Figures 5.6 and 5.7: that the most suitable template sizes for air and adipose tissue regions are also 9 pixels. In the case of bone regions, a template size of 11 pixels is shown to be the best choice as indicated in Figure 5.4. This is motivated by the fact that the bone region represents a higher level of variation comparable to the regions of soft tissue, air and adipose tissue. In this case, more causal pixels are required in order to accurately model this region.

5.1.2 Model Determination

Once the template is determined, the next step involves generating a prediction model based on this template. A linear prediction model is chosen in this study and can be expressed as follows:

$$\hat{p} = \beta_0 + \beta_1 x_1 + \beta_2 x_2 + ... + \beta_N x_N \tag{5.1}$$

where $\hat{p}$ is the predictive value, $x_1, x_2...x_N$ are the prediction causal pixels and $\beta_0, \beta_1...\beta_N$ are the coefficients of the prediction model. N=58 for the soft tissue, air and adipose tissue regions, while N=96 for the bone region.

The optimised coefficients of each causal pixel can be calculated by the least mean square principle. This process will be repeated on each segmented region, e.g. kidneys and liver. Consequently, the optimised predictors for bone, liver, kidneys, spleen, lean tissue, air in lungs, air in colon, subcutaneous fat, other adipose tissue, scanning table, clothing and the air outside the patient are generated. The adaptive model ultimately combines all these subpredictors and can be expressed as follows:

$$\begin{aligned} M = \big\{R, P\,\big\{&P_{bone}, P_{liver}, P_{kidneys}, P_{spleen}, P_{lean\_tissue}, P_{air\_lung}, P_{air\_colon}, \\ &P_{subcutaneous\_tissue}, P_{adipose\_tissue}, P_{table}, P_{clothing}, P_{external\_air}\big\}\big\} \end{aligned} \tag{5.2}$$

where R is the specific region and P is the corresponding predictor.

This process is implemented only once and then the coefficients for each predictor are stored in the header of the compressed data.

5.2 Edge-based Prediction Model

Compression at the edges is more difficult than in the interior regions due to the changing nature of the data distributions. Therefore, a number of specific edge-based prediction methods have been designed for image compression, i.e. GAP, EDP and MED. However, medical images have distinctive characteristics that are different from natural images, particularly in the case of the intensity profile of edge regions which is much smoother due to the PVE. This difference is illustrated in Figure 5.8. Although GAP caters for several edge categories, it performs best in areas that contain strong edges. Therefore it is more appropriate for use with real world images. EDP is not appropriate for use with medical images as this technique uses directly connected neighbours and, consequently, it is only useful in images with strong edges. Extending EDP to deal with the smooth edges found in medical images would negate the main benefit associated with this approach, i.e. computational efficiency, as the number of pixels to be processed would increase significantly. MED is also limited to dealing with strong edges and as such is not suitable for use with medical images either. In addition, studies of GAP and EDP have shown that MED does not perform as well as these approaches (Wu & Memon, 2000; Li & Orchard, 2001).

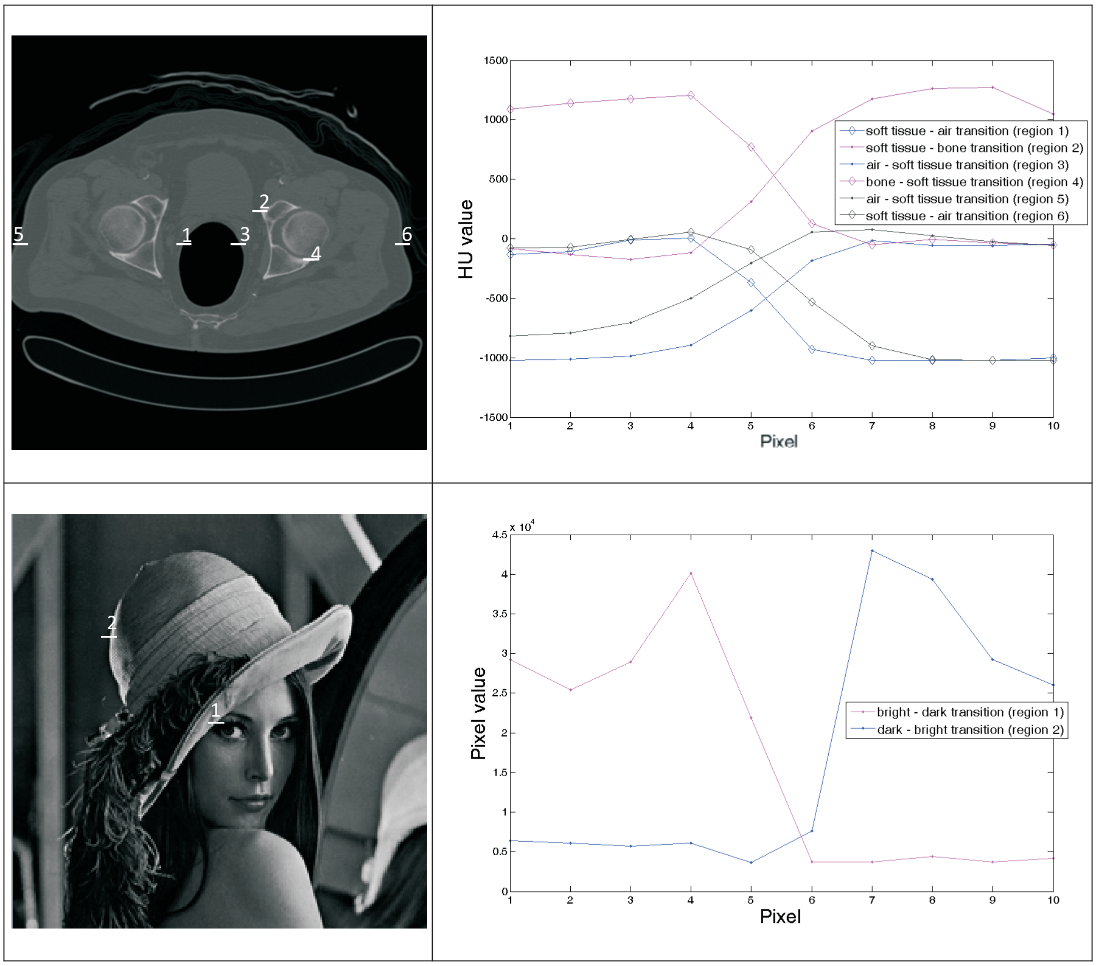

Figure 5.8: Edge transitions in an example CT image and a natural image. The upper left image is a 16-bit CT image and the upper right image is the profile plot corresponding to the lines in the CT image. The lower left image is a 16-bit grey-scale Lena image and the lower right image is the profile plot corresponding to the lines in the Lena image.

It is clear from the review provided above that the edge-based predictors that are currently available are not ideally suited for use with medical image data. Consequently, there is a need to develop an edge-based prediction technique specifically for use with the types of edges associated with the PVE regions commonly found in medical image data.

5.2.1 Estimation of the Normal Direction

When generating a prediction model, it is very important to consider the organisation of the input variables. If the input pattern is inconsistent, the efficiency of the prediction model is significantly decreased. Figure 5.9 shows an inconsistent approach for generating input variables for PVE regions. If the template is simply placed on each PVE pixel, the pattern of the input variables is inconsistent as shown. For example, the first input variable has a high density value in case 3, while the first input variable for case 1 has a low value. The fact that the input pattern is inconsistent means that it is almost impossible to generate a reliable prediction model.

These inconsistent situations can be completely avoided by rotating the template based on the edge normal (see Figure 5.10). This ensures the template is always aligned with the edge region.

The Zucker-Hummel edge operator (Zucker & Hummel, 1981) is commonly used in medical imaging applications, for example Kovalev *et al.* (2001), Mykkäen *et al.* (2005) and Chowdhury *et al.* (2005). The standard version of this edge operator uses the 26 directly connected neighbours of the current voxel in order to determine the normal direction and magnitude at that point. However, in the context of compression, only previously encoded pixels can be used for normal calculation. Thus, an alternative method for normal calculation is required in this context.

Common edge detection techniques use derivatives to identify edge regions.

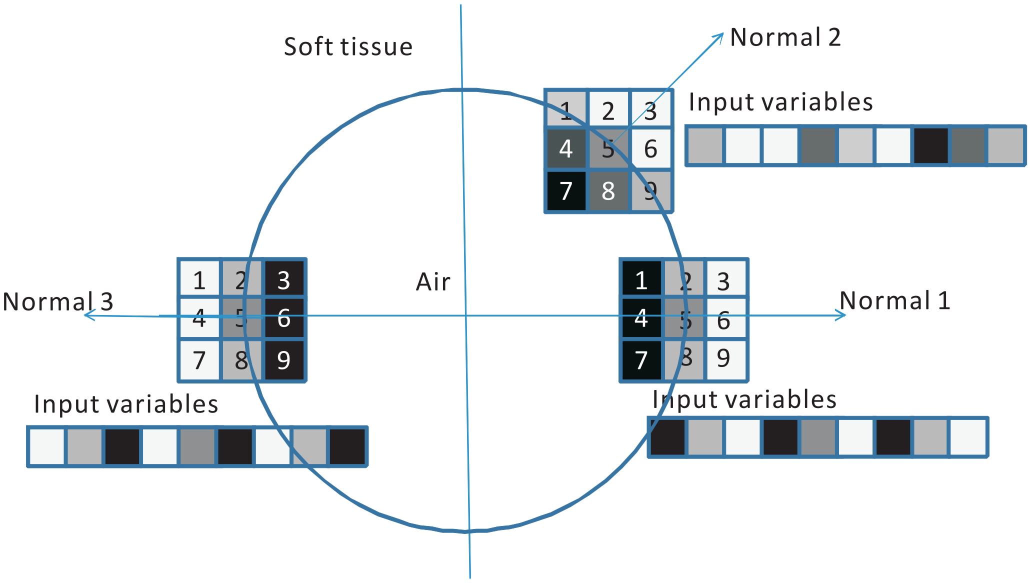

Figure 5.9: An unoptimised approach for organising the input variables used by a PVE prediction scheme. The order of input variables is indicated by the numbers in the templates.

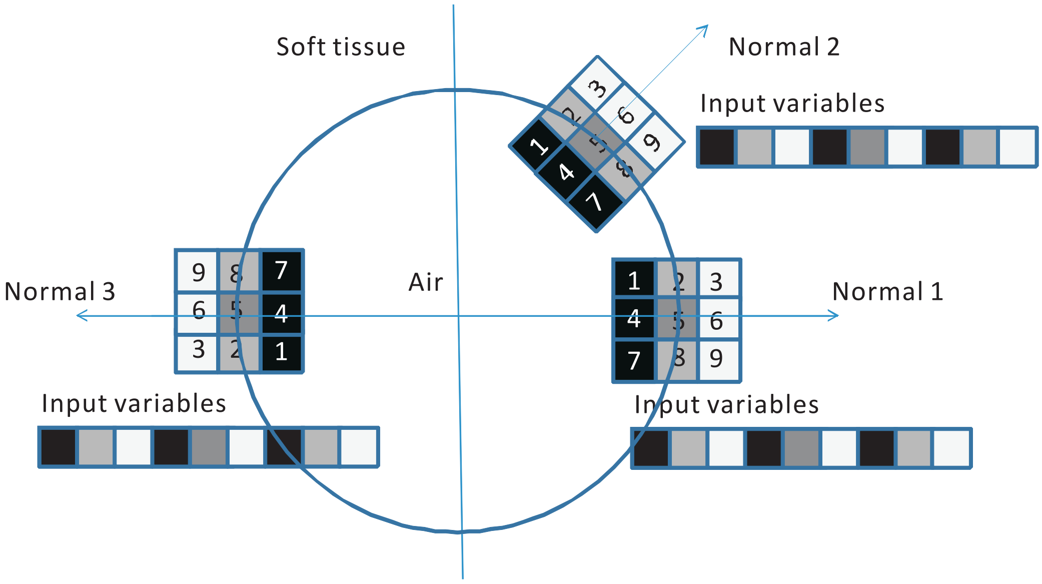

Figure 5.10: An optimised approach for organising the input variables used by a PVE prediction scheme where the template has been rotated according to the edge normal.

In the case of the first derivative, local minima and maxima are indicative of the presence of edges. Let $y = f(x)$ be a function of a density profile. The derivative of f at point x can be expressed as follows:

$$f'(x) = \lim_{h \to 0} \frac{f(x+h) - f(x)}{h} \approx f(x+1) - f(x) \quad (h = 1) \tag{5.3}$$

Therefore, the corresponding two-pixel edge detection mask is [-1, 1].

On the other hand, if a function has a derivative at a certain point, the right-hand and left-hand derivatives are equal to the derivative at that point. Let $f'_{-}(x)$ be the left-hand derivative of $f(x)$ at x and $f'_{+}(x)$ be the right-hand derivative of $f(x)$ at the same point. Thus, the following equation can be obtained:

$$\begin{aligned} f'(x) = \frac{f'_{-}(x) + f'_{+}(x)}{2} &= \frac{\lim_{h \to 0} \frac{f(x)-f(x-h)}{h} + \lim_{h \to 0} \frac{f(x+h)-f(x)}{h}}{2} \\ &\approx -\frac{1}{2} f(x-1) - 0 f(x) + \frac{1}{2} f(x+1) \quad (h = 1) \end{aligned} \tag{5.4}$$

This corresponds to a new edge detection mask with a combination of three connected pixels [- $\frac{1}{2}$, 0, $\frac{1}{2}$] (centred about x). Based on these masks, a new 3D edge operator for use in the context of compression that only uses previously encoded pixel data is developed. The masks for this operator are presented in Figure 5.11.

5.2.2 Quantisation of the Angle

It is clear from the discussion in Section 5.2.1 that it is not appropriate to use a fixed template to generate the input variables for the predictor. However, if the template is rotated based on the edge normal, the pattern of the input variables is consistent (see Figure 5.10). Rotation of the template in a continuous manner is computationally intensive, as it is necessary to use 3D interpolation. Thus,

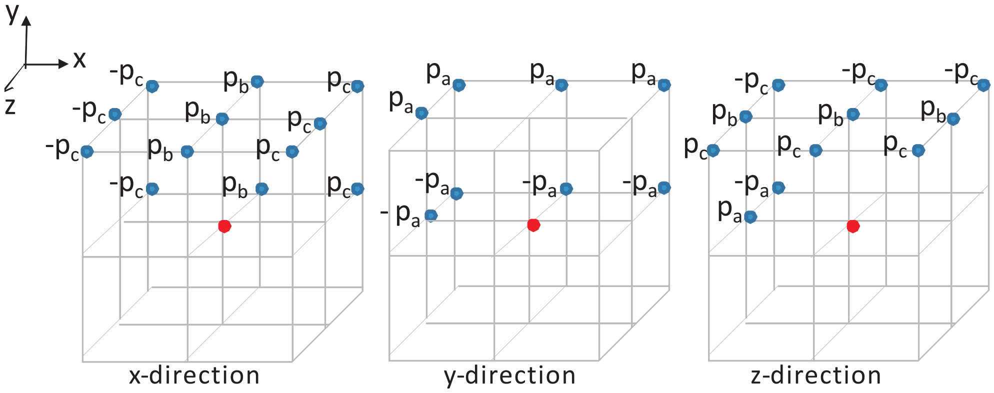

Figure 5.11: The new 3D normal calculator for use in the context of compression where $p_a = 1$, $p_b = 0$ and $p_c = \frac{1}{2}$. (the centre point (in red) is the current pixel)

for the sake of simplicity, discrete orientations of the normal are used instead. In the case of the XZ plane, a total of eight discrete orientations of the normal are defined: $0^o, 45^o, 90^o, 135^o, 180^o, 225^o, 270^o$ and 315^o (see Figure 5.12). If the actual angle is not equal to one of these eight angles, it is quantised to the nearest one. Additionally, in order to avoid pixel scaling at $45^o, 135^o, 225^o$ and 315^o it is necessary to develop an additional template for the normals in these directions. Therefore, two template categories are defined in the XZ plane according to the normal directions: one is along the axis and the other is at an angle of 45^o to the axis. The other templates in the top and bottom horizontal planes, illustrated in Figure 5.12, are defined in a similar way and the full details of all the template categories are presented in Table 5.3.

5.2.3 Model Determination

Once the normal has been determined, the predictors for each orientation are generated based on the cube template. The cube template is chosen due to the fact that it can give a consistent performance across different edge directions. A template size of 5 pixels is used in the edge-based predictor so as to maximise

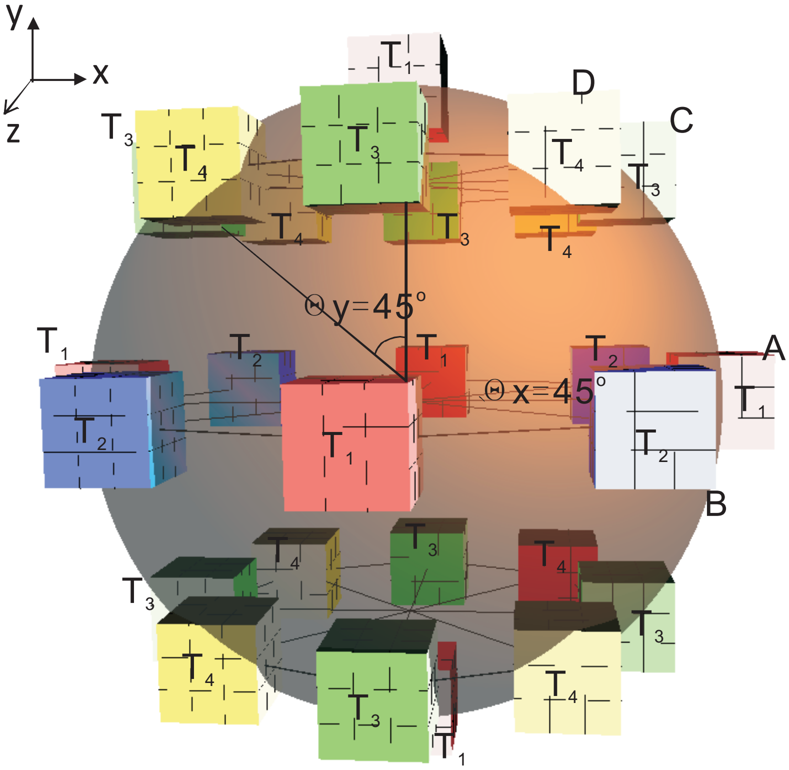

Figure 5.12: A 3D representation of the full set of prediction templates used by the proposed edge-based prediction method. The initial templates of T1, T2, T3 and T4 are at locations A, B, C and D respectively. The other templates are generated from these initial templates using rotation and translation.

Table 5.3: The specifications for the four template categories

Template category	XZ plane (θx measured from positive x-axis in the anti-clockwise direction)	Axis perpendicular to XZ plane (θy measured from positive y-axis in the anti-clockwise direction)
T1	($\theta x \leq 22.5^o$ or $\theta x \geq 337.5^o$) or ($\theta x \geq 67.5^o$ and $\theta x \leq 112.5^o$) or ($\theta x \geq 157.5^o$ and $\theta x \leq 202.5^o$) or ($\theta x \geq 247.5^o$ and $\theta x \leq 292.5^o$)	($\theta y \geq 67.5^o$ and $\theta y \leq 112.5^o$) or ($\theta y \geq 247.5^o$ and $\theta y \leq 292.5^o$)
	NA	$\theta y \leq 22.5^o$or $\theta y \geq 337.5^o$
	NA	$\theta y \geq 157.5^o$ and $\theta y \leq 202.5^o$
T2	($\theta x > 22.5^o$ and $\theta x < 67.5^o$) or ($\theta x > 112.5^o$ and $\theta x < 157.5^o$) or ($\theta x > 202.5^o$ and $\theta x < 247.5^o$) or ($\theta x > 292.5^o$ and $\theta x < 337.5^o$)	($\theta y \geq 67.5^o$ and $\theta y \leq 112.5^o$) or ($\theta y \geq 247.5^o$ and $\theta y \leq 292.5^o$)
T3	($\theta x \leq 22.5^o$ or $\theta x \geq 337.5^o$) or ($\theta x \geq 67.5^o$ and $\theta x \leq 112.5^o$) or ($\theta x \geq 157.5^o$ and $\theta x \leq 202.5^o$) or ($\theta x \geq 247.5^o$ and $\theta x \leq 292.5^o$)	($\theta y > 22.5^o$ and $\theta y < 67.5^o$) or ($\theta y > 202.5^o$ and $\theta y < 247.5^o$)
	($\theta x \leq 22.5^o$ or $\theta x \geq 337.5^o$) or ($\theta x \geq 67.5^o$ and $\theta x \leq 112.5^o$) or ($\theta x \geq 157.5^o$ and $\theta x \leq 202.5^o$) or ($\theta x \geq 247.5^o$ and $\theta x \leq 292.5^o$)	($\theta y > 112.5^o$ and $\theta y < 157.5^o$) or ($\theta y > 292.5^o$ and $\theta y < 337.5^o$)
T4	($\theta x > 22.5^o$ and $\theta x < 67.5^o$) or ($\theta x > 112.5^o$ and $\theta x < 157.5^o$) or ($\theta x > 202.5^o$ and $\theta x < 247.5^o$) or ($\theta x > 292.5^o$ and $\theta x < 337.5^o$)	($\theta y > 22.5^o$ and $\theta y < 67.5^o$) or ($\theta y > 202.5^o$ and $\theta y < 247.5^o$)
	($\theta x > 22.5^o$ and $\theta x < 67.5^o$) or ($\theta x > 112.5^o$ and $\theta x < 157.5^o$) or ($\theta x > 202.5^o$ and $\theta x < 247.5^o$) or ($\theta x > 292.5^o$ and $\theta x < 337.5^o$)	($\theta y > 112.5^o$ and $\theta y < 157.5^o$) or ($\theta y > 292.5^o$ and $\theta y < 337.5^o$)

accuracy and minimise complexity. These edge predictors are generated based on the same calculation process as described in Section 5.1.2. Consequently, the adaptive model for the edge regions is:

$$M = \{A, P\{P_{T1}, P_{T2}, P_{T3}, P_{T4}\}\} \tag{5.5}$$

where A is the specific angle and P is the corresponding predictor.

The process of edge predictor determination is implemented only once, and the coefficients for each predictor are subsequently stored in the same manner as the previous coefficients discussed in Section 5.1.2. Pre-storing these coefficients in the compressed data can significantly improve the overall efficiency of the technique.

The complete AAP model is developed by the combination of the interior-based model and the edge-based model. Once this prediction model is created, the encoding process can adaptively switch among these predictors based on the surrounding region types. The decorrelated data is then sent for entropy coding.

5.3 Experiments and results

The initial evaluation of the proposed prediction model was conducted using three randomly selected CTC data sets. These were the data sets 2, 3, and 10 (see Appendix A). The number of images per data set was 284, 289 and 259 and the resolution of each slice was 512 × 512 pixels with 12 bits per pixel.

5.3.1 Qualitative Evaluation

To estimate the efficiency of the AAP model, this model was compared with two of the best context-based prediction schemes that are currently available: MED and GAP. The 3D version of JPEG-4 proposed by Ait-Aoudia *et al.* (2006) was also used in this comparison. The residual information was compared in order to determine the performance of each prediction method.

Figure 5.13 shows the residual images produced by MED, 2D/3D GAP, 3D JPEG-4 and the proposed prediction method. It can be clearly seen that the proposed prediction method produces significantly less residual information than the other prediction approaches.

5.3.2 Quantitative Evaluation

A quantitative analysis of the prediction techniques was also carried out. This involved decorrelating the three test data sets using each of the five prediction methods. Shannon Entropy (Shannon, 1948) is used as a measurement to quantify the information remaining in a data set after decorrelation. A smaller residual entropy indicates an improved level of decorrelation performance.

The resulting entropies are presented in Table 5.4. As seen in this table, the AAP method achieves the lowest entropy with an average improvement of 15% over MED and GAP 2D and of 7% over 3D JPEG-4 and GAP 3D. It is clear from the experimental results that the predictor based on the 3D version significantly outperforms the one used in 2D cases. The improvements in performance achieved by 3D predictors can be attributed to the high level of similarity between adjacent slices in a CTC data set. The 3D predictors have the ability to exploit the inter-frame correlation to decorrelate the data set further. Additionally, the proposed prediction method is not only taking advantage of this correlation to remove the temporal redundancy but also using the segmentation technique to locally optimise the prediction value. Thus, a better result is achieved by the proposed prediction method compared to the other alternatives.

In addition, the compression technique proposed in this thesis is designed to facilitate data delivery. The data is stored persistently on the server in compressed

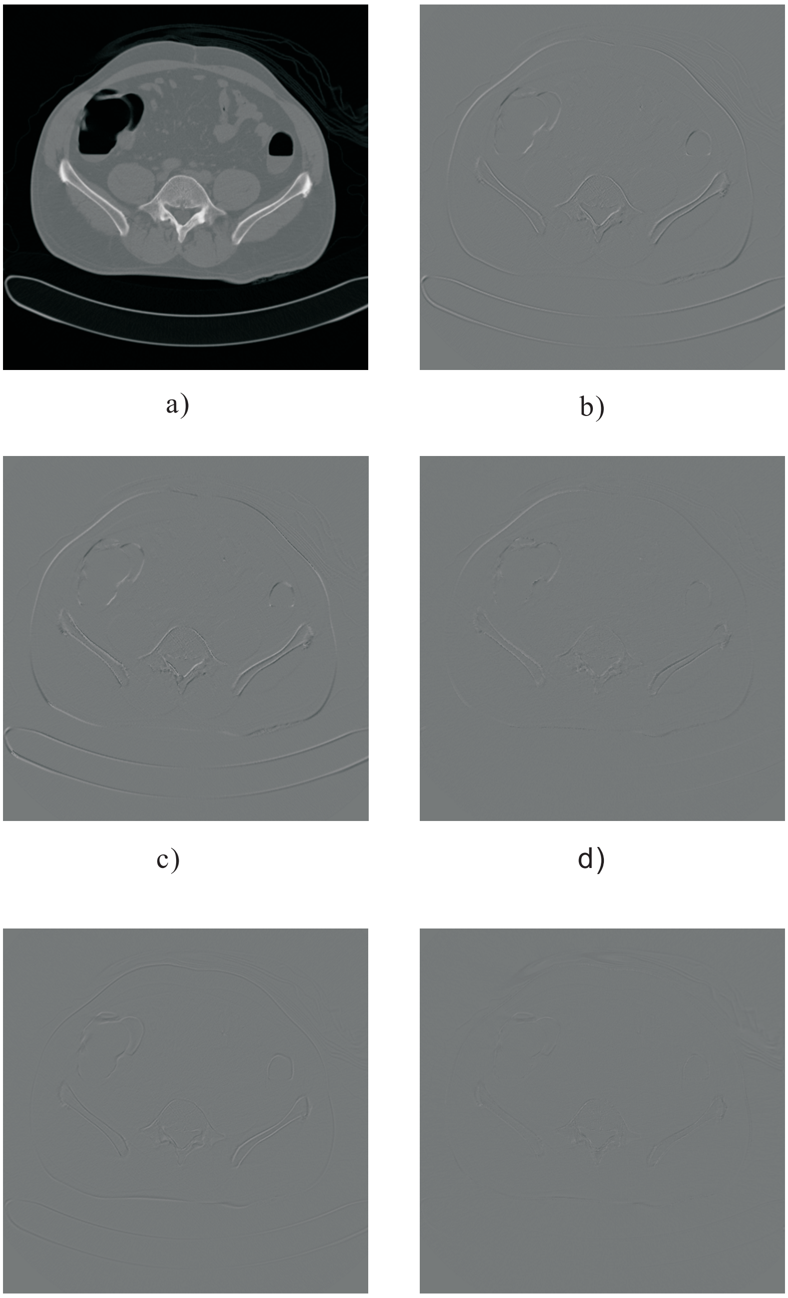

a) b) c) d) e) f)

Figure 5.13: Residue images of a CT image after different prediction methods. a) original image, b) MED, c) 2D GAP, d) 3D GAP, e) 3D JPEG-4, and f) the proposed prediction method (AAP).

Table 5.4: Entropies of prediction residuals for MED, GAP, 3D JPEG-4 and AAP models.

Data set	Entropies after prediction (bits per pixel)				
	MED	GAP 2D	3D JPEG-4	GAP 3D	AAP
2	5.89	5.86	5.36	5.35	4.85
3	6.43	6.37	5.88	5.86	5.52
10	6.47	6.47	5.97	5.94	5.56

form and has to be decompressed in a short time when the user requests to download it. Since the compression process happens once only, there is no need to be concerned with the encoding time. Based on this scenario, the proposed prediction technique is asymmetric. The encoder can be slow, but the decoder has to be fast. Most computationally intensive tasks, such as coefficient determination using the LS method, are performed in the encoding stage. All the computed results are stored as header information with the compressed data. Therefore, subsequent decoding will directly generate the predictor for each region and avoid the LS calculation. When determining the optimal template in Section 5.1.1, the larger size of template provides a higher prediction accuracy. The complexity of the prediction method was selected to give an efficient performance, which maximises accuracy and minimises complexity.

5.4 Conclusion

In this chapter, a new prediction model for medical image compression is presented. This model is developed based on two modelling approaches to deal with interior and edge regions separately. The first approach designed for interior regions is based on the identification of an optimum template to generate an efficient predictor. This predictor can achieve high prediction accuracy at a relatively low computational cost. The second approach dealing with edge regions considers different edge directions. It rotates the prediction template to ensure a consistent input pattern in the prediction model. This pattern makes the generation of an optimised edge-based predictor feasible. The proposed prediction model contains these two types of predictors and adaptively switches to the optimal predictor according to the characteristics of the region being compressed. In order to illustrate the validity of this prediction model, its decorrelation performance was compared with current state-of-the-art prediction methods. The numerical results indicate that the proposed prediction model significantly outperforms the set of alternatives that are currently available and is able to return consistent decorrelated results when applied to medical image data. The next chapter discusses the combination of the proposed prediction model and an efficient entropy coding technique to yield a complete compression scheme optimised for use with abdominal CT data.

Chapter 6

Delivery Scheme Implementation and Evaluation

One of the major contributions of this thesis is a novel compression scheme that uses prior knowledge of anatomical information to improve the performance of medical image compression. This scheme consists of an anatomy-based segmentation process, an adaptive prediction model and an entropy coder. An outline of the complete compression scheme (ALMIC) in terms of its encoding and decoding stages is illustrated in Figure 6.1. During the encoding stage, the original data set is initially segmented into different anatomical regions and an optimised predictor is subsequently generated for each region. The AAP model uses a series of optimised predictors to decorrelate the data. The residual data is then sent for entropy coding. The decoding process is the opposite of the encoding process. However, due to the fact that the coefficients for each predictor have been stored in the header within the compressed data, the prediction model can be generated without significant computational cost. According to the type of the region associated with the current pixel, the decoder switches to the corresponding predictor to generate the predictive value. This value is added to the stored prediction error to reconstruct the original data. The anatomy-based segmentation and the adaptive prediction model are described in Chapters 4 and 5 respectively. This chapter deals with the entropy coding component, with the aim of identifying an efficient entropy coding technique to ultimately compress the residual data. Once the complete compression scheme is generated, this technique is subsequently used to develop an optimum solution for medical data delivery via the Internet. An evaluation of both the compression and the delivery schemes is conducted on 20 CTC data sets.

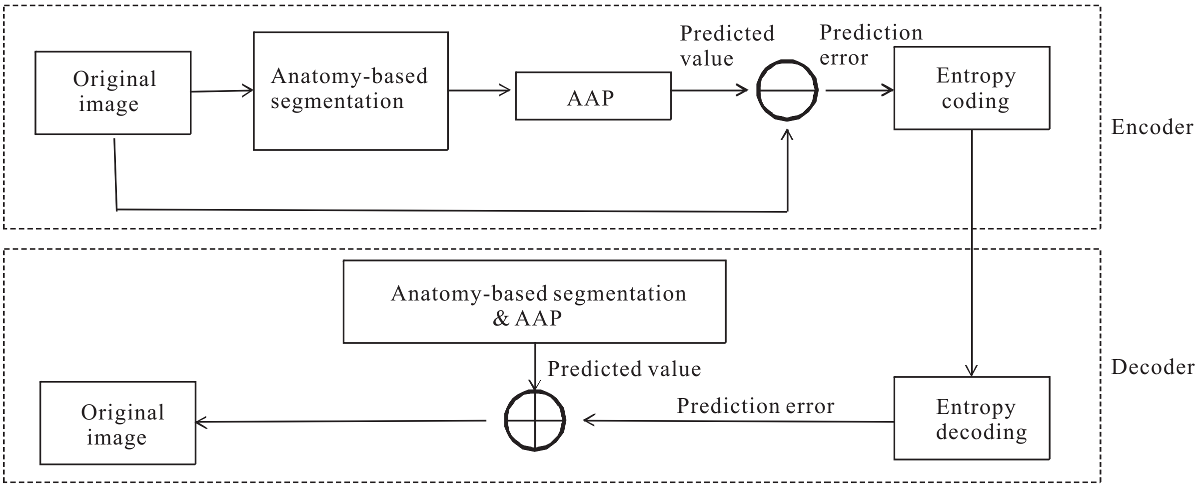

Figure 6.1: The encoding and decoding processes of the ALMIC technique.

6.1 Lossless Compression Performance

Lossless compression is characterised by a reversible process where the decompressed data is numerically identical to the original data. This type of technique is preferred in the case of medical image compression due to the fact that the loss of any diagnostic information in an image may lead to serious consequences, such as misdiagnosis. Consequently, this section focuses on the evaluation of the lossless performance of the proposed compression method.

6.1.1 Data Description

The data sets used in this study were divided into two subsets: training data sets and blind test data sets. The parameters for anatomical region segmentation and the optimised template strategies for each anatomical region were identified from the training data sets. In the final evaluation, the experiments were only conducted on the test data sets in order to determine the true performance of the compression scheme. Twenty CTC data sets were included in the test set. The details of these data sets are provided in Appendix A.

6.1.2 Lossless Entropy Coding

The final stage of the compression scheme is to encode the residual data using an entropy coder. With regard to entropy coding, the most representative lossless compression techniques are Huffman coding (Huffman, 1952), Lempel-Ziv-77 (LZ77) (Lempel & Ziv, 1977) and Prediction with Partial Matching (PPM) (Cleary & Witten, 1984). In this experiment, all of the above techniques were evaluated using third-party implementation [1] [2] [3]. The compression results using these entropy coding techniques on the test data sets are shown in Table 6.1. Note: The compression ratio = the original size / the size of the data set after compression.

It is clear from this table that the performance of the PPM method is better than the other three techniques in terms of the compression ratio achieved. This achievement is mainly due to its use of an adaptive context model. The basic

---

[1] Huffman coding `http://www.codeproject.com/`

[2] LZ77 `http://www.7-zip.org/`

[3] PPM `http://www.chilkatsoft.com/compression-java.asp`

Table 6.1: Compression ratio for each lossless compression method.

Data set	Huffman coding	LZMA	PPMd
1	1.45	2.22	2.43
2	1.42	2.17	2.38
3	1.43	2.31	2.59
4	1.43	2.15	2.34
5	1.48	2.21	2.40
6	1.44	2.17	2.37
7	1.47	2.31	2.57
8	1.41	2.14	2.36
9	1.41	2.22	2.48
10	1.44	2.31	2.61
11	1.42	2.19	2.43
12	1.45	2.32	2.60
13	1.39	2.12	2.34
14	1.47	2.29	2.56
15	1.45	2.21	2.43
16	1.46	2.23	2.46
17	1.44	2.23	2.46
18	1.40	2.15	2.37
19	1.44	2.31	2.60
20	1.39	2.18	2.43

principle of statistical data compression is that frequently occurring values are replaced by a short code and less frequently occurring values are replaced with a longer code. The general statistical data compression techniques, such as Huffman coding, are based on a global distribution of probabilities for the input symbols. The PPM technique assigns the probability of the current symbol based on the previous context. The current symbol may have a high probability in a specific context, but a low probability in the global distribution. Consequently, a shorter code can be assigned to the current symbol using the PPM compression technique, thus this technique improves the level of compression.

Based on this experimental result, the PPM technique is chosen for use as the entropy coder in the ALMIC scheme. This is motivated by the fact that this technique can achieve the highest compression ratio and as a result it can maximise the entire compression performance.

6.1.3 Complete Lossless Performance

In order to illustrate the validity of the whole compression scheme, including the data decorrelation and entropy coding stages, the compression results provided by the proposed scheme were compared with those obtained by a number of alternative techniques, e.g. JPEG2000 and 3D-JPEG2000. The compression results yielded by JPEG2000 and 3D-JPEG2000 techniques were obtained losslessly with three levels of decomposition. The Kakadu JPEG2000 software development kit[1] was used to implement the two compression techniques. The compression results obtained by the proposed compression scheme and alternative techniques are presented in Table 6.2.

The results reported in this table show that the proposed method achieves the highest compression ratio on all of the tested data sets with an average im-

---

[1] `http://www.kakadusoftware.com/`

Table 6.2: Lossless compression results using various compression methods.

Data set	Compression method			
	JPEG2000	3D-JPEG2000	3D JPEG4+PPMd	AAP +PPMd
	Compression ratio (bits per pixel)			
1	2.59 (6.18 bpp)	2.60 (6.16 bpp)	2.78 (5.76 bpp)	2.94 (5.43 bpp)
2	2.54 (6.30 bpp)	2.55 (6.28 bpp)	2.72 (5.89 bpp)	2.88 (5.55 bpp)
3	2.88 (5.55 bpp)	2.90 (5.52 bpp)	3.14 (5.09 bpp)	3.32 (4.82 bpp)
4	2.50 (6.39 bpp)	2.52 (6.35 bpp)	2.67 (6.00 bpp)	2.83 (5.65 bpp)
5	2.71 (5.90 bpp)	2.73 (5.85 bpp)	2.92 (5.48 bpp)	3.11 (5.15 bpp)
6	2.55 (6.27 bpp)	2.56 (6.24 bpp)	2.76 (5.79 bpp)	2.89 (5.53 bpp)
7	2.96 (5.40 bpp)	2.97 (5.39 bpp)	3.17 (5.05 bpp)	3.39 (4.72 bpp)
8	2.75 (5.82 bpp)	2.76 (5.79 bpp)	2.98 (5.38 bpp)	3.17 (5.05 bpp)
9	2.45 (6.52 bpp)	2.47 (6.49 bpp)	2.60 (6.16 bpp)	2.76 (5.80 bpp)
10	2.48 (6.44 bpp)	2.50 (6.41 bpp)	2.71 (5.90 bpp)	2.76 (5.80 bpp)
11	2.74 (5.85 bpp)	2.74 (5.84 bpp)	2.95 (5.43 bpp)	3.13 (5.12 bpp)
12	3.00 (5.34 bpp)	3.01 (5.31 bpp)	3.25 (4.93 bpp)	3.48 (4.60 bpp)
13	2.58 (6.21 bpp)	2.59 (6.18 bpp)	2.79 (5.73 bpp)	2.94 (5.45 bpp)
14	2.79 (5.74 bpp)	2.80 (5.72 bpp)	3.00 (5.33 bpp)	3.19 (5.03 bpp)
15	2.63 (6.07 bpp)	2.65 (6.05 bpp)	2.83 (5.65 bpp)	3.00 (5.34 bpp)
16	2.66 (6.02 bpp)	2.67 (6.00 bpp)	2.86 (5.60 bpp)	3.03 (5.29 bpp)
17	2.62 (6.10 bpp)	2.64 (6.07 bpp)	2.83 (5.65 bpp)	2.98 (5.38 bpp)
18	2.59 (6.18 bpp)	2.60 (6.15 bpp)	2.78 (5.76 bpp)	2.97 (5.40 bpp)
19	2.96 (5.40 bpp)	2.98 (5.37 bpp)	3.23 (4.95 bpp)	3.44 (4.66 bpp)
20	2.77 (5.77 bpp)	2.79 (5.72 bpp)	3.00 (5.33 bpp)	3.19 (5.03 bpp)

provement of 12% over JPEG2000 and 3D-JPEG2000, and 6% over the standard 3D-JPEG4+PPMd method. Even though the 3D-JPEG2000 and the 3D-JPEG4+PPMd methods exploit the correlation between slices, they cannot compress edge regions efficiently. These techniques perform poorly in the case of medical images due to the fact that a high number of edges are present.

The proposed compression scheme incorporates a novel edge-based prediction method to deal specifically with the PVE regions in the medical image data sets. This predictor has been shown to be quite effective in reducing the amount of residual information associated with edges (Min & Sadleir, 2012). The remaining regions are decorrelated by a series of optimised predictors. Facilitated by the proposed prediction model, PPMd achieves a better compression performance in comparison to alternative techniques that were tested in the experiment.

6.2 Delivery Scheme

This section evaluates the proposed compression method used in the remote access CTC scenario. To achieve this, the compression method has been incorporated into a CTC data delivery scheme. There are two issues which need to be considered with regard to efficient delivery over the Internet: one is download time, another is decompression time. In order to reduce download time, the data set must be compressed. The compressed data set is stored permanently on the server and, since the compression process happens only once, it is not necessary to be concerned about the compression time. However, the decompression time is important in a delivery scheme due to the fact that a long decompression stage will negate the benefits of compression. The proposed compression method is developed based on a compromise between compression ratio and coding efficiency. Therefore, it should be feasible for use in a delivery scheme. In order to test this hypothesis, a series of experiments were carried out to determine the performance of the proposed compression method when used to facilitate data delivery.

6.2.1 Experimental Environment

The experimental environment is shown in Figure 6.2, and consists of: a server, a client and an IEEE 802.11g router. A Belkin N Wireless Router is used to provide the local network. The maximum network data transfer rate provided by this router is 300 Mbps. This rate is sufficient for the experiments that are carried out. The details of the machines used in the experiment are shown in Table 6.3.

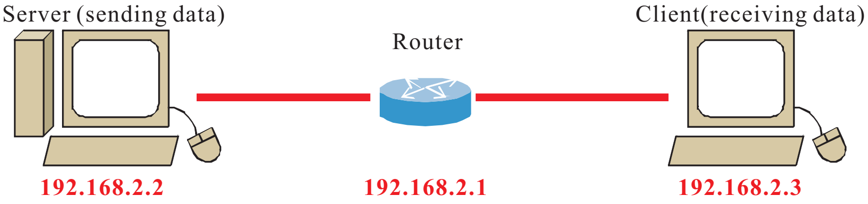

Figure 6.2: Overview of the experimental testbed for modelling the network environment.

Table 6.3: The details of equipment used in the experiments.

Client	CPU	Intel(R) Core(TM)2 Quad Q6600 @ 2.40GHz 2.39 GHz
	Memory	3.00 GB
	Operating System	Windows Vista 32-bit
Server	CPU	Intel(R) Core(TM) i3 CPU @ 2.27GHz 2.27GHz
	Memory	2.00 GB
	Operating System	Windows 7 32-bit
Router	Brand	Belkin
	Model	F5D8233-4v3
	Network Data Transfer Rate	300 Megabits per Second (Mbps)

6.2.2 Description of the Experiment

All the programs in this experiment were written using Java with the exception of the implementation of the PPMd algorithm which was written in C. The server program is responsible for sending data at a certain rate and the client program is used to download and decompress the data set. The downloading and decompression processes are implemented in parallel on the client side in order to provide an optimised solution for data delivery. A Java applet is used as the Web-based client application in this experiment as it has the required level of accessibility, functionality and connectivity. In addition, in order to observe the performance of the proposed delivery scheme at a certain connection rate, a bandwidth monitor was installed on the client computer to measure the simulated connection speed between the server and the client programs. According to the reported connection speed, the server updated the sending rate in order to simulate different network connections. Therefore, a quantitative evaluation of the delivery scheme when used in conjunction with a range of connection speeds can be achieved.

6.2.3 Experiments and Results

Figure 6.3 depicts the performance of two data delivery schemes. One is the proposed delivery scheme that transmits the precompressed data set. The other is the general delivery scheme that transmits the uncompressed data set. These schemes were tested using different connection speeds ranging from 1 Mbps to 48 Mbps.

As shown in Figure 6.3, the delivery time for transmitting the data set to the client is mainly influenced by the connection speed. It is evident that the delivery of compressed data is much faster than delivering uncompressed data at most connection speeds. In the region between the dotted vertical lines which represents typical connection speeds in Ireland, the proposed scheme can reduce

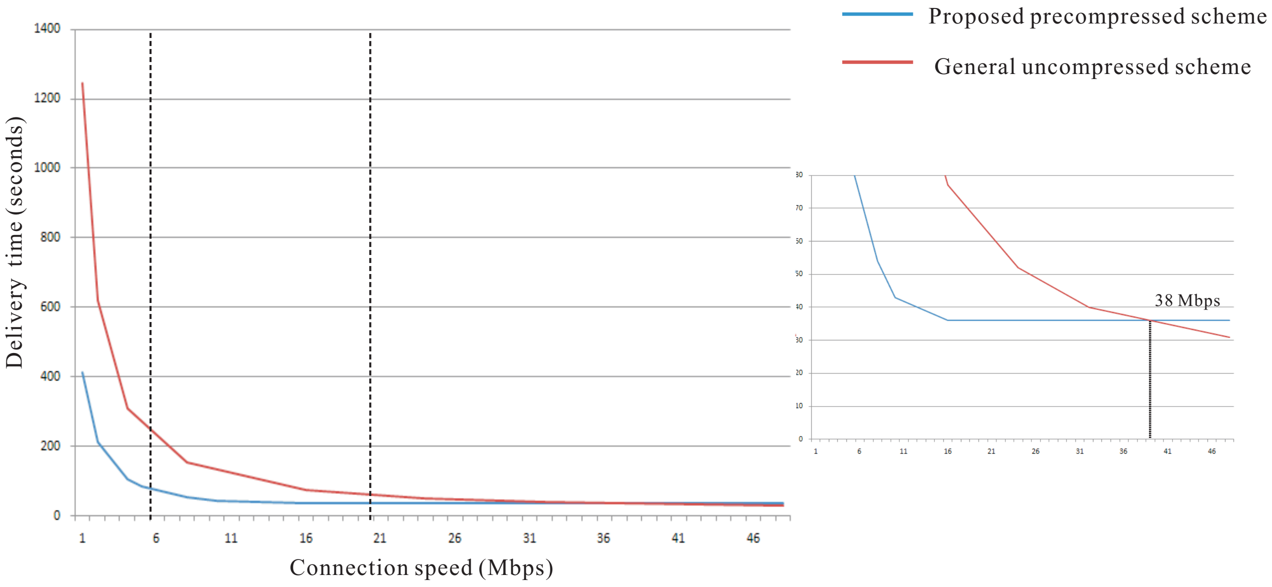

Figure 6.3: Performance of the delivery time for data set 1 over a range of different connection speeds.

delivery time by more than half of the original download time. As the connection speed increases, the benefit associated with using the proposed technique is reduced. The explanation of these results is that increasing the connection speed can reduce the download time, but the decompression time is constant. In the current implementation, the decompression time is 33 seconds for data set 1 and the download time for the uncompressed data set is less than 33 seconds when the connection speed is above 38 Mbps. In this case, the proposed delivery scheme is not valid as the decompression time is longer than the transmission time of the uncompressed data set.

However, it should be noted that the current implementation of the proposed technique is based on a low-cost PC platform. With an improvement in the hardware, the decompression time will be reduced, thus the proposed technique will be valid for even higher connection speeds.

In addition, according to a report by IrelandOffline [1], the typical download speed currently available in Ireland is 8.32 Mbps. As can be seen in Figure 6.3, the proposed scheme reduces the delivery time by nearly two thirds when compared with the original download time at this speed. These results indicate that the proposed technique provides a significant improvement over uncompressed delivery for the transmission of medical image data over the Internet, thus confirming that the previous hypothesis is true.

It should be noted that the experiments were carried out in a simulated environment where a router connects a client and a server to create a lossless communication network. Real-world networks are much more complicated and they introduce delays and errors due to the round-trip time across the network (latency), packet loss, and jitter (Lundgren, 2002). However, this thesis focuses on compression, and the experimental results tested on the simple network demonstrate that the proposed compression technique can reduce transmission time, thus confirming its validity.

6.3 Discussion

The delivery scheme, developed based on the proposed compression technique, has been proven to be efficient in the transmission of CTC data sets. However, there is scope for further improvement of this scheme by optimising the template size based on the transmission speed and by using scalable compression.

6.3.1 Template Optimisation

A shorter delivery time can be achieved by optimising the template size. The current template sizes for each region are visually selected in Chapter 5. This

---

[1] `http://irelandoffline.org/2012/06/quarterly-report-q2-2012/`

selection is based on a compromise between the compression efficiency and the decompression speed. Consequently, the proposed compression method can achieve a high compression ratio as well as a short decompression time. In order to maximise the benefit of this compression method in the delivery scheme, the factor of the transmission rate should also be considered. This is due to the fact that the delivery scheme is most efficient when the decompression rate equals the transmission rate. The validation of this argument is provided below. Based on the current implementation, the decompression rate is 11.92 Mbps. In the case of the typical transmission rate in Ireland (8.32 Mbps), the decompression rate is higher than the transmission rate, which means the final delivery time is determined by the download time. Thus, it is possible to increase the template size to obtain further compression gains, which, in turn, leads to a shorter download time. When the decompression rate approaches the same level as the current transmission rate, the delivery scheme reaches optimum performance at that transmission rate. If the decompression rate reduces further, the decompression time will be longer than the transmission time, which negates the benefits of a short transmission time. Therefore, optimum delivery performance is achieved when the decompression rate equals the transmission rate. It should be noted that the decompression rate is mainly determined by the template size: the larger the template size, the lower the decompression rate. Consequently, the template size should be adaptively changed according to the transmission rate so as to achieve optimal delivery performance. In order to deduce the optimum template sizes for a range of transmission rates, a quantitative evaluation of the delivery time yielded by the proposed scheme in conjunction with different template sizes has been carried out.

Table 6.4 describes the delivery performance in the case of different template sizes. Three cases are evaluated. The first case uses the template size of 5 (low compression ratio, but fast decompression speed). The second case applies the current version of the template used for compression. The third case uses the template size of 13 (high compression ratio, but low decompression speed). As shown in the Table, the larger template size generates a higher compression ratio. However, it is clear that the high compression ratio does not provide a short delivery time, due to the fact that a high compression ratio usually indicates high computational complexity. This high complexity leads to a long decompression stage, which significantly degrades the delivery performance at a high transmission rate. This can be seen in case 3, the outcome of which is poor performance at a high transmission rate. In addition, due to the tested transmission rates being higher than or equal to the decompression rate, case 3 has a constant delivery time, which equals the decompression time. On the other hand, although case 1 produces the lowest compression ratio among the three cases, it still achieves the shortest delivery time in the case of a high connection speed. This experimental data confirms that use of the optimised template can improve the delivery performance of the proposed scheme. Therefore, a further reduction of the delivery time can be achieved by adaptively changing the size of template.

6.3.2 Scalable Compression

The evaluation of the scalable compression of the proposed method is based on a recent study by Kim *et al.* (2011). The study has demonstrated that an improvement in the compressibility of medical image data could be achieved by removal of the area outside the body. This functionality can be incorporated into the proposed technique in order to improve the achievable level of compression. Figure 6.4 presents the compression results for both cases i.e. with and without the detail outside the patient.

It is evident that the application of this enhanced version of the proposed

Table 6.4: The delivery performance achieved using different template sizes.

Case	Template size				Image data after compression (compression ratio)	Decompression rate / optimum transmission rate	Transmission time		
	Soft tissue	Adipose tissue	Air	Bone			using optimum transmission speed in case 1	using optimum transmission speed in case 2	using optimum transmission speed in case 3
1	5	5	5	5	51,403 KB (2.88)	14.34 Mbps	**32.27s**	36.29s	49.92s
2	9	9	9	11	50,361 KB (2.94)	11.92 Mbps	35.80s	**35.95s**	49.38s
3	13	13	13	13	50,302 KB (2.94)	8.73 Mbps	49.35s	49.35s	**49.35s**

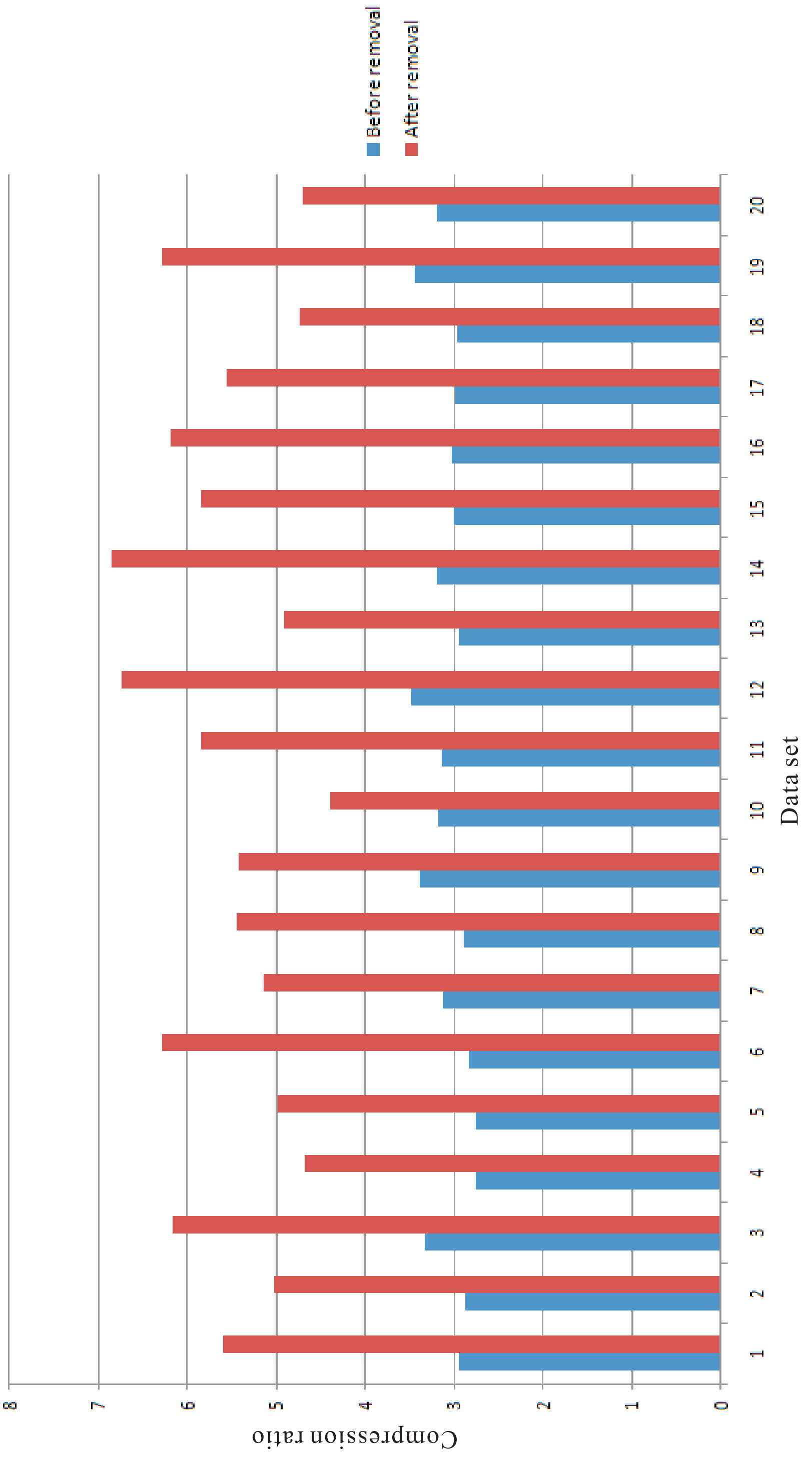

Figure 6.4: The image compression ratio before and after removing the area outside the body.

method can significantly improve compression results and achieve an average improvement of 85% over methods which retain the area outside the body. However, this improvement is only achievable when it is acceptable to discard the data outside of the patient. In the CTC training scenario, it is important to retain all the information in the images. This is due to the fact that some novices are not familiar with CT images. The additional information, such as the scanning table, can provide trainees with an indication of the position of the patient in the CT images. This makes it easier for trainees to understand the anatomical relationships in sagittal, axial and coronal planes. This observation is supported by the Royal Australian and New Zealand College of Radiologists that all the information in the CT images should be provided during CTC training (RANZCR, 2012).

However, this enhanced version of the proposed method may be applicable in clinical scenarios due to the fact that radiologists proficient in CTC are sufficiently familiar with the anatomical structure on CT images. Therefore, the removal of data that is not of diagnostic significance is acceptable. The removal of the information outside the patient offers a further improvement in the transmission capacity of the proposed scheme. For example, if transmitting a 200 MB CTC data set at the typical network speed in Ireland, the delivery times using the uncompressed method, the optimised version of the proposed scheme and the enhanced version of the proposed scheme which includes scalable compression are 142 seconds, 56 seconds and 35 seconds respectively. It is clear that this enhanced version of the proposed method significantly improves the delivery performance by reducing the original download time by nearly 75%, and the optimised delivery time by 40%. More importantly, this level of performance has been achieved without compromising the patient data.

6.3.3 Transmission Optimisation

Progressive image transmission (PIT) is a potential technique to accelerate the data delivery process. It initially sends a coarse version of the original image and then refines the initial image by increasing the level of detail progressively. This approach can help to reduce the latency when transmitting a large amount of image data via a low speed connection. In order to apply this technique in the proposed method, the predictive error needs to be quantified into different levels. This would allow the most significant errors to be quickly transmitted to the client for fast reconstruction of a rough approximation of the image. More image details could then be obtained by subsequent transmission of less significant errors and the original image could ultimately be reconstructed if all of the data is transmitted to the client.

Although this technique is attractive, it cannot work in the training scenario. As discussed in Chapter 1, the whole data set must be completely downloaded to the client in order to provide a short response time for client-side operations and to facilitate the recording of the training time for each session. Therefore, the CTC interpretation will not be started until all the CTC data has been downloaded and in this case, progressive image transmission cannot help to reduce the delivery time.

6.4 Conclusion

In this chapter, a novel lossless 3D compression scheme (ALMIC) which combines an adaptive prediction model and an efficient entropy coding technique is presented. The main emphasis of this chapter was placed on the performance evaluation of the ALMIC scheme. To achieve this, the ALMIC scheme has been tested with 20 blind CTC data sets. The experimental data indicates that the

ALMIC scheme significantly outperforms the standard image compression techniques with an average improvement of 12% over JPEG2000 and 3D JPEG2000. Based on this result, it is expected that similar levels of compression can be achieved by applying ALMIC to medical images associated with other areas of the human body.

Another objective of this chapter was to integrate the ALMIC method into a delivery scheme in order to achieve a short transmission time. The validity of the proposed delivery scheme is illustrated by comparing the delivery of an uncompressed data set and precompressed data set using a range of connection speeds. The numerical results indicate that the proposed delivery scheme reduces the delivery time by nearly two thirds in the case of the typical connection speed in Ireland, thus confirming the feasibility of the technique when applied to the remote access CTC scenario.

Some potential still exists for further improvements in the current version of the delivery scheme, which can be achieved by adaptively changing the template size in response to the connection speed and removal of the information outside the patient (if acceptable). Integration of these improvements into the existing scheme permits an even higher transmission speed for CTC data set delivery.

Chapter 7

System integration

The main aim of this thesis is to develop a framework for remote access CTC training in order to provide a straightforward and cost-effective training experience. Two challenges associated with the development of this framework have been addressed using an improved volume rendering technique and a novel lossless compression approach. Integration of the developed volume rendering technique and compression approach into the framework can significantly minimise the latency times for data visualisation and data delivery.

The purpose of this chapter is to discuss the whole framework for remote access CTC training in terms of functionality and feasibility. The details of each integrated component are described and an initial implementation of the framework is also presented.

7.1 The Proposed Framework for Remote Access CTC Training

As previously outlined in Chapter 1, there are two requirements for providing adequate CTC training, namely a simulated clinical environment and training feedback. The proposed framework for remote access CTC training, which is presented in Figure 7.1, attempts to satisfy both of these requirements. This framework mainly focuses on the client-side components, i.e. data connection, image analysis/interpretation functionality and training feedback.

7.1.1 Data Connection

When launching the CTC training system, the first task is to download the relevant data set to the client. As shown in Chapter 6, an efficient data delivery scheme has been developed based on the ALMIC approach which is designed for fast decompression. However, as compression may be time-consuming, all the data sets are precompressed and stored on the server. Once a client makes a request to download a data set, the compressed version of the data set is transmitted to the client. The downloading and decompression are performed in parallel in order to optimise the delivery procedure. The experimental results presented in Chapter 6 indicate that the proposed delivery scheme significantly reduces transmission time in the case of a very slow connection.

7.1.2 Functionality Provided by the Framework

Once the download and decompression are complete, the first slice in the data set is automatically displayed on the screen. The user can then use 2D and 3D tools to assist in the interpretation and analysis of the downloaded data set.

The essential 2D interpretation functions include windowing and magnification. Windowing is a useful tool for the enhanced visualisation of particular anatomical structures in the image. A specific range of object densities can be viewed with a window centre and a window width. Another post-processing function, image magnification, can be used to see the fine detail in the image.

Both surface rendering and volume rendering are incorporated in the proposed

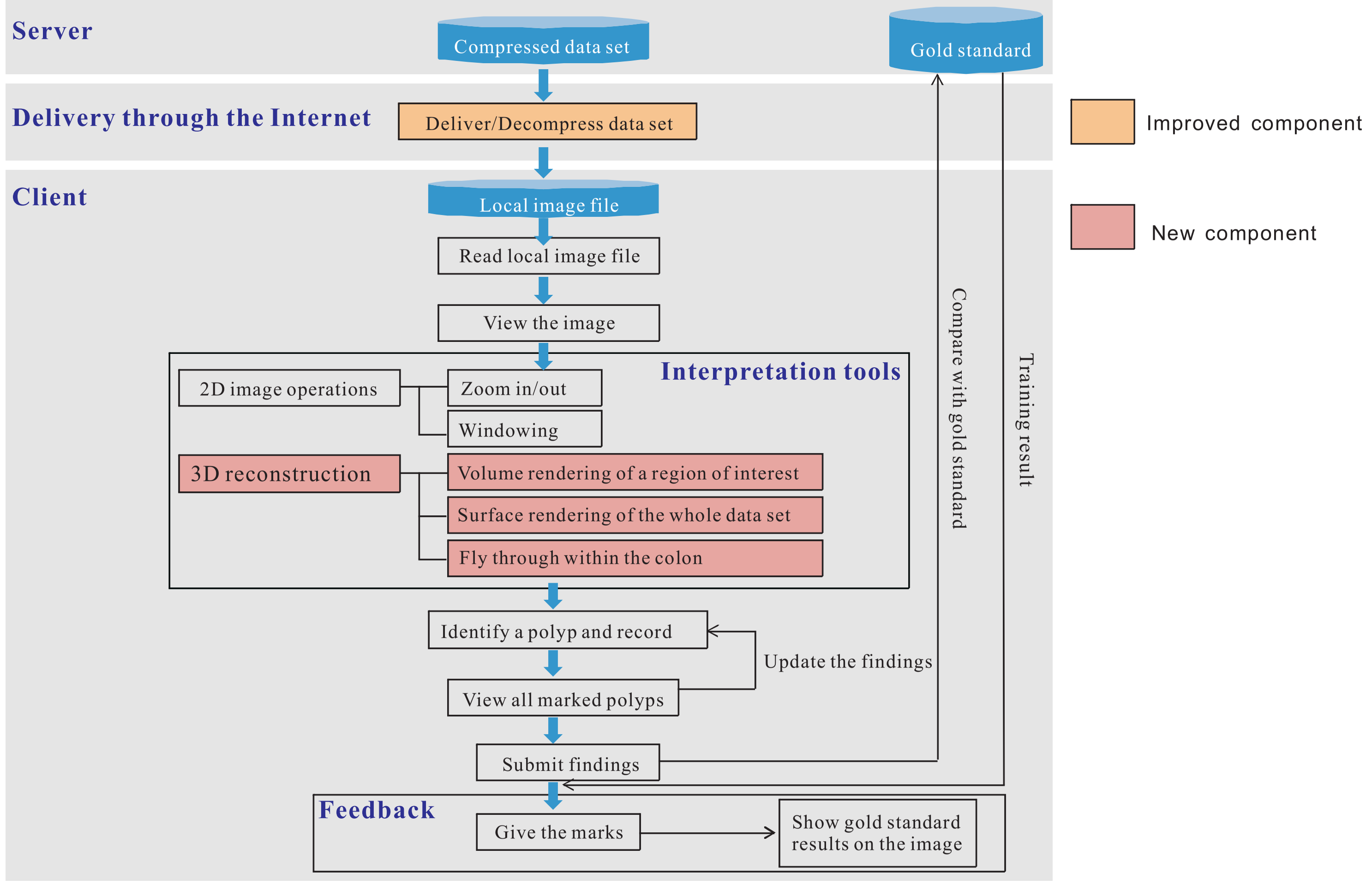

Figure 7.1: An outline of the proposed online framework for CTC training.

framework for 3D visualisation of the colonic surface. Surface rendering can be used as a primary 3D interpretation tool to detect potential abnormalities, and a further study of the detected abnormalities can be carried out using volume rendering. The combination of these two 3D functions can provide some additional information which has the potential to increase the diagnostic accuracy of CTC. In the case of surface rendering, the extraction of the isosurface from a volumetric data set is performed using a modified version of the Marching cubes algorithm (Lorensen & Cline, 1987), and this process is implemented once only. Subsequently, the information pertaining to the vertices and the normals are stored on the server. Therefore, the client only needs to generate a 3D model according to the existing vertices and normals, instead of implementing the whole 3D reconstruction algorithm. Consequently, a fast visualisation of the whole colon can be achieved using the surface rendering technique. A useful interpretation tool, virtual fly-through, is implemented based on this rendering technique. It allows the camera to move along a predefined path within the colon. This path is commonly referred to as the colon centreline. The trainee can easily observe the inner wall of the colon with the sequential movement of the camera. This function can facilitate the detection of potential abnormalities. Once the potential abnormalities are detected, a further study of the tissues beneath the colon wall can be achieved using volume rendering. This technique can help trainees to distinguish between benign and malignant lesions based on the volumetric information. However, one of the main disadvantages of this technique resides in its high computational complexity. This problem is addressed by the efficient volume rendering technique which is presented in Chapter 3. Inclusion of this technique in the complete framework facilitates real-time rendering performance on a low-cost PC platform.

7.1.3 Feedback

One of the important components of this framework is feedback provision. This feedback aims to help trainees to avoid repeating the same mistakes and improve sensitivity in subsequent training sessions. Hodder *et al.* (1989) demonstrate that immediate and specific feedback can improve learning outcomes for medical students. Consequently, the developed training system is designed to support this feedback strategy. During the training process, the trainee is initially blinded to the training case and performs an interpretation using 2D/3D tools. Once the interpretation of a particular CTC data set has been completed, the findings are sent to the server. These findings are automatically evaluated based on the relevant gold standard and feedback for this session is immediately sent back to the trainee. In order to provide specific feedback, some explanations on false-negative or false-positive polyps and the teaching points associated with the case will be ultimately displayed on the client side. This specific feedback and remedial instruction make the training more effective (Rolfe & Sanson-Fisher, 2002). This proposed training strategy corresponds to the suggestion by most CTC experts as discussed in Chapter 1.

7.2 Implementation

The initial implementation of the proposed framework for the remote access CTC training system was achieved using Java. A Java applet is used as the client application. This is motivated by the fact that, using this application, the system can be distributed via the Internet and deployed across a range of different platforms, thereby providing a high level of usability. Each of the components that make up the proposed framework are presented in Appendix B.

This system has been evaluated by a person familiar with CTC. This person confirmed that the navigation, magnification and windowing functionalities were equivalent to that on a clinical workstation. The only feature that was different to clinical software was the custom volume rendering technique. This technique was fully evaluated in Chapter 3 and the result of this evaluation shows that the proposed volume rendering technique can achieve a level of polyp detection sensitivity comparable to that achieved using the VTK. Thus, it can be concluded that the developed system is capable of providing all necessary functionalities in terms of CTC interpretation and its performance is comparable to the industry standard. Combining these interpretation tools with feedback provision results in a remote access CTC training system that is comparable to the CTC software used in a clinical environment.

7.3 Conclusion

This chapter presents an integrated framework for remote access CTC training and demonstrates its feasibility for providing such training. The framework incorporates an efficient data delivery scheme to reduce the time required for data transmission significantly. Thus, the training is more efficient due to the fact that the trainee does not have to wait for a long time to receive the data. The framework also provides a range of 2D/3D features to facilitate image interpretation. One of the most important features is volume rendering. This feature allows the trainee to further analyse the detected abnormalities, which has the potential for increasing diagnostic accuracy and reducing the number of false positives. The final phase of training is to provide feedback related to the trainees's performance. This information has the potential to make the training more efficient and effective.

Based on the initial implementation using Java, it can be concluded that the proposed framework is capable of providing CTC training in a remotely-accessible fashion. This training system has a short delivery time and comprehensive 3D visualisation features and more importantly, it is able to achieve a high level of performance even in the case of low-cost PC platforms with low-speed data connections.

Chapter 8

Conclusions and Future Work

The aim of this research has been to develop a new framework to facilitate remote access CTC training. The motivation for this research is derived from the fact that current insufficient training resources and a shortage of CTC experts significantly restrict the clinical use of CTC. A remote access CTC training system would offer a promising solution to this issue. Such a system could provide remote access to the training material as well as automatic evaluation of reader performance. Utilisation of such a training system would greatly reduce the difficulties associated with CTC accreditation.

In order to provide CTC training in a remotely-accessible fashion, two challenges have to be addressed: the implementation of fast software-based volume rendering and the development of an efficient data delivery scheme. The research presented in this thesis has led to novel approaches to tackle these issues.

The first challenge is addressed by the development of a new volume rendering technique. Due to the intensive computation involved, volume rendering algorithms can be extremely slow; a lot of previous work has been directed toward using hardware acceleration techniques to improve the efficiency of volume rendering. Clearly, the hardware-based acceleration techniques are not applicable in the case of a standard PC platform. Chapter 3 presents a purely software-based approach in order to increase accessibility to volume rendering. Experimental results confirm that real-time volume rendering can be achieved on a low-cost PC platform using the proposed technique.

The challenge associated with data delivery is addressed by a novel anatomy-based lossless medical image compression technique (referred to as ALMIC). As indicated in the literature review detailed in Chapter 2, most of the existing image compression methods are designed for use with natural images. In the vast majority of the cases, the characteristics of medical images have not been used to improve the level of compression that can be achieved. The proposed technique utilises anatomical features to provide better medical image compression performance. The experimental results indicate that the proposed technique significantly outperforms general purpose methods that are designed for natural image compression. An optimum solution for medical image data delivery is subsequently developed based on the ALMIC approach. The proposed delivery scheme can greatly reduce the transmission time particularly in the case of a low connection speed. Thus, a shorter delivery time is achievable using the proposed scheme.

Addressing these challenges has led to a number of research contributions. These contributions are summarised in Section 8.1 and potential future research directions are outlined in Section 8.2.

8.1 Research Contributions

This thesis deals with two challenges related to remote access CTC. For each challenge, a novel solution is proposed, evaluated through real experimentation, and then validated by the results from these experiments. Major and minor contributions of this research are summarised in the following sections.

8.1.1 Major Contributions

- **Real-time software-based volume rendering**

The first major contribution of this research is the development of a real-time software-based volume rendering technique. In order to improve rendering efficiency, a series of acceleration techniques are proposed, such as rendering with a subvolume and optimised trilinear interpolation. The proposed volume rendering technique incorporates these acceleration methods to improve the performance of the rendering process. Results show conclusively that the proposed volume rendering technique can achieve real-time performance on a low-cost PC platform.

The quality of the rendering results generated by the proposed technique has been verified by visualising a large range of polyp sizes. Even small polyps can be easily seen in the rendered images, thus confirming the diagnostic validity of the proposed technique. Other air-filled body parts, such as the lungs and the stomach, have similar characteristics to the colon. Therefore, use of the proposed technique is feasible in these scenarios and, in each case, it should be possible to visualise the data on a low-cost PC platform.

- **Anatomy-based lossless medical image compression**

The second major contribution of this research is the development of an anatomy-based lossless medical image compression method. The novelty of this technique consists of a ‘divide and conquer’ approach to divide the original medical data set into specific anatomical regions which are then compressed separately. Therefore, the first task of this technique is to automatically identify each region in the CTC data set. Identification of the specific anatomical regions is a complex task since the density characteristics of these organs are similar and consequently a simple density-based segmentation method is not adequate. To tackle this problem, anatomical features are employed to guide the segmentation process in order to improve segmentation accuracy. A tailored version of this segmentation method is then developed for use in the preprocessing stage of the compression technique. Based on the segmentation result, a series of predictors optimised for each anatomical region can be generated. The combination of this prediction model and an efficient entropy coding technique ultimately creates the ALMIC scheme. The experimental results indicate that the proposed technique can provide an average improvement of 12% over JPEG2000 and 3D-JPEG2000 in terms of compression ratio. The proposed compression scheme is designed for use with abdominal CT data sets. However, the segmentation model can be extended beyond the abdomen and it is expected that similar levels of compression can be achieved by applying the proposed technique to other parts of the human body and to medical images obtained by modalities other than CT.

In order to reduce the time for the transmission of CTC data sets, the ALMIC technique is integrated into a delivery scheme. This scheme transmits the precompressed data set and implements decompression in parallel. The proposed delivery solution can reduce the original download time by 65% at the typical connection speed available in Ireland. Further improvements can be achieved by optimising the template size based on connection speeds and removing the information associated with the scanning table and the patients' clothing. Integration of these improvements into the proposed scheme would result in the achievement of an even higher transmission speed for the delivery of CTC data sets.

Considering the large size of medical image data sets, there is a clear need for an efficient delivery scheme to provide fast access to image data. The proposed scheme meets this need and has the potential to bring about significant improvements in productivity in a teleradiology environment.

8.1.2 Minor Contributions

A number of minor contributions have resulted from the development of the CTC training framework documented in this thesis. They can be summarised as follows:

- **A new edge-based prediction method**: This method is designed for use with PVE regions and demonstrates a high level of prediction accuracy in the case of CTC data sets. This method is also applicable in the case of other body parts and other modalities.
- **A new trilinear interpolation operator**: This operator has a low computational cost and can be used in a range of potential application areas, including general volume rendering, surface reconstruction and 3D image registration. Integration of the new trilinear interpolation method has the potential to reduce the computational complexity significantly and improve the overall efficiency of these applications.
- **The incorporation of previously documented contributions into a comprehensive framework for remote access CTC training**: This framework has a short delivery time, a comprehensive set of visualisation tools and the ability to run on low-cost PC platforms with low-speed connections. It can be expected that the utilisation of such a CTC training system will improve the uptake of CTC in clinical settings. Increasing the availability of CTC has the potential to increase the number of patients benefitting from CTC and this in turn has the potential to reduce the mortality rates associated with CRC.

8.2 Future Work

There is a great deal of potential for future work in the area of remote access CTC frameworks. Some of the main areas that warrant further research are outlined below.

1. The proposed compression scheme only integrates two major stages: decorrelation and entropy coding. The compression result may potentially be improved further by introducing a context model for reducing the prediction error. Some studies (Ramabadran & Chen, 1992; Wu & Memon, 1997) have shown that the utilisation of a context model after the decorrelation stage in combination with an arithmetic entropy coder could significantly increase the compression ratio. However, current context models have a high computational cost that results in a long decompression time. Clearly, they are not applicable in the delivery scenario presented in this thesis. Future work could involve the development of a compression technique that combines a prediction model, an efficient context modelling method and an arithmetic encoder.

2. In this research, the edge-based predictor is designed for use in the PVE regions. It adaptively rotates the prediction template so that it is optimally aligned with the PVE boundary. This allows the predictor to make an accurate prediction. However, the PVE regions have a common density profile along the normal direction which can be utilised to improve prediction accuracy. Further research could involve investigation of the benefit associated with the inclusion of a profile-based prediction method to deal with PVE regions.

3. The validity of the ALMIC scheme is illustrated in the case of abdominal CT images. However, it is possible to apply ALMIC to images generated by

a range of modalities, e.g. MR and PET. In addition, it is also potentially useful in the compression of image data associated with other body parts. Further analysis of ALMIC when applied to these scenarios has the potential to generate a unified compression solution for the entire human body.

4. Considerable effort has been devoted to the development of acceleration techniques for software-based volume rendering. Hardware acceleration is another research direction that has led to volume rendering techniques that improve rendering performance. Kruger & Westermann (2003) have implemented a ray casting algorithm on the GPU which achieved a 50% improvement in efficiency over standard ray casting, thus demonstrating that there is great potential to further improve the performance of volume rendering using GPU-based acceleration methods. The current implementation of the proposed volume rendering technique, which is based on a non-GPU approach, is able to achieve real-time performance without any loss of image quality. Since more than 90% of machines currently in use are equipped with GPUs (Fresse *et al.*, 2010), further improvement of the proposed technique in terms of increasing the frame rate and enlarging the size of the rendering subvolume can be achieved by taking advantage of graphics hardware acceleration.

5. In the process of CTC interpretation, a range of tools can be used to improve the accuracy and efficiency of polyp detection. These tools include computer-aided detection (Yoshida & Nappi, 2001), fecal tagging (Thomeer *et al.*, 2003) and intra-patient supine-prone colon registration (Acar *et al.*, 2001). Therefore, these features could be integrated into the existing framework in order to assist trainees in making a timely and accurate interpretation, thereby enhancing their learning experience.

6. At the time of writing, there is still no consensus on a strategy for CTC training. Although some radiology organisations recommend that 50 to 100 cases should be used, a recent study by Liedenbaum *et al.* (2011) suggests that novice readers are only able to demonstrate the same sensitivity as experienced readers after studying an average of 164 CTC training cases. This significant discrepancy in the number of studies required for CTC necessitates further investigation. Utilisation of the proposed system can provide a straightforward and cost-effective way to identify an optimum number of cases required for CTC training.

Appendix A: Description of the Data Used for Development and Testing

This appendix provides a detailed description of the CTC data that was used for the development, training and evaluation of the compression and volume rendering techniques outlined in this thesis. The data was obtained from the Department of Radiology at the Mater Misericordiae University Hospital in Dublin. A complete description of these data sets is provided in Table 2 and an explanation of the abbreviations used in Table 2 is presented in Table 1 below.

Table 1: An explanation of the abbreviations used in Table 2.

Abbreviation	Meaning
VRTe	volume rendering testing
STr	segmentation training
STe	segmentation testing
TTr	template training
PTe	prediction testing
CTe	compression testing

Table 2: Details of the CTC data sets used in this thesis.

Data set	Patient position	3D dimension	Bit/pixel	Size	Used for
1	Supine	512 × 512 × 246	12	125,952 KB	CTe, STe
2	Supine	512 × 512 × 284	12	145,408 KB	CTe, STe, PTe
3	Supine	512 × 512 × 289	12	147,968 KB	CTe, PTe, VRTe
4	Supine	512 × 512 × 295	12	151,040 KB	CTe, VRTe
5	Supine	512 × 512 × 266	12	136,192 KB	CTe
6	Supine	512 × 512 × 267	12	136,704 KB	CTe
7	Supine	512 × 512 × 261	12	133,632 KB	CTe
8	Supine	512 × 512 × 303	12	146,944 KB	CTe
9	Supine	512 × 512 × 248	12	126,976 KB	CTe
10	Supine	512 × 512 × 259	12	132,608 KB	CTe, PTe
11	Prone	512 × 512 × 238	12	121,856 KB	CTe, STe
12	Prone	512 × 512 × 245	12	125,440 KB	CTe
13	Prone	512 × 512 × 303	12	155,136 KB	CTe
14	Prone	512 × 512 × 233	12	119,296 KB	CTe
15	Prone	512 × 512 × 282	12	144,384 KB	CTe
16	Prone	512 × 512 × 273	12	139,776 KB	CTe
17	Prone	512 × 512 × 303	12	155,136 KB	CTe
18	Prone	512 × 512 × 279	12	142,848 KB	CTe
19	Prone	512 × 512 × 266	12	136,192 KB	CTe
20	Prone	512 × 512 × 284	12	145,408 KB	CTe
21	Supine	512 × 512 × 249	12	127,488KB	STr, TTr, VRTe
22	Supine	512 × 512 × 281	12	143,872KB	STr, TTr, VRTe
23	Supine	512 × 512 × 251	12	128,512KB	STr, TTr
24	Supine	512 × 512 × 252	12	129,024KB	STr, TTr
25	Supine	512 × 512 × 248	12	126,976KB	STr, TTr
26	Supine	512 × 512 × 220	12	112,640KB	STr, TTr
27	Supine	512 × 512 × 220	12	112,640KB	STr, TTr
28	Supine	512 × 512 × 266	12	136,192KB	STr, TTr
29	Supine	512 × 512 × 245	12	125,440KB	STr, TTr
30	Supine	512 × 512 × 287	12	146,944KB	STr, TTr
31	Supine	512 × 512 × 240	12	122,880KB	STr, TTr
32	Supine	512 × 512 × 317	12	162,304KB	STr, TTr
33	Supine	512 × 512 × 239	12	122,368KB	STr, TTr
34	Supine	512 × 512 × 267	12	136,704KB	STr, TTr
35	Prone	512 × 512 × 267	12	136,704KB	STr, TTr
36	Prone	512 × 512 × 302	12	154,624KB	STr, TTr
37	Prone	512 × 512 × 273	12	139,776KB	STr, TTr
38	Prone	512 × 512 × 275	12	140,800KB	STr, TTr
39	Prone	512 × 512 × 282	12	144,385KB	STr, TTr
40	Prone	512 × 512 × 266	12	136,193KB	STr, TTr, VRTe

Appendix B: Overview of the Implemented System

Navigation

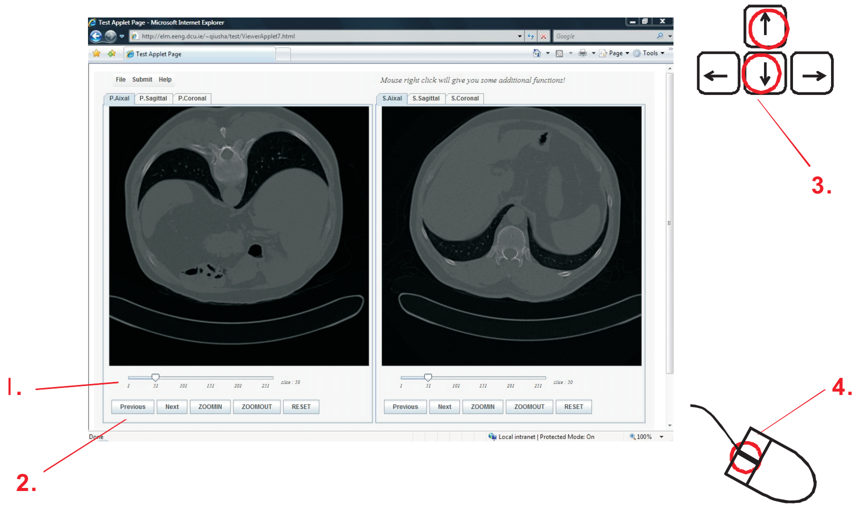
Mouse right click will give you some additional functions!

Figure 1: The four methods provided for navigating through the slices in a data set: slider-based navigation, previous and next buttons, arrow keys and scroll wheel.

Magnification

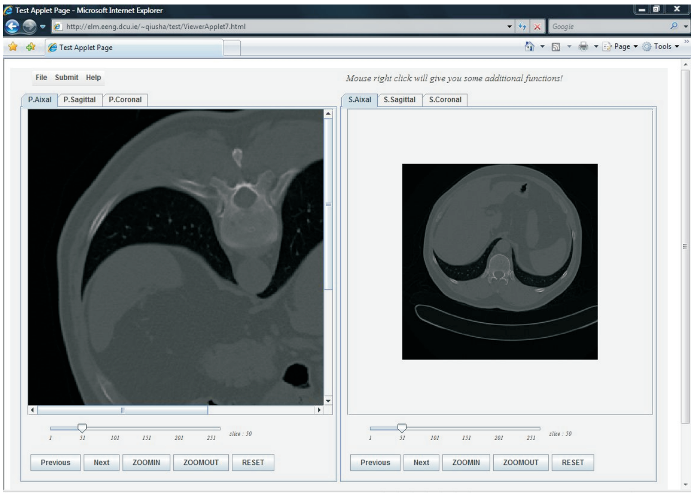

Mouse right click will give you some additional functions!

Figure 2: Control over the magnification of a slice using the zoom in, zoom out and reset buttons.

Reformatted Images (Axial, Sagittal and Coronal)

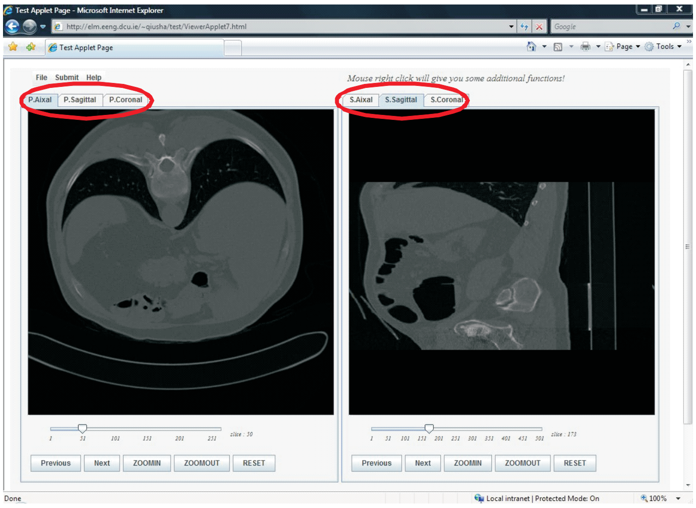

Mouse right click will give you some additional functions!

Figure 3: The three types of images provided by the system: axial, sagittal and coronal images. In this figure, an axial image is displayed on the left and a sagittal image is displayed on the right side.

Windowing

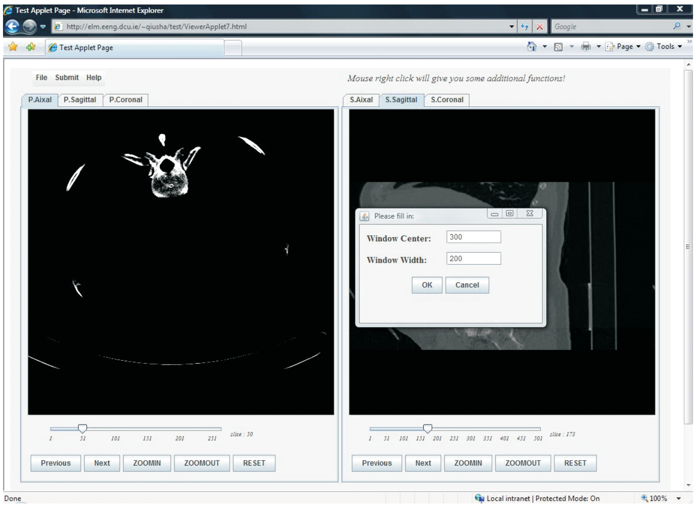

Mouse right click will give you some additional functions!

Please fill in:

Window Center: 300

Window Width: 200

Figure 4: A windowed image where the following settings have been used: window centre, 300 HU; window width, 200 HU.

Volume rendering

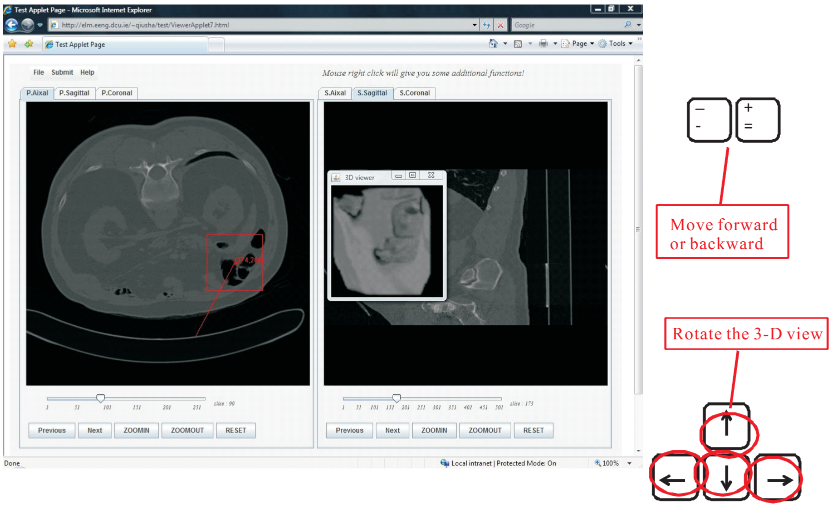

Mouse right click will give you some additional functions!

Figure 5: Perspective volume rendering of a region of interest. This 3D model can be rotated as follows: the plus key moves the viewpoint forward, the minus key moves the viewpoint backward and the arrow keys rotate the 3D model.

Surface rendering

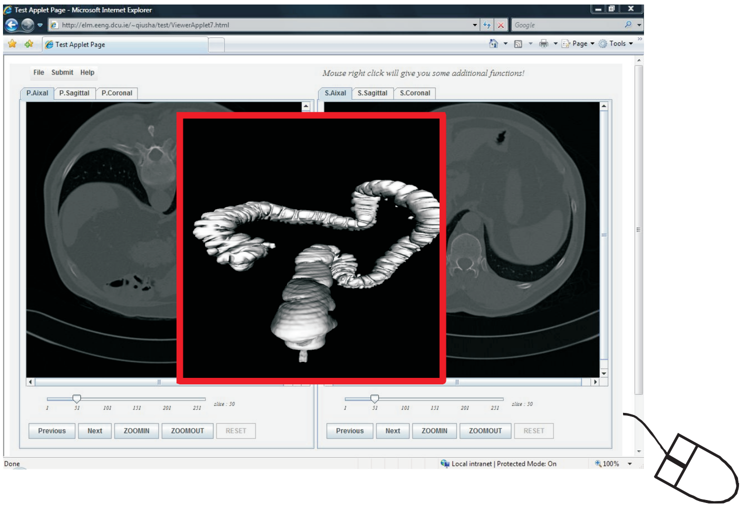

Mouse right click will give you some additional functions!

Figure 6: A surface rendering of the entire colon which can be controlled by the user via the mouse.

Fly-through

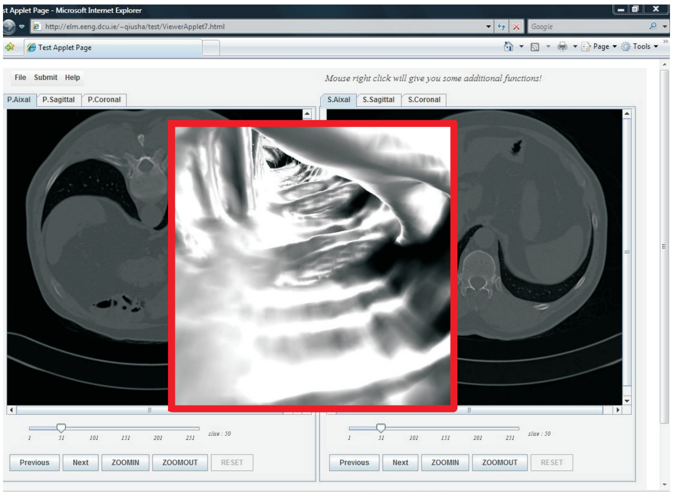

Mouse right click will give you some additional functions!

Figure 7: A single frame of fly-through within the surface rendered model of the colon.

Flagging a potential polyp

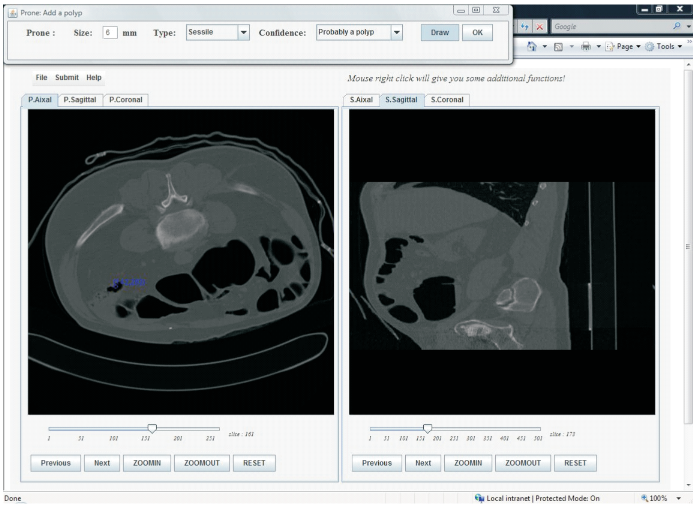

Prone : Size: 6 mm Type: Sessile Confidence: Probably a polyp

Mouse right click will give you some additional functions!

Figure 8: The tool for flagging a potential polyp. This tool allows a polyp size, a polyp type and a confidence value to be specified.

Evaluation panel

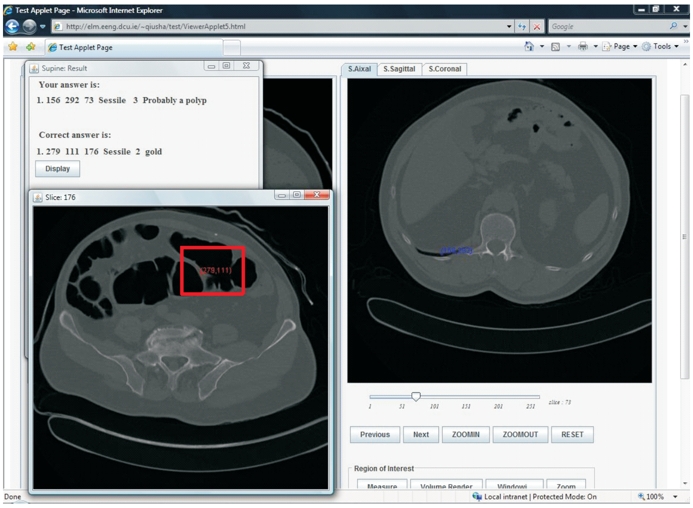

Your answer is:

1. 156 292 73 Sessile 3 Probably a polyp

Correct answer is:

1. 279 111 176 Sessile 2 gold

Figure 9: Automatic evaluation of the submitted findings based on the gold standard and presentation of the correct diagnosis.

References

ACAR, B., NAPEL, S., PAIK, D., LI, P., YEE, J., JEFFREY, R. & BEAULIEU, C. (2001). Medial axis registration of supine and prone CT colonography data. In *Proceedings of the 23rd Annual International Conference of the IEEE*, vol. 3, 2433 – 2436, Istanbul, Turkey, 25-28 October.

AIT-AOUDIA, S., BENHAMIDA, F.Z. & YOUSFI, M.A. (2006). Lossless compression of volumetric medical data. In *Computer and Information Sciences*, vol. 4263 of *Lecture Notes in Computer Science*, 563–571, Springer Berlin / Heidelberg.

ALAKUIJALA, J., JASKE, U., SALLINEN, S., HEHMINEN, H. & LAITINEN, J. (1996). Reconstruction of digital radiographs by texture mapping, ray casting and splatting. In *Proceedings of the 18th Annual International Conference of the IEEE*, vol. 2, 643 –645, Amsterdam, Netherlands, 31 October -3 November.

ALOMARI, R., KOMPALLI, S. & CHAUDHARY, V. (2008). Segmentation of the liver from abdominal CT using markov random field model and GVF snakes. In *Proceedings of the International Conference on Complex, Intelligent and Software Intensive Systems*, 293 –298, Barcelona, Spain, 4-7 March.

ANDERSON, M., PASHA, T. & LEIGHTON, J. (2000). Endoscopic perforation of the colon: lessons from a 10-year study. *The American Journal of Gastroenterology*, **12**, 3418–3422.

ARNESEN, R.B., VON BENZON, E., ADAMSEN, S., SVENDSEN, L.B., SVENDSEN, L.B., RAASCHOU, H.O. & HANSEN, O.H. (2007). Diagnostic performance of computed tomography colonography and colonoscopy: A prospective and validated analysis of 231 paired examinations. *Acta Radiologica*, **48**, 831 – 837.

AVRAMOVIĆ, A. (2011). Lossless compression of medical images based on gradient edge detection. In *Proceedings of the 19th Telecommunications Forum (TELFOR)*, 1199 –1202, Serbia, Belgrade, 22-24 November.

AVRAMOVIĆ, A. & RELJIN, B. (2010). Gradient edge detection predictor for image lossless compression. In *Proceedings of ELMAR*, 131 –134, Zadar, Croatia, 15-17 September.

AVRAMOVIĆ, A. & SAVIĆ, S. (2011). Lossless predictive compression of medical images. *Serbian journal of electrical engineering*, **8**, 27–36.

BHAVANI, S. & THANUSHKODI, K. (2010). A survey on coding algorithms in medical image compression. *International Journal on Computer Science and Engineering*, **2**, 1429–1434.

BILGIN, A., ZWEIG, G. & MARCELLIN, M.W. (1998). Efficient lossless coding of medical image volumes using reversible integer wavelet transforms. In *Proceedings of the Data Compression Conference*, 428 –437, Snowbird, UT, 30 March - 1 April.

BILGIN, A., ZWEIG, G. & MARCELLIN, M.W. (2000). Three-dimensional image compression with integer wavelet transforms. *Applied Optics*, **39**, 1799–1814.

BRADY, M., JUNG, K., NGUYEN, H. & NGUYEN, T. (1998). Interactive volume navigation. *IEEE Transactions on Visualization and Computer Graphics*, **4**, 243–256.

BRAMBLE, J.M. (1989). Comparison of information-preserving and information-losing data-compression algorithms for CT images. *Radiology*, **170**, 453–455.

BURGENER, F. & KORMANO, M. (1996). *Differential Diagnosis in Computed Tomography*. Georg Thieme Verlag.

CABAN, J.J., JOSHI, A. & NAGY, P. (2007). Rapid development of medical imaging tools with open-source libraries. *Journal of Digital Imaging*, **20**, 83 – 93.

CABRAL, B., CAM, N. & FORAN, J. (1994). Accelerated volume rendering and tomographic reconstruction using texture mapping hardware. In *Proceedings of the 1994 symposium on Volume visualization*, 91–98, New York, USA.

CALHOUN, P., KUSZYK, B., HEATH, D., CARLEY, J.C. & FISHMAN, E.K. (1999). Three-dimensional volume rendering of spiral CT data: theory and method. *Radiographics*, **19**, 745–764.

CAMPADELLI, P., CASIRAGHI, E., PRATISSOLI, S. & LOMBARDI, G. (2009). Automatic abdominal organ segmentation from CT images. *Electronic Letters on Computer Vision and Image Analysis*, **8**, 1 – 14.

ÇELEBI, O.C. & ÇEVIK, U. (2010). Accelerating volume rendering by ray leaping with back steps. *Computer Methods and Programs in Biomedicine*, **97**, 99–113.

CHEN, Y.T. & TSENG, D.C. (2007). Wavelet-based medical image compression with adaptive prediction. *Computerized Medical Imaging and Graphics*, **31**, 1 – 8.

CHEN, Z.D., CHANG, R.F. & KUO, W.J. (1999). Adaptive predictive multiplicative autoregressive model for medical image compression. *IEEE Transactions on Medical Imaging*, **18**, 181 –184.

CHO, S., KIM, D. & PEARLMAN, W. (2004). Lossless compression of volumetric medical images with improved three-dimensional SPIHT algorithm. *Journal of Digital Imaging*, **17**, 57–63.

CHOWDHURY, T., GHITA, O. & WHELAN, P. (2005). A statistical approach for robust polyp detection in CT colonography. In *Proceedings of the 27th Annual International Conference of the Engineering in Medicine and Biology Society*, 2523 –2526, Shanghai, China, 1-4 September.

CLEARY, J. & WITTEN, I. (1984). Data compression using adaptive coding and partial string matching. *IEEE Transactions on Communications*, **32**, 396 – 402.

CLUNIE, D.A. (2000). Lossless compression of grayscale medical images - effectiveness of traditional and state of the art approaches. In *Proceedings of the SPIE Medical Imaging*, 74–84.

COHEN, D. & SHEFFER, Z. (1994). Proximity clouds - an acceleration technique for 3D grid traversal. *The Visual Computer*, **11**, 27–38.

DACHILLE, F., KREEGER, K., WAX, M., KAUFMAN, A. & LIANG, Z. (2001). Interactive navigation for PC-based virtual colonoscopy. In *Proceedings of the Medical Imaging 2001: Physiology and Function from Multidimensional Images*, 500–504.

DACHMAN, A.H. (2008). Training for Interpretation of CT Colonography: Some Get It, But Some Don't. Available at: `http://www.gastro.org/wmspage.cfm?parm1=4693`.

Dachman, A.H., Kelly, K.B., Zintsmaster, M.P., Rana, R., Khankari, S., Novak, J.D., Ali, A.N., Qalbani, A. & Fletcher, J.G. (2008). Formative evaluation of standardized training for CT Colonographic image interpretation by novice readers. *Radiology*, **249**, 167–177.

Das, M. & Burgett, S. (1993). Lossless compression of medical images using two-dimensional multiplicative autoregressive models. *IEEE Transactions on Medical Imaging*, **12**, 721 –726.

Das, M. & Lin, C. (1996). Lossless compression of medical images using hierarchical autoregressive models. In *Proceedings of the Ninth IEEE Symposium on Computer-Based Medical Systems*, 6 –11, Ann Arbor, USA, 17-18 June.

Deglint, H., Rangayyan, R., Ayres, F., Boag, G. & Zuffo, M. (2007). Three-dimensional segmentation of the tumor in computed tomographic images of neuroblastoma. *Journal of Digital Imaging*, **20**, 72–87.

Denecker, K., van Overloop, J. & Lemahieu, I. (1997). An experimental comparison of several lossless image coders for medical images. In *Proceedings of the Data Compression Conference*, 435, Snowbird, UT, USA, 25-27 March.

Deserno, T.M. (2011). *Biomedical Image Processing*. Springer Berlin Heidelberg.

Emamian, S.A., Nielsen, M.B., Pedersen, J.F. & Ytte, L. (1993). Kidney dimensions at sonography: correlation with age, sex, and habitus in 665 adult volunteers. *American Journal of Roentgenology*, **160**, 83–6.

Ericsson, K.A. (2004). Deliberate practice and the acquisition and maintenance of expert performance in medicine and related domains. *Academic Medicine*, **79**, 70–81.

FENLON, H.M., NUNES, D.P., SCHROY, P.C., BARISH, M.A., CLARKE, P.D. & FERRUCCI, J.T. (1999). A comparison of virtual and conventional colonoscopy for the detection of colorectal polyps. *The New England Journal of Medicine*, **341**, 1496–1503.

FRESSE, V., HOUZET, D. & GRAVIER, C. (2010). GPU architecture evaluation for multispectral and hyperspectral image analysis. In *Conference on Design and Architectures for Signal and Image Processing (DASIP)*, 121–127, Edinburgh, UK, 26-28 October.

FUNG, P. & HENG, P. (1998). Efficient volume rendering by isoregion leaping acceleration. In *Proceedings of the Sixth International Conference in Central Europe on Computer Graphics and Visualization*, 495–501.

GIBNEY, M.A., ARCE, C.H., BYRON, K.J. & HIRSCH, L.J. (2010). Skin and subcutaneous adipose layer thickness in adults with diabetes at sites used for insulin injections: implications for needle length recommendations. *Current Medical Research and Opinion*, **26**, 1519–1530.

GRASER, A., STIEBER, P., NAGEL, D., SCHÄFER, C., HORST, D., BECKER, C.R., NIKOLAOU, K., LOTTES, A., GEISBÜSCH, S., KRAMER, H., WAGNER, A.C., DIEPOLDER, H., SCHIRRA, J., ROTH, H.J., SEIDEL, D., GÖKE, B., REISER, M.F. & KOLLIGS, F.T. (2009). Comparison of CT colonography, colonoscopy, sigmoidoscopy and faecal occult blood tests for the detection of advanced adenoma in an average risk population. *Gut*, **58**, 241–248.

GRAY, H. (1977). *Anatomy, descriptive and surgical*. New York.

GUNDERMAN, R.B. (2006). *Essential Radiology: Clinical Presentation Pathophysiology Imaging*. Thieme Medical Publishers.

HARA, A.K., BLEVINS, M., CHEN, M.H., DACHMAN, A.H., KUO, M.D., MENIAS, C.O., SIEWERT, B., CHEEMA, J.I., OBREGON, R.G., FIDLER, J.L., ZIMMERMAN, P., HORTON, K.M., COAKLEY, K.J., IYER, R.B., HALVORSEN, R.A., CASOLA, G., YEE, J., HERMAN, B.A. & JOHNSON, C.D. (2011). Acrin ct colonography trial: Does reader's preference for primary two-dimensional versus primary three-dimensional interpretation affect performance? *Radiology*, **259**, 435–441.

HODDER, R., RIVINGTON, R., CALCUTT, L. & I.R., H. (1989). The effectiveness of immediate feedback during the objective structured clinical examination. *Medical Education*, **23**, 184–188.

HONG, L., MURAKI, S., KAUFMAN, A., BARTZ, D. & HE, T. (1997). Virtual voyage: Interactive navigation in the human colon. In *Proceedings of SIGGRAPH*, Los Angeles, USA, 3-8 August.

HUANG, Q. & DOM, B. (1995). Quantitative methods of evaluating image segmentation. In *International Conference on Image Processing*, vol. 3, 53–56, Washington, DC, USA, 23-26 October.

HUFFMAN, D. (1952). A method for the construction of minimum-redundancy codes. In *Proceedings of the IRE*, vol. 40, 1098 –1101.

JEFFREYS, H. & JEFFREYS, B. (1988). *Methods of Mathematical Physics*. England: Cambridge University Press.

JIANG, X., MARTI, C., IRNIGER, C. & BUNKE, H. (2005). Image segmentation evaluation by techniques of comparing clusterings. In *Image Analysis and Processing - ICIAP 2005*, vol. 3617 of *Lecture Notes in Computer Science*, 344–351, Springer Berlin Heidelberg.

Kim, D.H., Pickhardt, P.J., Taylor, A.J., Leung, W.K., Winter, T.C., Hinshaw, J.L., Gopal, D.V., Reichelderfer, M., Hsu, R.H. & Pfau, P.R. (2007a). CT Colonography versus Colonoscopy for the detection of advanced neoplasia. *The New England Journal of Medicine*, **357**, 1403–1412.

Kim, K.J., Lee, K.H., Kim, B., Richter, T., Yun, I.D., Lee, S.U., Bae, K.T. & Shim, H. (2011). JPEG2000 2D and 3D reversible compressions of thin-section chest CT images: improving compressibility by increasing data redundancy outside the body region. *Radiology*, **259**, 271–277.

Kim, S.H., Lee, J.M., Eun, H.W., Lee, M.W., Han, J.K., Lee, J.Y. & Choi, B.I. (2007b). Two- versus three-dimensional colon evaluation with recently developed virtual dissection software for CT Colonography. *Radiology*, **244**, 852–864.

Kim, Y. & Pearlman, W.A. (1999). Lossless volumetric medical image compression. In *Proceedings of SPIE application of digital image processing*, 305–312.

Kivijärvi, J., Ojala, T., Kaukoranta, T., Kuba, A., Nyúl, L. & Nevalainen, O. (1998). A comparison of lossless compression methods for medical images. *Computerized Medical Imaging and Graphics*, **22**, 323 – 339.

Knezovic, J., Kovac, M. & Mlinaric, H. (2006). A new adaptive blending predictor for lossless image compression. In *Proceedings of the 4th International Conference on Information Communications Technology*, 1–12, Cairo, Egypt, 10-12 December.

Kofidis, E., Kolokotronis, N., Vassilarakou, A., Theodoridis, S. & Cavouras, D. (1999). Wavelet-based medical image compression. *Future Generation Computer Systems*, **15**, 223 – 243.

KOVALEV, V., KRUGGEL, F., GERTZ, H.J. & VON CRAMON, D. (2001). Three-dimensional texture analysis of MRI brain datasets. *IEEE Transactions on Medical Imaging*, **20**, 424 –433.

KRUGER, J. & WESTERMANN, R. (2003). Acceleration techniques for GPU-based volume rendering. In *Proceedings of the 14th IEEE Visualization*, Seattle, WA, USA, 24 October.

KUDUVALLI, G. & RANGAYYAN, R. (1992). Performance analysis of reversible image compression techniques for high-resolution digital teleradiology. *IEEE Transactions on Medical Imaging*, **11**, 430 –445.

KWON, M., KIM, H.J., LEE, C.W. & LEE, S.U. (1999). A lossless image coder with context-based minimizing MSE prediction and entropy coding. In *Proceedings of the IEEE International Symposium on Circuits and Systems*, vol. 4, 479 –482, Orlando, FL, USA.

LACROUTE, P. & LEVOY, M. (1994). Fast volume rendering using a shear-warp factorization of the viewing transformation. In *Proceedings of the 21st annual conference on Computer graphics and interactive techniques*, 451–458.

LAKARE, S. & KAUFMAN, A. (2004). Light weight space leaping using ray coherence. In *Proceedings of IEEE visualsitation*, 19–26, 10-15 October.

LEE, T.Y., LIN, P.H., LIN, C.H., SUN, Y.N. & LIN, X.Z. (1999). Interactive 3-D virtual colonoscopy system. *IEEE Transactions on Information Technology in Biomedicine*, **3**, 139 –150.

LEMPEL, A. & ZIV, J. (1977). A universal algorithm for data compression. *IEEE Transactions on Inform Theory*, 337–343.

LEVOY, M. (1988). Display of surfaces from volume data. *IEEE Computer Graphics and Applications*, **8**, 29–37.

LEVOY, M. (1990). Efficient ray tracing of volume data. *ACM Transactions on Graphics*, **9**, 245–261.

LI, W., KAUFMAN, A. & KREEGER, K. (2001). Real-time volume rendering for virtual colonoscopy. In *Proceedings of Volume Graphics*, 363–374.

LI, W., MUELLER, K. & KAUFMAN, A. (2003). Empty space skipping and occlusion clipping for texture-based volume rendering. In *Proceedings of the 14th IEEE Visualization*, 317–324, Seattle, WA, USA, 24 October.

LI, X. & ORCHARD, M. (2001). Edge-directed prediction for lossless compression of natural images. *IEEE Transactions on Image Processing*, **10**, 813 –817.

LIANG, J.Y., CHEN, C.S., HUANG, C.H. & LIU, L. (2008). Lossless compression of medical images using Hilbert space-filling curves. *Computerized Medical Imaging and Graphics*, **32**, 174 – 182.

LIEDENBAUM, M.H., BIPAT, S., BOSSUYT, P.M.M., DWARKASING, R.S., DE HAAN, M.C., JANSEN, R.J., KAUFFMAN, D., VAN DER LEIJ, C., DE LIJSTER, M.S., LUTE, C.C., VAN DER PAARDT, M.P., THOMEER, M.G., ZIJLSTRA, I.A. & STOKER, J. (2011). Evaluation of a standardized CT Colonography training program for novice readers. *Radiology*, **258**, 477–487.

LIM, S. & SHIN, B.S. (2008). A distance template for octree traversal in CPU-based volume ray casting. *The Visual Computer*, **24**, 229–237.

LIN, D.T., LEI, C.C. & HUNG, S.W. (2006). Computer-aided kidney segmentation on abdominal CT images. *IEEE Transactions on Information Technology in Biomedicine*, **10**, 59 –65.

LORENSEN, W.E. & CLINE, H.E. (1987). Marching cubes: A high resolution 3D surface construction algorithm. *SIGGRAPH Computer Graphics*, **21**, 163–169.

LUNDGREN, H. (2002). *Implementation and real-world evaluation of routing protocols for wireless ad hoc networks*. Licentiate thesis, Uppsala University.

MARTIN, D., FOWLKES, C., TAL, D. & MALIK, J. (2001). A database of human segmented natural images and its application to evaluating segmentation algorithms and measuring ecological statistics. In *8th International Conference on Computer Vision*, 416–423, Vancouver, BC, Canada, 7-14 July.

MARTINEZ, J.D. (2005). *Focus On Colorectal Cancer Research*. Nova Science Publishers.

MENEGAZ, G. (2006). Trends in medical image compression. *Current Medical Imaging Reviews*, **2**, 165šC185.

MIAOU, S.G., KE, F.S. & CHEN, S.C. (2009). A lossless compression method for medical image sequences using JPEG-LS and interframe coding. *IEEE Transactions on Information Technology in Biomedicine*, **13**, 818 –821.

MIN, Q. & SADLEIR, R.J. (2012). An edge-based prediction approach for medical image compression. In *Proceedings of the IEEE-EMBS Conference on Biomedical Engineering (IECBES 2012)*, Langkawi, Malaysia, 17-19 December.

MOTTA, G., STORER, J. & CARPENTIERI, B. (1999). Adaptive linear prediction lossless image coding. In *Proceedings of the Data Compression Conference*, 491 –500, Snowbird, UT, USA, 29-31 March.

MUNTEANU, A., CORNELIS, J., VAN DER AUWERA, G. & CRISTEA, P. (1999). Wavelet-based lossless compression scheme with progressive transmission capability. *International Journal of Imaging Systems and Technology*, **10**, 76–85.

Mykkäen, J., Tohka, J., Luoma, J. & Ruotsalainen, U. (2005). Automatic extraction of brain surface and mid-sagittal plane from PET images applying deformable models. *Computer Methods and Programs in Biomedicine*, **79**, 1 – 17.

Niemeyer, P. & Knudsen, J. (2005). *Learning Java*. O'Reilly Media.

Novins, K.L., Sillion, F.X. & Greenberg, D.P. (1990). An efficient method for volume rendering using perspective projection. *SIGGRAPH Comput. Graph.*, **24**, 95–102.

Pickhardt, P.J., Lee, A.D., Taylor, A.J., Michel, S.J., Winter, T.C., Shadid, A., Meiners, R.J., Chase, P.J., Hinshaw, J.L., Williams, J.G., Prout, T.M., Husain, S.H. & Kim, D.H. (2007). Primary 2D versus primary 3D polyp detection at screening CT Colonography. *American Journal of Roentgenology*, **189**, 1451–1456.

Qing, D., Chen, J. & Wang, Z. (2010). An improved ray-casting algorithm based on aabb. In *Proceedings of the International Conference on Audio Language and Image Processing (ICALIP)*, 582 –586, Shanghai, China, 23-25 November.

Rabbani, M. & Jones, P.W. (1991). Image compression techniques for medical diagnostic imaging systems. *Journal of Digital Imaging*, **4**, 65–78.

Rabushka, L.S., Kawashima, A. & Fishman, E.K. (1994). Imaging of the spleen: CT with supplemental MR examination. *Radiographics*, **14**, 307–332.

Ramabadran, T. & Chen, K. (1992). The use of contextual information in the reversible compression of medical images. *IEEE Transactions on Medical Imaging*, **11**, 185 –195.

Ramesh, S. & Shanmugam, A. (2010). Medical Image Compression using Wavelet Decomposition for Prediction Method. *International Journal of Computer Science and Information Security*, **7**, 262 – 265.

Ramkumar, D. & Raglend, I.J. (2012). Performance analysis of low complexity lossless compression scheme for medical image sequences. *European Journal of Scientific Research*, **89**, 562–567.

RANZCR (2012). Ranzcr requirements for the practice of computed tomography colonography. Available at: `http://www.ranzcr.edu.au/component/docman/doc_down`.

Rao, C. & Toutenburg, H. (1999). *Linear Models: Least Squares and Alternatives*. Springer.

Roberts, L.G. (1965). Machine perception of three dimensional solids. In *Optical and Electro-optical Information Processing*, 159–197.

Rolfe, I.E. & Sanson-Fisher, R.W. (2002). Translating learning principles into practice: a new strategy for learning clinical skills. *Medical Education*, **36**.

Roos, P. & Viergever, M. (1993). Reversible 3-D decorrelation of medical images. *IEEE Transactions on Medical Imaging*, **12**, 413 –420.

Roos, P., Viergever, M., van Dijke, M. & Peters, J. (1988). Reversible intraframe compression of medical images. *IEEE Transactions on Medical Imaging*, **7**, 328 –336.

Rubin, G.D., Beaulieu, C.F., Argiro, V., Ringl, H., Norbash, A.M., Feller, J.F., Dake, M.D., Jeffrey, R.B. & Napel, S. (1996). Perspective volume rendering of CT and MR images: applications for endoscopic imaging. *Radiology*, **199**, 321–330.

SAID, A. & PEARLMAN, W. (1996). A new, fast, and efficient image codec based on set partitioning in hierarchical trees. *IEEE Transactions on Circuits and Systems for Video Technology*, **6**, 243 –250.

SANCHEZ, V., ABUGHARBIEH, R. & NASIOPOULOS, P. (2009). Symmetry-based scalable lossless compression of 3D medical image data. *IEEE Transactions on Medical Imaging*, **28**, 1062 –1072.

SCHELKENS, P., BARBARIEN, J. & CORNELIS, J.P. (2000). Compression of volumetric medical data based on cube splitting. In *Proceedings of the Applications of Digital Image*.

SEEMANN, T., TISCHER, P. & MEYER, B. (1997). History-based blending of image sub-predictors. In *Proceedings of the 1997 International Picture Coding Symposium*, 147–151.

SHANNON, C.E. (1948). A mathematical theory of communication. *The Bell System Technical Journal*, **27**, 379–423,623–656.

SHAPIRO, J. (1993). Embedded image coding using zerotrees of wavelet coefficients. *IEEE Transactions on Signal Processing*, **41**, 3445 –3462.

SHEN, L. & RANGAYYAN, R.M. (1997). A segmentation-based lossless image coding method for high-resolution medical image compression. *IEEE Transactions on Medical Imaging*, **16**, 301– 307.

SLATER, A., TAYLOR, S.A., TAM, E., GARTNER, L., SCARTH, J., PEIRIS, C., GUPTA, A., MARSHALL, M., BURLING, D. & HALLIGAN, S. (2006). Reader error during CT colonography: causes and implications for training. *European Radiology*, **16**, 2275–2283.

Slomka, P.J., Elliott, E. & Driedger, A.A. (2000). Java-based remote viewing and processing of nuclear medicine images: Toward “the imaging department without walls”. *Journal of Nuclear Medicine*, **41**, 111–118.

Soto, J.A., Barish, M.A. & Yee, J. (2005). Reader training in CT Colonography: how much is enough? *Radiology*, **237**, 26–27.

Strintzis, M.G. (1998). A review of compression methods for medical images in pacs. *International Journal of Medical Informatics*, **52**, 159 – 165.

Summers, R.M. (2010). Polyp size measurement at CT Colonography: What do we know and what do we need to know? *Radiology*, **255**, 707–720.

Svensson, M.H., Svensson, E., Lasson, A. & Hellström, M. (2002). Patient acceptance of CT Colonography and conventional colonoscopy: Prospective comparative study in patients with or suspected of having colorectal disease. *Radiology*, **222**, 337–345.

Taubman, D. (2000). High performance scalable image compression with EBCOT. *IEEE Transactions on Image Processing,*, **9**, 1158 –1170.

Taylor, P.M. (2007). A review of research into the development of radiologic expertise: Implications for computer-based training. *Academic Radiology*, **14**, 1252 – 1263.

Thomeer, M., Carbone, I., Bosmans, H., Kiss, G., Bielen, D., Vanbeckevoort, D., Van Cutsem, E., Rutgeerts, P. & Marchal, G. (2003). Stool tagging applied in thin-slice multidetector computed tomography colonography. *Journal of Computer Assisted Tomography*, **27**, 132–139.

Tiwari, A. & Kumar, R. (2008). Least squares based optimal switched predictors for lossless compression of images. In *Proceedings of the IEEE Interna-*

tional Conference on Multimedia and Expo, 1129 –1132, Hannover, German, 23-26 April.

Twining, P., McHugo, J. & Pilling, D. (2007). *Textbook of fetal abnormalities*. Churchill Livingstone Elsevier.

Ukrit, M., A.Umamageswari & G.R.Suresh (2011). A survey on lossless compression for medical images. *International Journal of Computer Applications*, **31**, 47–50.

Vidal, V., Mei, X. & Decaudin, P. (2008). Simple empty-space removal for interactive volume rendering. *Journal of Graphics, GPU, and Game Tools*, **13**, 21–36.

Vining, D., Gelfand, D., Bechtold, R., Scharling, E., Grishaw, E. & Shifrin, R. (1994). Technical feasibility of colon imaging with helical CT and virtual reality. *American Journal of Roentgenology*, **162**, 104.

Wallace, G. (1991). The JPEG sill picture compression standard. *Communications of the ACM*, **34**, 30–44.

Wan, M., Bryson, S. & Kaufman, A. (1998). Boundary cell-based acceleration for volume ray casting. *Computers & Graphics*, **22**, 715 – 722.

Wan, M., Tang, Q., Kaufman, A., Liang, Z. & Wax, M. (1999). Volume rendering based interactive navigation within the human colon. In *Proceedings of Visualization*, 397 –549, San Francisco, CA, USA, 29 October.

Wan, M., Li, W., Kreeger, K., Bitter, I., Kaufman, A., Liang, Z., Chen, D. & Wax, M. (2000). 3D virtual colonoscopy with real-time volume rendering. In *Proceedings of SPIE in Physiology and Function from Multidimensional Images*, 165–171.

Wan, M., Sadiq, A. & Kaufman, A. (2002). Fast and reliable space leaping for interactive volume rendering. In *Proceedings of IEEE Visualization*, 195 –202, Boston, MA, USA, 1 November.

Wang, H. & Pu, X. (2009). 3D medical CT images reconstruction based on VTK and visual C++. In *Proceedings of the 3rd International Conference on Bioinformatics and Biomedical Engineering*, 1 –4, Beijing, China, 11-13 June.

Wang, S., Zhu, H., Lu, H. & Liang, Z. (2008). Volume-based feature analysis of mucosa for automatic initial polyp detection in virtual colonoscopy. *International Journal of Computer Assisted Radiology and Surgery*, 131–142.

Wang, X., Li, C., Eberl, S., Fulham, M. & Feng, D. (2009). Automated liver segmentation for whole-body low-contrast CT images from PET-CT scanners. In *Proceedings of the Annual nternational Conference of the IEEE*, 3565 –3568, Minneapolis, MN, USA, 3-6 September.

Weinberger, M., Seroussi, G. & Sapiro, G. (1996). Loco-i: a low complexity, context-based, lossless image compression algorithm. In *Proceedings of the Data Compression Conference*, 140 –149, Snowbird, UT, USA.

Westover, L. (1989). Interactive volume rendering. In *Proceedings of the 1989 Chapel Hill workshop on Volume visualization*, 9–16.

WHO (2003). Global cancer rates could increase by 50 percent to 15 million by 2020 [online]. Available at: `http://www.who.int/mediacentre/news/releases/2003/pr27/en/`.

WHO (2012). Cancer [online]. Available at: `http://www.who.int/mediacentre/factsheets/fs297/en/`.

WITTEN, I.H., NEAL, R.M. & CLEARY, J.G. (1987). Arithmetic coding for data compression. *Communications of the ACM*, **30**, 520–540.

WOLF, I., VETTER, M., WEGNER, I., BÖTTGER, T., NOLDEN, M., SCHÖBINGER, M., HASTENTEUFEL, M., KUNERT, T. & MEINZER, H.P. (2005). The medical imaging interaction toolkit. *Medical Image Analysis*, **9**, 594 – 604.

WONG, S., ZAREMBA, L., GOODEN, D. & HUANG, H. (1995). Radiologic image compression-a review. In *Proceedings of the IEEE*, vol. 83, 194–219.

WU, X. & MEMON, N. (1997). Context-based, adaptive, lossless image coding. *IEEE Transactions on Communications*, **45**, 437 –444.

WU, X. & MEMON, N. (2000). Context-based lossless interband compression-extending CALIC. *IEEE Transactions on Image Processing*, **9**, 994 –1001.

XIONG, Z., WU, X., YUN, D. & PEARLMAN, W. (1998). Progressive coding of medical volumetric data using three-dimensional integer wavelet packet transform. In *Proceedings of the IEEE Second Workshop on Multimedia Signal Processing*, 553 –558, Redondo Beach, CA, USA, 7-9 December.

XIONG, Z., WU, X., CHENG, S. & HUA, J. (2003). Lossy-to-lossless compression of medical volumetric data using three-dimensional integer wavelet transforms. *IEEE Transactions on Medical Imaging*, **22**, 459 –470.

YAGEL, R. & SHI, Z. (1993). Accelerating volume animation by space-leaping. In *Proceedings of the IEEE Conference on Visualization*, 62 –69, San Jose, CA, USA, 25-29 October.

YE, H., DENG, G. & DEVLIN, J. (1999). Least squares approach for lossless image coding. In *Proceedings of the Fifth International Symposium on Signal*

Processing and Its Applications, vol. 1, 63–66, Brisbane, Qld, Australia, 22-25 August.

Yoshida, H. & Nappi, J. (2001). Three-dimensional computer-aided diagnosis scheme for detection of colonic polyps. *IEEE Transactions on Medical Imaging*, **20**, 1261 –1274.

You, S., Hong, L., Wan, M., Junyaprasert, K., Kaufman, A., Muraki, S., Zhou, Y., Wax, M. & Liang, Z. (1997). Interactive volume rendering for virtual colonoscopy. In *Proceedings of the 8th conference on Visualization '97*, 433–436, Phoenix, AZ, USA, 24-24 October.

Zagoria, R.J. (2004). *Genitourinary Radiology: The Requisites*. Mosby.

Zhao, L., Tian, Y., Sha, Y. & Li, J. (2009). Medical image lossless compression based on combining an integer wavelet transform with DPCM. *Frontiers of Electrical and Electronic Engineering in China*, **4**, 1–4.

Zhuge, B., Feng, H.Q. & Zhou, H.Q. (2003). A fast tri-linear interpolation algorithm for volume rendering of medical images. *Space Medicine & Medical Engineering*, **16**, 206–209.

Ziv, J. & Lempel, A. (1978). Compression of individual sequences via variable-rate coding. *IEEE Transactions on Information Theory*, **IT-24**, 530–535.

Zucker, S.W. & Hummel, R.A. (1981). A three-dimensional edge operator. *IEEE Transactions on Pattern Analysis and Machine Intelligence*, **3**, 324–331.